SPIRE-AST-DOC-001433

Title: **HERSCHEL Straylight Calculation Results**

CI-No: 120000

Prepared by:	A. Frey / H. Hartmann	Date:	02.04.2004
Checked by:	J. Kroeker		6.4.2004
Product Assurance:	R. Stritter		06.04.04
Configuration Control:	W. Wietbrock		07.04.04
Project Management:	W. Rühe		7.4.04

Issue	Date	Sheet	Description of Change	Release
1	10.06.02	1-37	First issue	
2	18.10.02	1-74	Completely revised issue	
3	02.04.04	1-85	Completely revised issue	

Table of contents

1 Introduction

This TN presents the results of the Straylight Analysis for the orbit configuration of HERSCHEL.

2 Reference Documents

RD1	Herschel Telescope Straylight Analysis	HER.NT.017.T.ASTR, issue 3, 01 Okt. 02
RD2	Radiometric Environment Hypotheses for Straylight Assessments	H-P-1-ASPI-TN-0216, issue 2, Rev 01, 19/06/2002
RD3	Herschel Straylight Expertise	H-P-2-ASPI-TN-0379, issue 1, 27 Sep 02
RD4	Optical Configuration and Straylight during Ground Testing	HP-2-ASED-TN-0076, issue 2, 30.03.04

Applicable Document

AD1	H-EPLM Requirements Specification (HERS)	H-P-2-ASPI-SP-0250, issue 3/1

3 Straylight Requirements

The requirements in the AD1 are listed below:

For the spacecraft design w.r.t. straylight for the Herschel instruments an integrated approach has been selected. This means that the instrument optical layout is included in the system straylight analysis. This approach allows to directly provide the straylight level originated from the various sources at the detector level.

The system straylight requirements are given therefore directly as the straylight reaching the detector level. The system will provide the following maximum straylight over the full operational wavelength:

Scattered light (source outside the telescope FoV)
Taking into account the worst combination of the Moon and the Earth positions w.r.t. LOS of the telescope
with maximal:
− Sun - S/C - Earth angle of 37º
− Sun - S/C - Moon angle of 47º
− Sun - S/C - LOS angle of 60º to 120º (in x-z plane),
− Sun-S/C – LOS angle of ± 1° (about x = roll)
the straylight shall be: < 1.0% of background radiation induced by self-emission of the telescope.

Sources inside FOV:
Over the entire FOV at angular distances 3' from the peak of the point-spread-function (PSF), the straylight will be: < 1.10-4 of PSF peak irradiance (in addition to level given by diffraction).

Self-emission
The straylight level, received at the defined detector element location of the PLM/Focal Plane Unit Straylight model by self emission (with «cold» stops in front of PACS and SPIRE instrument detectors), not including the self emission of the telescope reflectors alone, should be < 10 % of the background induced by selfemission of the telescope reflectors.

4 Model Description

4.1 General Overview

The present status of the overall ASAP model is displayed in figure 4.1-1. A detailed plot of the design from the M1-baffle down to the instrument shield is shown in figure 4.1-2.

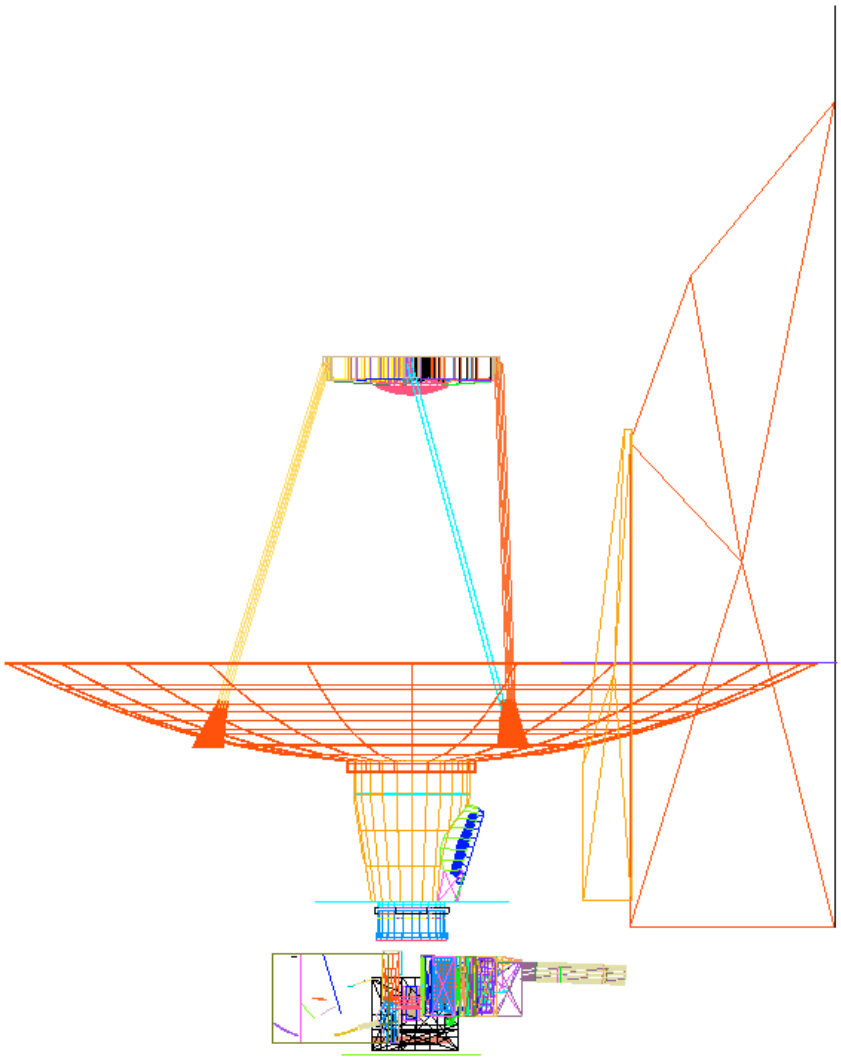

Figure 4.1-1: Overall configuration plotted with the ASAP model

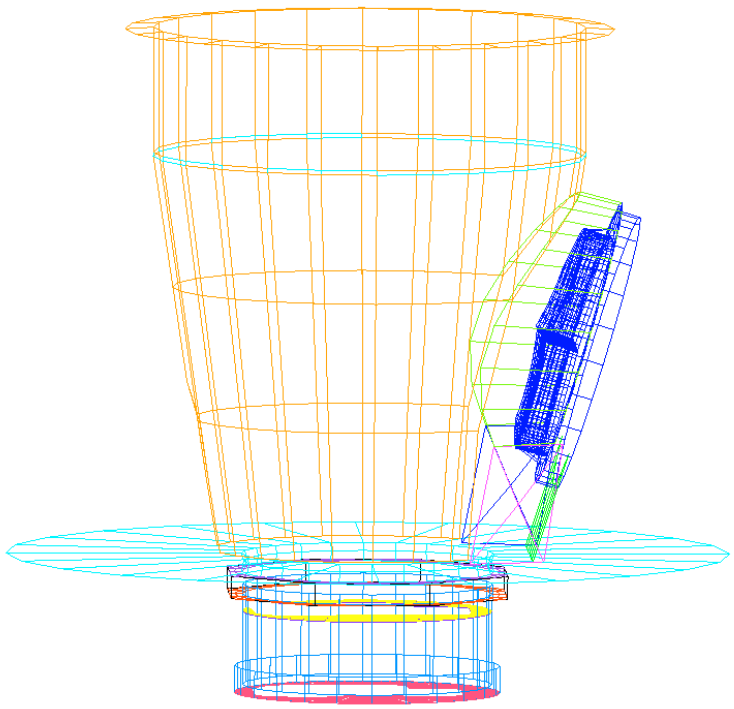

ring of M1-baffle (slightly inclined)

cylindrical part of M1-baffle

conical part of M1-baffle with cutouts (left and right) for the cryocover mechanisms

concave mirrors on cryocover

CVV

thermal shield 2 baffle and aperture

instrument shield baffle and aperture

Figure 4.1-2: Detail of design from M1-baffle down to the instrument shield

Four ASAP models have been received, all of them were integrated into the total optical ASAP model of Herschel

- the telescope model
- the SPIRE model
- the PACS model
- the HIFI-model

The rest of Herschel to be modeled for the straylight analysis comprises

- the sunshade
- the cryostat part near the cyrocover
- the baffles between CVV and telescope (M1-baffle), including the cryocover and cryocover mirrors
- the thermal shield and instrument shield baffles and apertures above the instruments.

Overview on the basis for the total model:

object	basis for modelling
OBA including instrument shield	drawing ref. no. HP-2-ASED-ID-0095-02-0A dated 15.10.03 drawing ref. no. HP-2-ASED-ID-0042-08-0A dated 31.03.03 drawing ref. no. HP-2-ASED-ID-0063-02-0B dated 15.10.03 drawing ref. no. HP-2-ASED-ID-0009-01-0B dated 11.07.03
PACS	ASAP Model from Kayser-Threde: file PACS-Top_Optics_Inside_11.inr (e-mail dated 27.03.02). model corrected and used by ASED: file PACS-Top_Opt_Ins_11korr.inr dated 26.06.02 contained in e-mail (dated 26.06.02) resent to Kayser-Threde new data for all mirrors received from MPE (excel file in e-mail dated 09.05.2003) some corrections made in order to reach the final file 'PACS_TopOptic_Coord_F.xls' as basis for the new ASAP command lines for all mirrors confirmation received from PACS (e-mail dated 28.11.03)
SPIRE	ASAP model from ESTEC/RAL files spire.inr, spire_macros.inr, spire_prop.inr, spire_scatter.inr, replacement_fp_unit.inr (e-mail dated 06.03.02) model corrected and used by ASED: file spire_tel2.inr dated 17.05.02 contained in e-mail (dated 17.05.02) resent to RAL/ESTEC new scattering functions for FP_UNIT (e-mail dated 09.01.03) new scattering function for thermal filter 1 (e-mail dated 06.06.03) confirmation received from SPIRE (e-mail dated 28.11.03)
HIFI	ASAP model from ESTEC files HiFi.inr, hifi_ch1.inr, hifi_ch2.inr, hifi_ch3.inr, hifi_ch4.inr, hifi_ch5.inr, hifi_ch6.inr, hifi_ch7.inr, hifi_prop.inr, hifi_macros.inr, hifi_struct.inr (e-mail dated 27.11.01)
thermal shield 2 baffle and aperture	drawing ref. no. HP-2-ASED-ID-0095-02-0A dated 15.10.03 drawing ref. no. HP-2-ASED-ID-0065-01-0B, not yet released.
CVV	drawing ref. no. HP-2-ASED-ID-0004-01-0E dated 06.08.03
cryostat baffle (M1-baffle)	drawing ref. no. HP-2-ASED-ID-0063-01-0B dated 15.10.03
cryocover	drawing ref. no. HP-2-ASED-ID-0095-01-0A dated 15.10.03 drawing ref. no. HP-2-ASED-ID-0095-02-0A dated 15.10.03
cryocover mirrors	specification HP-2-ASED-PS-0018, issue 3
telescope	ASAP model from ASEF (dated 26.05.02 by ASEF) new mirror scattering function in report 01-Her.NT.0017.T.ASTR-03 file HEXAPOD_NEW2.INR (dated 16.05.03) received from ESTEC
sunshade	drawing ref. no. HP-2-ASED-ID-0051-01-0B dated 17.07.03 drawing ref. no. HP-2-ASED-ID-0051-02-0B dated 17.07.03

4.2 ASAP instrument models

The instrument ASAP models are displayed in the next figures:

- the SPIRE model in figure 4.2-1
- the PACS model in figure 4.2-2
- the HIFI-model in figure 4.2-3.

Several iterations have been performed for SPIRE and PACS in order to have sufficient model fidelity.

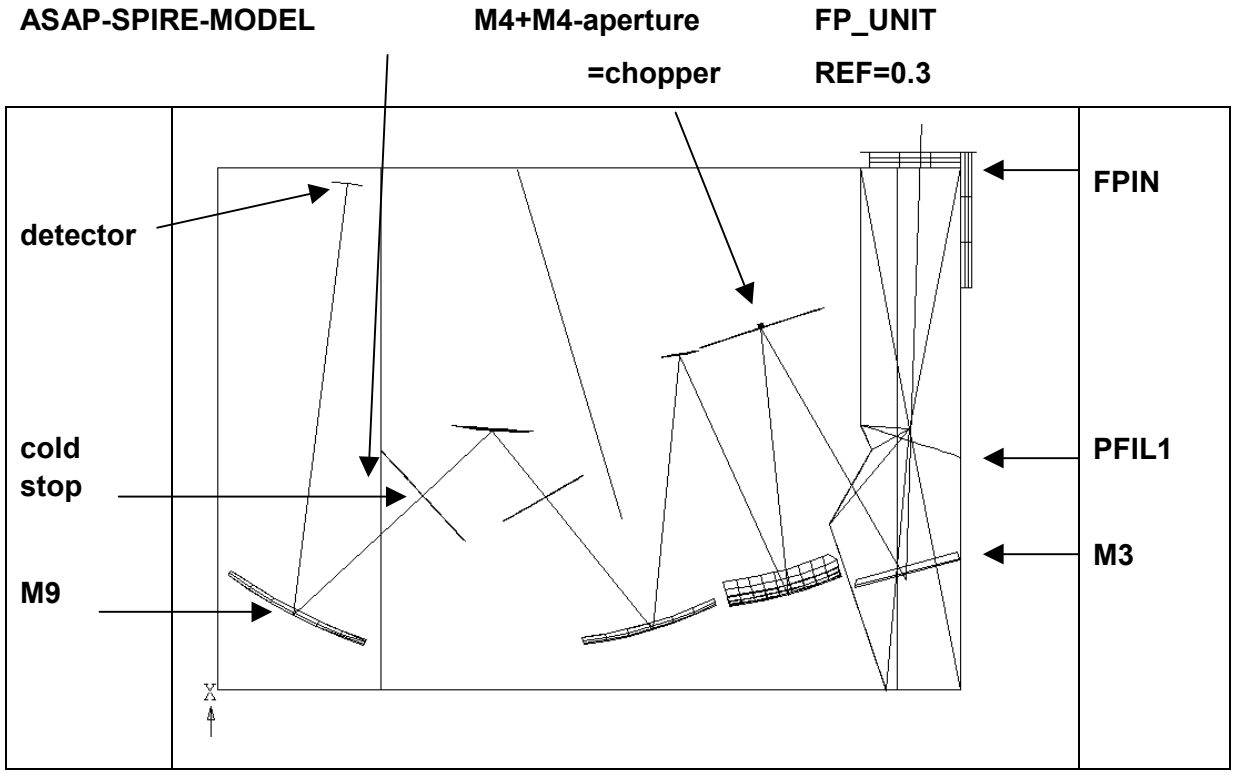

Figure 4.2-1: ASAP SPIRE model. It represents a singular path towards one of the detectors of the photometer. This photometer path is representative for the straylight sensitive paths within SPIRE.

ASAP PACS-MODEL→cold stop chopper

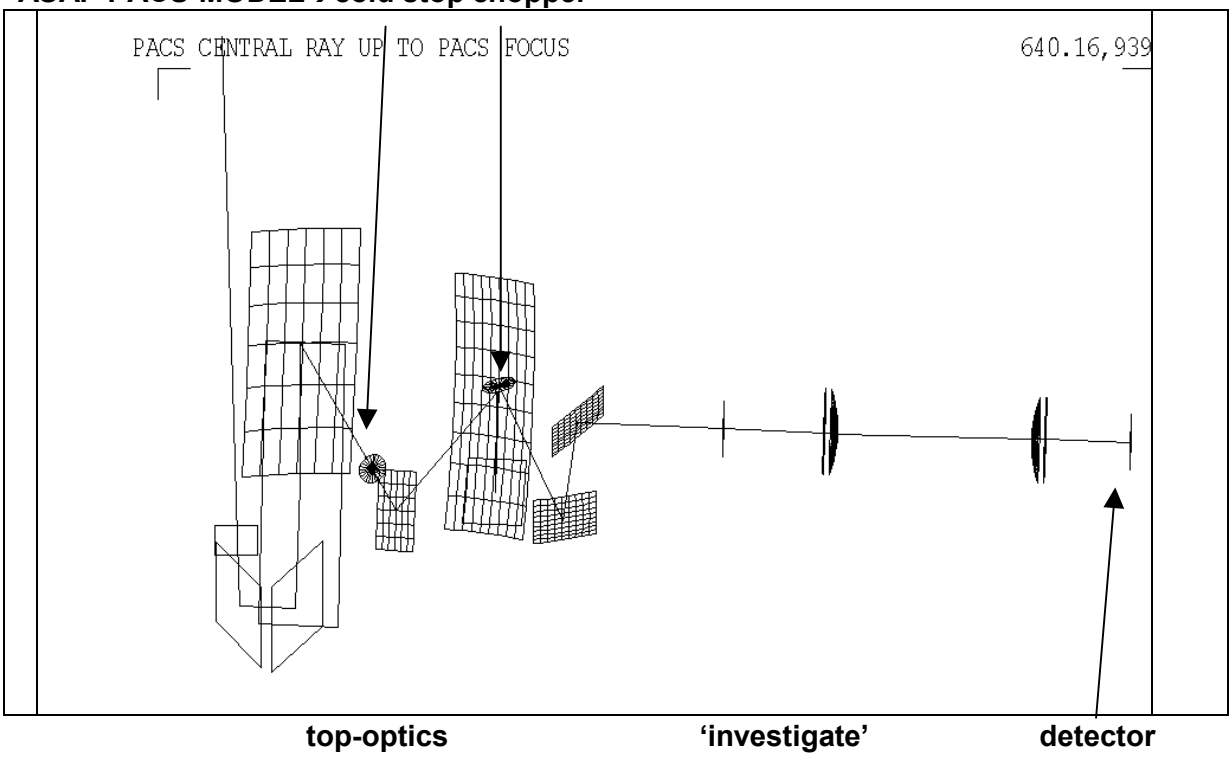

Figure 4.2-2: ASAP PACS model. Only the optics is shown, without structural elements. A specific detector path has been selected as representative for straylight.

Compared to issue 2 of this technical note, there was a considerable change in the ASAP model for PACS

- there is a new data basis for the modeling of all mirrors, i.e. an Excel sheet with mirror data. The ASAP commands for the mirrors have been set up by Astrium. The difference to the earlier mirror geometry mainly affects the mirror limitations (not the curvatures and distances)
- all calibration mirrors are modeled now
- the entrance opening is modeled now.

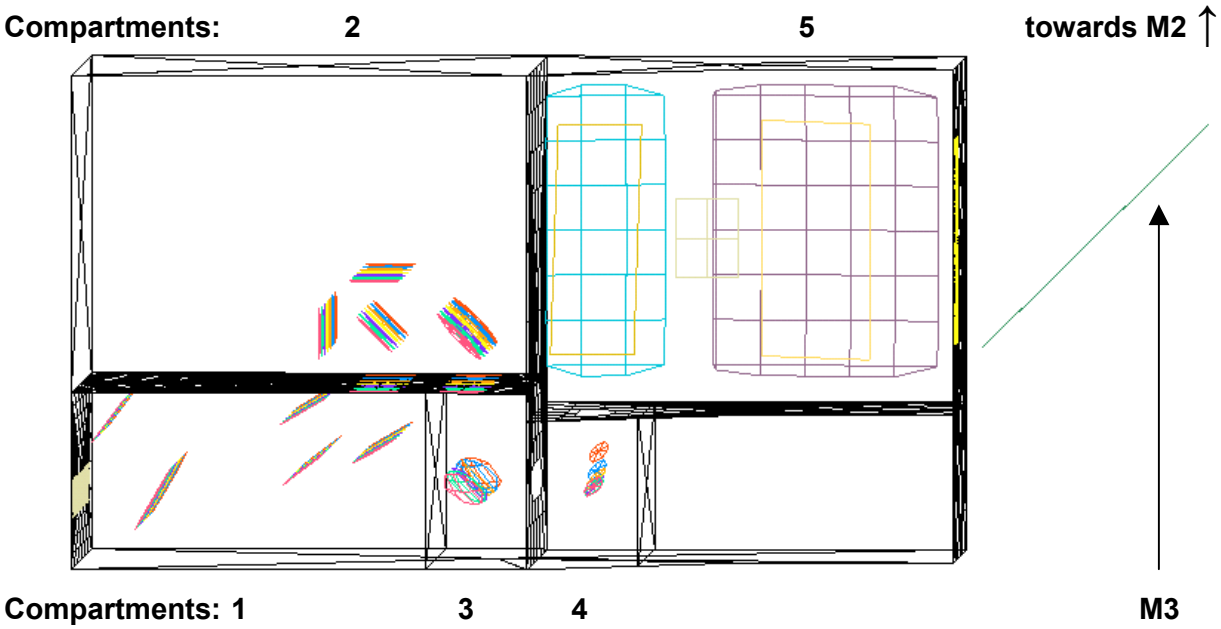

Figure 4.2-3 ASAP-HIFI model. HIFI is not straylight sensitive; it is included because it may influence straylight towards PACS and SPIRE. The compartment numbering is introduced in order to enable easier description of the straylight calculations. The compartment numbers increase from the local oscillator windows to the inner opening towards M3 and M2 (telescope secondary mirror).

There is an object-image relation between the hole within SPIRE M4 and the center of M2. This leads to a partial obscuration of some straylight contributions, as the calculations will show.

The optics design of SPIRE confines the acceptance cone for purely specular radiation very closely to the secondary mirror, as a backward raytrace shows. Only a very small fraction of the hexapod can be seen by the SPIRE detector (see figure 4.2-4).

The confinement of the acceptance cone for purely specular radiation is similar for PACS (not as close as for SPIRE). A backward trace from the PACS detector is shown in figure 4.2-5.

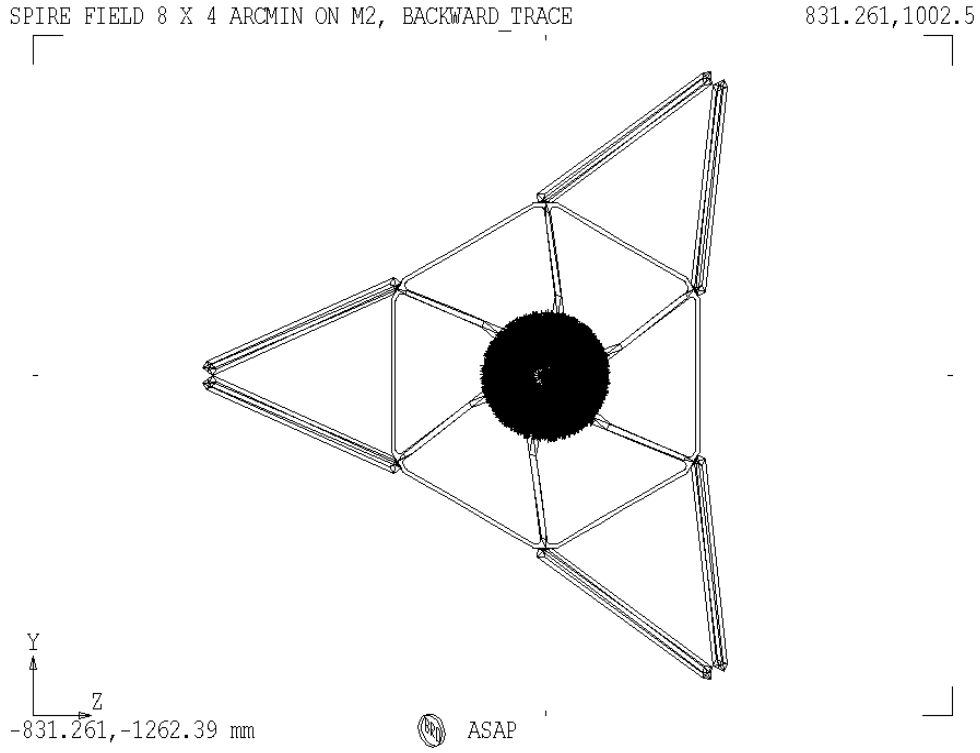

Figure 4.2-4: Backward trace onto M2 starting from the SPIRE detector

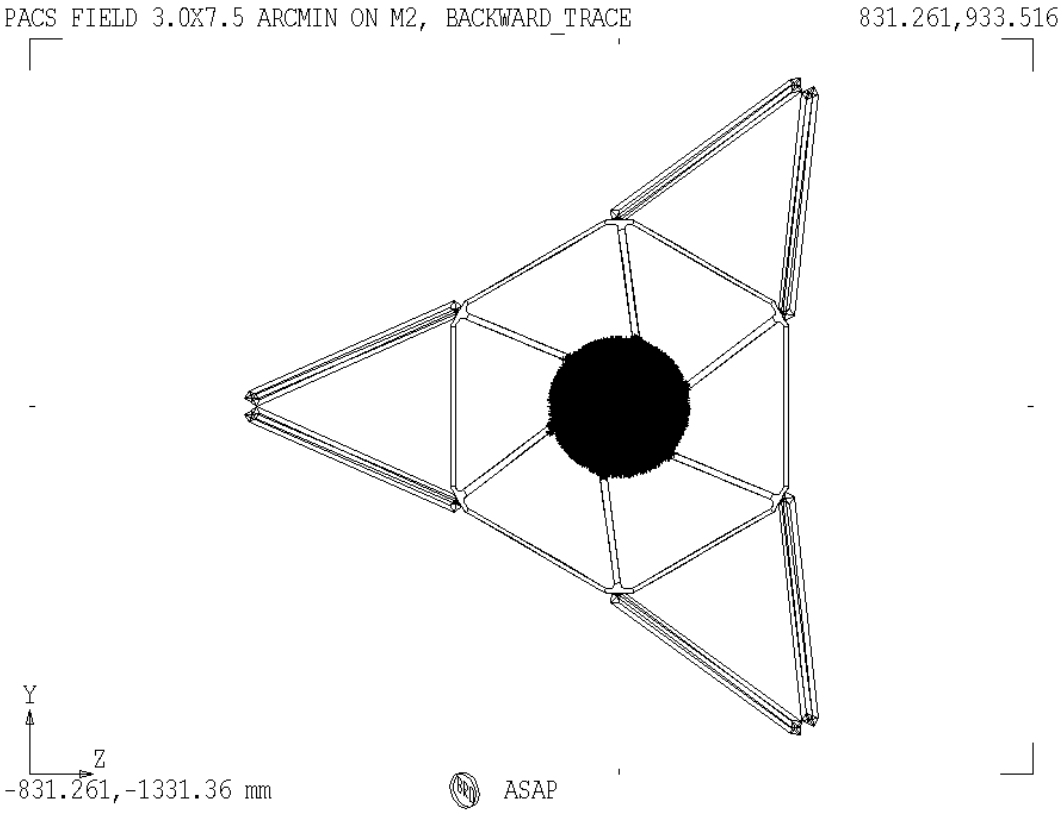

Figure 4.2-5: Backward trace onto M2 starting from the PACS detector

For the straylight calculations the instrument detectors labelled in figures 4.2-1 and 4.2-2 have been considered as representative for all detectors of the respective instrument.

The apodization effect (or edge taper) of the horns in front of the SPIRE detectors is included. For radiation impinging on the horns, this effect produces a change in sensitivity depending on the angle w.r.t. the horn axis such that the sensitivity decreases for increasing angles. Projected onto the pupils of SPIRE (cold stop, telescope secondary) there is a decrease of 8 dB, i.e. an edge taper of 8 dB. This edge taper is realized for the calculations with the apodization function of ASAP, this is a ray change in ASAP. Thus there is no change of objects in the ASAP SPIRE model. The effect of the ASAP apodization is displayed in figure 4.2-6. This is not just a graphical representation of a gaussian function, but the result of a raytrace with a beam starting at the telescope secondary and ending at the SPIRE detector. There the resulting radiant intensity (in direction cosine space) is displayed without and with apodization.

All the calculations in issue 2 and issue 3 (i.e. those on thermal self emission) have been performed including the apodization for SPIRE. The apodization results

- in a straylight reduction, if the stray radiation originates at (or passes) the rim of the pupil, e.g. for the case of diffraction at the rim of the secondary mirror
- in no relative straylight reduction for those cases, where the stray radiation fills the pupil, because then stray radiation and radiation from M1 and M2 are affected similarly by apodization
- in an apparent straylight increase (in a relative sense only), if the stray radiation is confined to regions near the center of the pupil, because then only the reference beam is apodized appreciably.

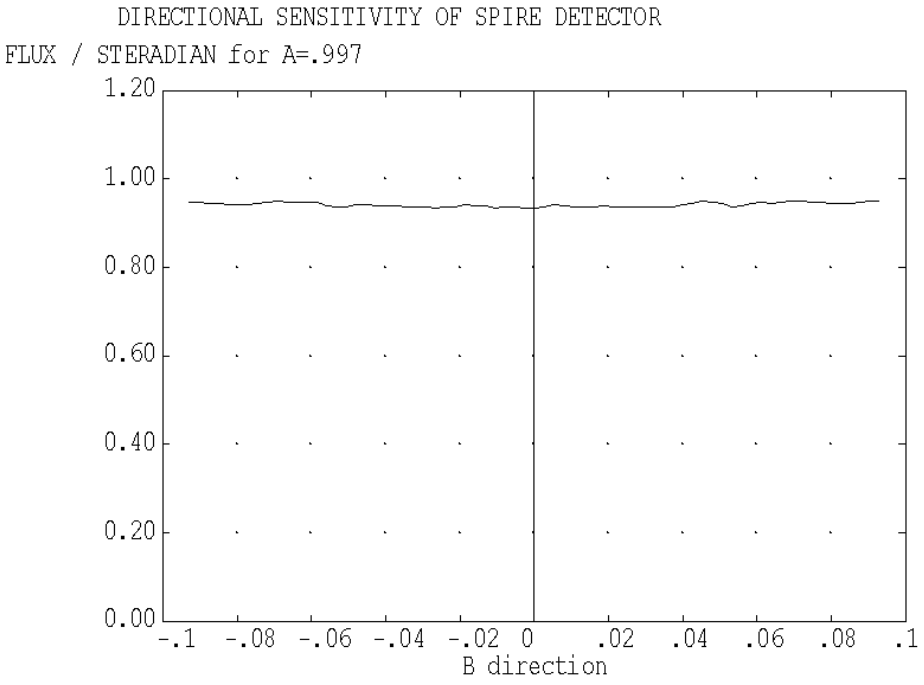

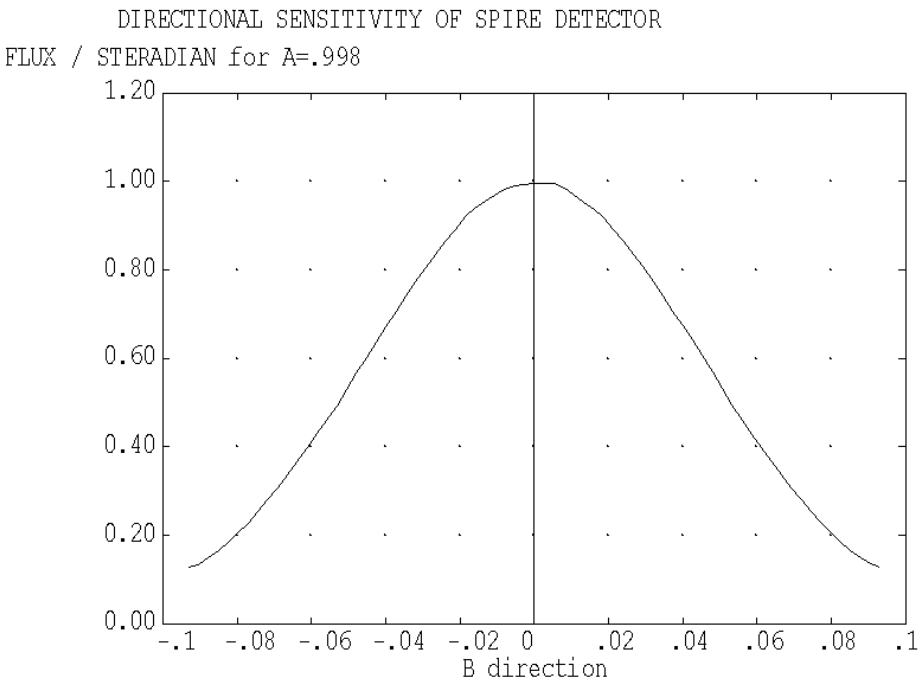

Figure 4.2-6: ASAP apodization function at SPIRE detectors (edge taper of 8 dB)

The scattering functions of the instruments are grouped into 2 categories:

- scattering function for mirrors
- scattering function for thermal filters.

Those for the mirrors were found within the delivered ASAP files. It will become clear later on that they do not play an important role, i.e. mirror scattering within the instruments does not dominate. Therefore the choice of parameters is not important.

The SPIRE mirror scattering function is displayed in figure 11.3-1 in the appendix. It is a particle model with many parameters determining the resulting scattering function. Two PACS mirror scattering functions have been delivered. As a worst case, the higher one has been selected (displayed in figure 11.2-1 in the appendix).

No scattering functions were delivered for thermal filters for PACS. In that case the scattering function was found not important, as a check we inserted an (arbitrarily selected) high function, i.e. a lambertian scatterer with BSDF=0.1/π 1/sr at the place of the cold stop. No important scatter path resulted from this insertion.

For SPIRE a scattering function was received for the thermal filters 1 and 2 (see figure 11.3-5 in the appendix). This function had been measured as reflection function, the rays transverse it by transmission in Herschel. Here the thermal filter 1 may open important scattering paths as the chapters on thermal self emission will show. The reason for the imbalance between SPIRE and PACS with respect to the sensitivity on filter scattering is that the PACS thermal filter is more deeply buried within the instrument than thermal filter 1 of SPIRE.

The scattering functions received for the inner sides of the SPIRE-FP-unit (=input compartment) are displayed in figures 11.3-3 and 11.3-4 in the appendix.

4.3 Telescope model

The telescope models were established by Astrium France. They are described in detail in reference document RD1. Some characteristics and the evolution of changes are repeated here for sake of completeness.

The telescope model now contains the variants

- hexapod with rectangular legs
- hexapod with elliptical legs
- small scattercone with continuous slope change
- large scattercone with continuous slope change.

In issue 1 of the present TN the rectangular legs were included as baseline. Highly effective specular paths towards selected patches of the sky were detected for the rectangular legs.

Therefore the version with elliptical legs was introduced, it shall reduce these specular paths. The elliptical legs are modelled with a polygonal cross section with 24 sides. In issue 2 of the present TN all calculations (i.e. those on thermal self emission) have been performed with the version with elliptical legs.

The specular paths found for the elliptical version are more spreaded over the sky, however they represent less sensitive paths. A comment from the scientists (e-mail from SPIRE dated 31.01.03) states that the minor degree of spreading is favoured, so all the new calculations in this issue 3 (i.e. those on thermal self emission) had been performed with the version with rectangular legs (also the calculations on moon/earth have used the rectangular shape).

The scattercone (also called antinarcissus) was introduced earlier as a reflector placed in the center of the M2 mirror with an extent such that it occupies the area which cannot be used by the Cassegrain telescope type for stellar radiation (central obscuration). The slope had been devised such that backreflections from instrument to M1-baffle via M2 do not occur. As a consequence there was a discontinuous slope change from the M2-surface to the surface of the scattercone. That discontinuity is favourable for avoiding views of the instruments towards the objects in the center of M1 (via M2), however, discontinuities might have an impact on HIFI in terms of standing waves.

Numbers and figures for obscuration and straylight characteristics are listed in sections 5 and 6. Here the reflection behaviour of the three scattercone versions are displayed by the sequence of figures 4.3-1 through 4.3-3. There beams have been generated originating within SPIRE and PACS, these beams were traced backwards towards the M2-assembly. Similar figures have been presented in RD1 for the center of the FOV at the telescope system focus. The figures shown here use the following extreme beams from the edges (at –Z and +Z) of the SPIRE and PACS fields.

	color code in figures 4.3-1 through 4.3-3	
color	beam generated at	beam reflected by
blue	SPIRE, -Z side	scattercone, half at –Z
yellow	SPIRE, -Z side	M2, inner part near scattercone at –Z
black	PACS, +Z side	scattercone, half at +Z
red	PACS, +Z side	M2, inner part near scattercone at +Z

Many calculations in the earlier issue 2 have been performed with the versions with continuous scattercone (small and large).

The different versions have the following properties:

scattercone	small discontinuous	small continuous	large continuous
obscuration ratio, rectangular legs	≈7.7%	7.7%	10.3%
obscuration ratio, elliptical legs	≈8.7%	8.7%	11.3%
energy within 1st dark ring of Airy disk	≈79%	79%	75%
standing waves (HIFI)	present	reduced	reduced
background homogeneity for chopping/nodding	better	worse	better
thermal self emission	lower	higher	lower

The evaluation by the scientists resulted in the favour of the small continuous scattercone (reported in e-mail D.deChambure dated 21.10.2002), mainly because of the better (i.e. smaller) obscuration ratio and the reduced flux of standing waves. All calculations presented in this issue 3 involve the small continuous scattercone.

Another improvement is the abolishment of the chamfers at the transition between scattercone and M2-surface. These chamfers (having the shape of a roof with 45 degrees inclination) introduce a retroreflection in one plane. The programming code received from Astrium France had been changed such that the chamfers are removed (the original model contains them).

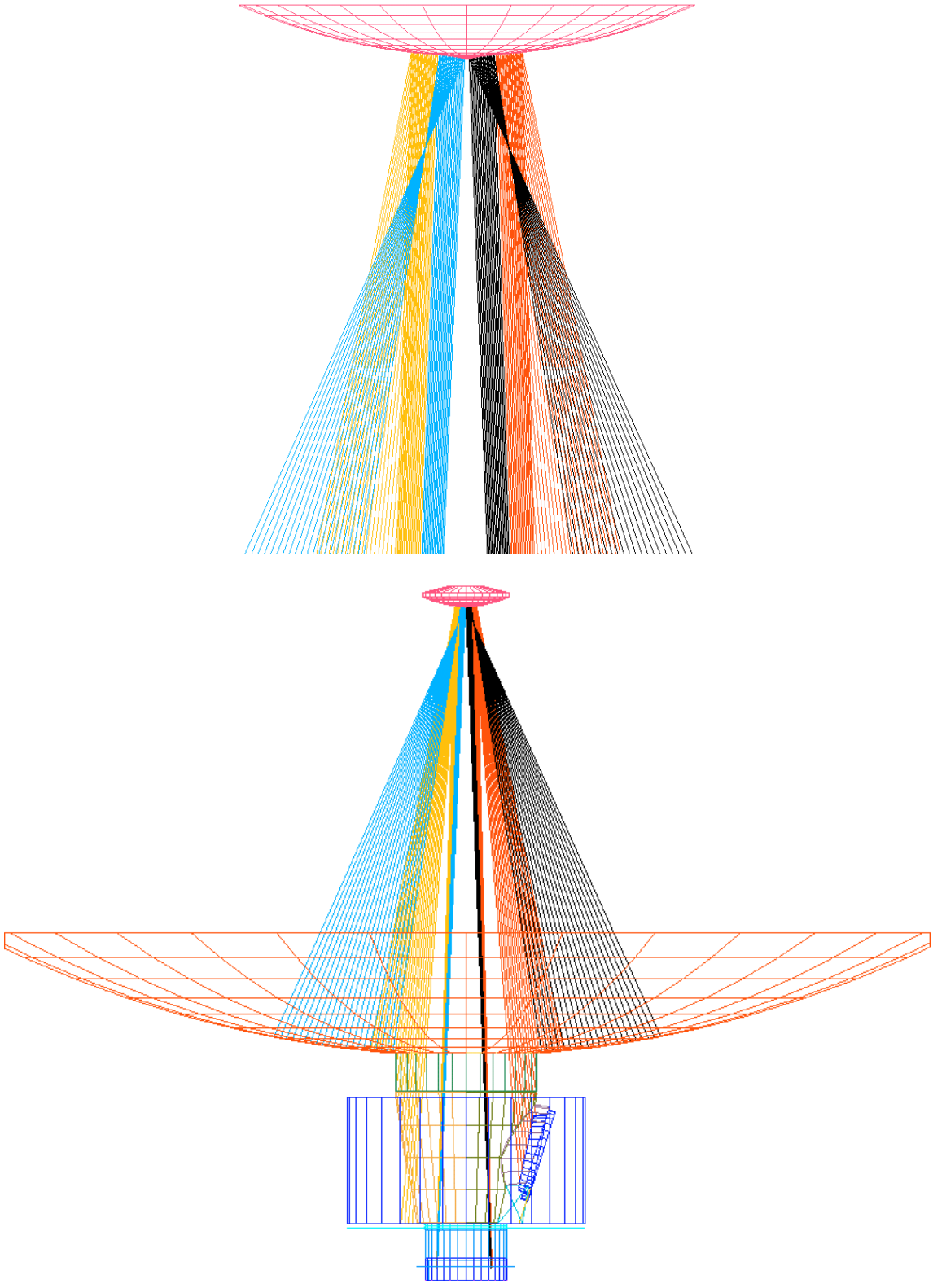

Figure 4.3-1: Back-reflections by the small discontinuous scattercone

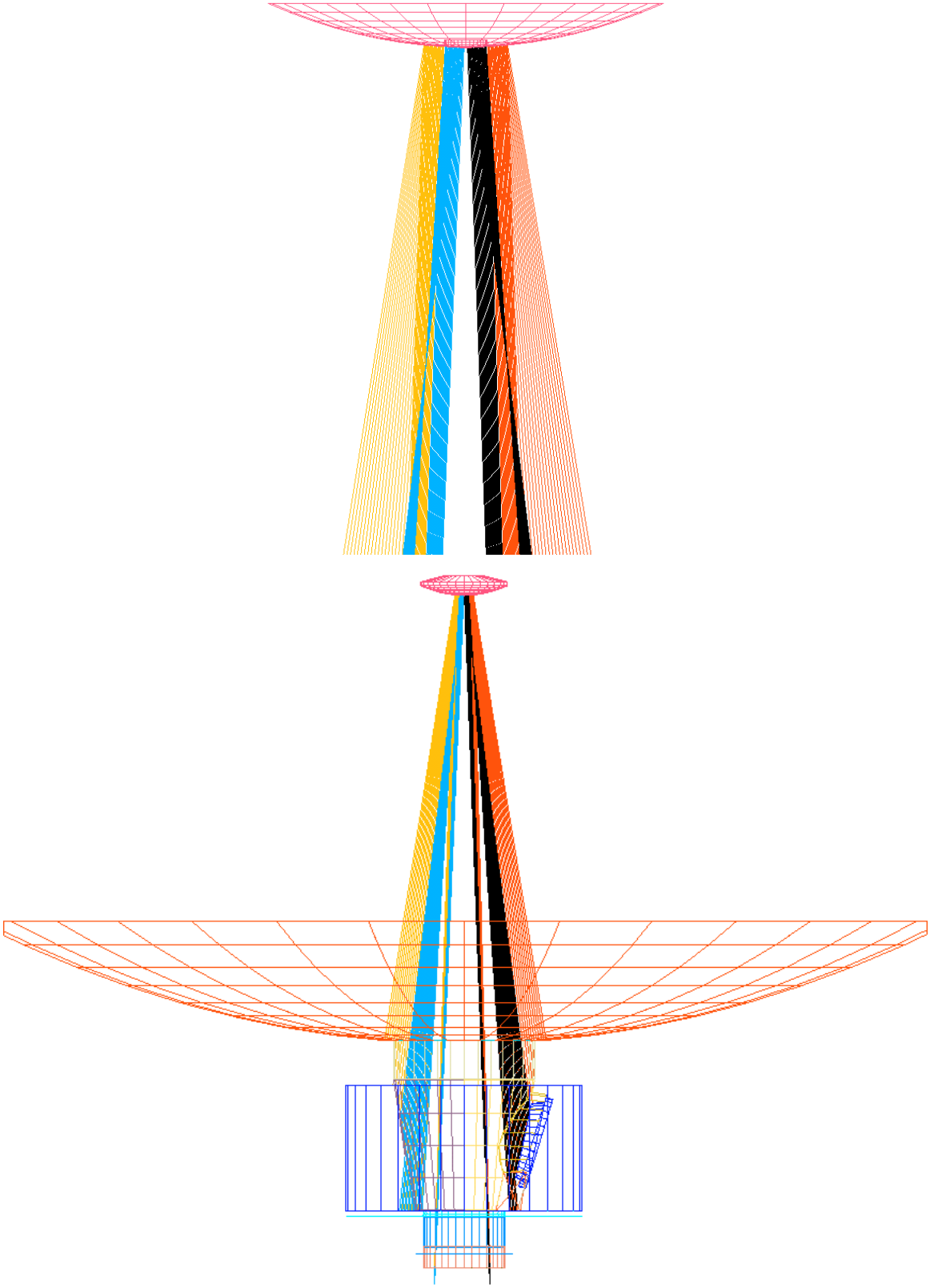

Figure 4.3-2: Back-reflections by the small continuous scattercone

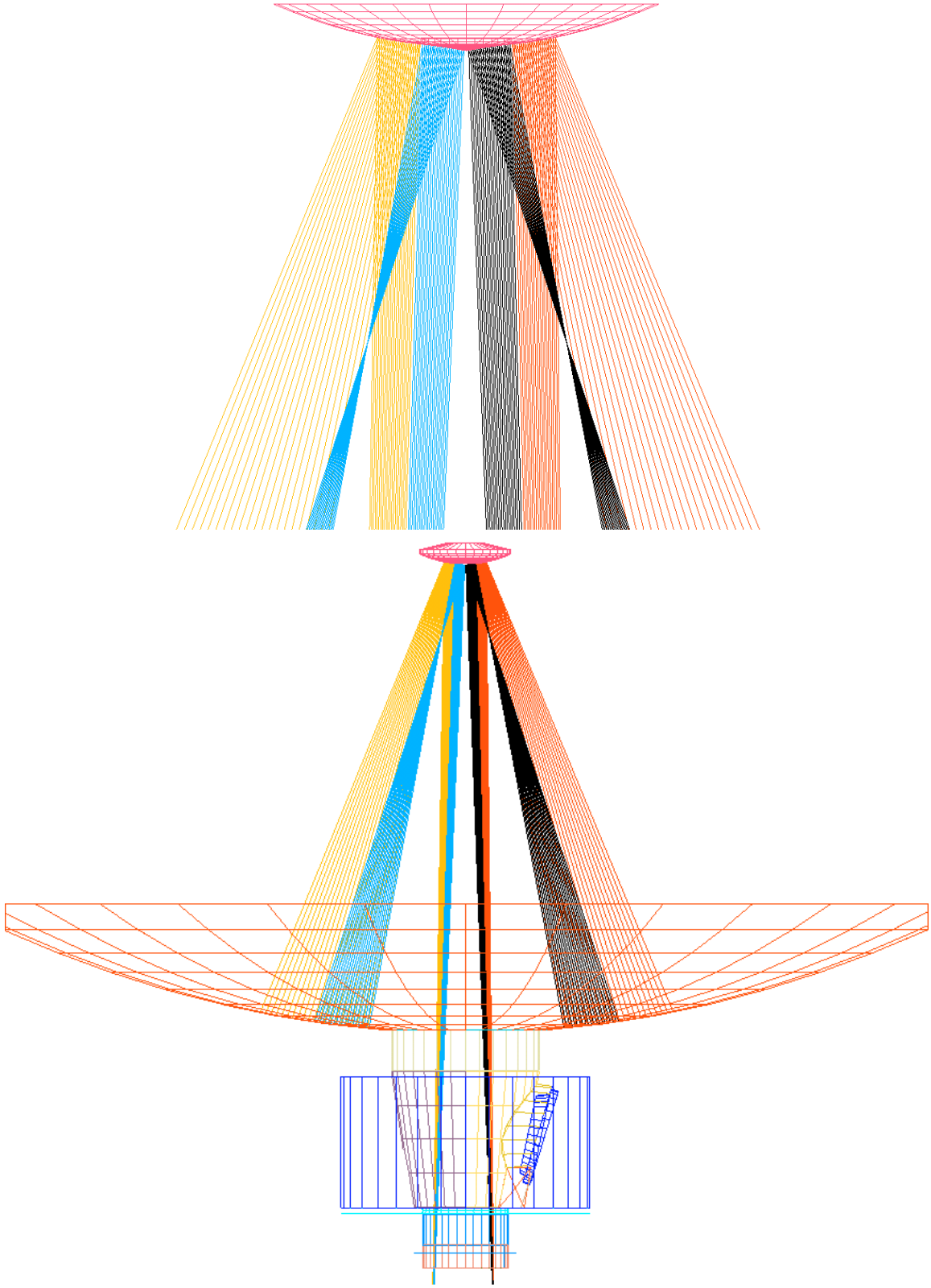

Figure 4.3-3: Back-reflections by the large continuous scattercone

The telescope barrel surfaces facing towards –X have been detected as effective reflecting surfaces for the HIFI instrument. The reflection produces undesirable standing waves. Therefore a change in the barrel surface limitation was introduced, see figure 4.3-4. The inclination of the surfaces is exaggerated there for sake of visibility. The corresponding change in the ASAP telescope model has been performed by ESTEC (sent in may 2003) and is integrated in the overall ASAP model. All calculations presented in this issue 3 include the inclinations shown in figure 4.3-4.

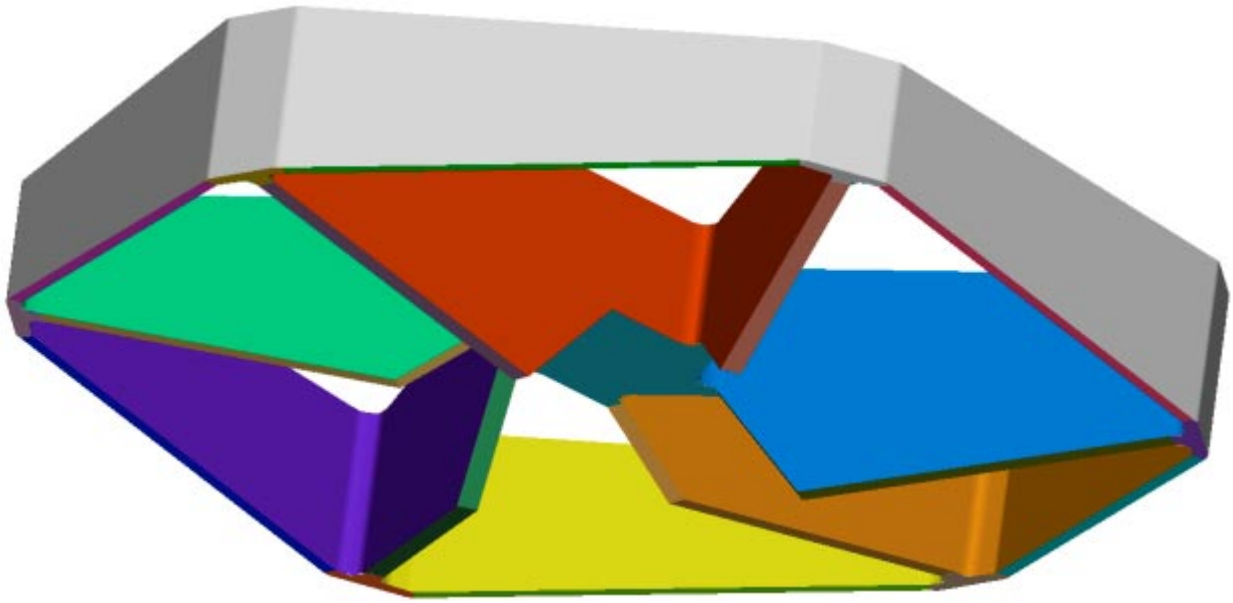

Figure 4.3-4: Change in inclination of the lower hexapod barrel surfaces (the inclination of the surfaces is exaggerated here for sake of visibility). This inclination shall reduce back reflections towards HIFI thereby reducing the standing waves.

A new telescope mirror scattering function (displayed in the appendix in figure 11.1-2) had been delivered by Astrium France shortly after completion of the calculations for issue 2. The new one is higher than the earlier one, it is the basis for all calculations for issue 3 (involving the telescope).

4.4 M1 Baffle and Cryostat Components

The space between the hole within the primary mirror and the cryostat requires attention, since an interface harmonization was necessary there (keyword M1-baffle). The design follows the rules:

- keep warm bodies far off the instrument beam
- avoid zigzag reflections with directions roughly parallel to the x-axis

Zigzag reflections near the y/z-plane are not as critical as they are not likely to reach the instruments. The mechanical needs result in some planes parallel to the Y/Z-plane (e.g. on top of the CVV), so some zigzag reflection paths cannot be avoided.
Also other components around the baffle set constraints, mainly the cyrocover and the accessories necessary for its operation. The lower radius of the M1-baffle reflects the mechanical configuration there.

In issue 1 investigations have been performed for two different designs for the baffle within the centre of the telescope primary mirror (the M1-baffle),

- a cone-baffle
- a cylinder-baffle.

The progress in interface definition w.r.t. the inner rim of the telescope primary led to a restriction of the available diameter of 500 mm for the M1-baffle. Therefore a cylindrical shape has to be chosen for the upper part of the M1-baffle, since a continuous cone from the M1-vertex down to the CVV is not reasonable with an upper diameter of only 500 mm. The lower part can be made conical, the conical shape limits the thermal radiation transport towards the instruments. The resulting cone/cylinder-baffle has been shown already in figure 4.1-2. All the new calculations in issue 2 and issue 3 (i.e. those on thermal self emission) have been performed with that version of the M1-baffle.

The flat ring above the cylindrical part of the M1-baffle (see figure 4.1-2) is part of all calculations in this issue 3. A recent change is the wish of HIFI for a conical shape of the innermost flat part of the M1-baffle. Meanwhile the flat shape has been abandoned and it was decided to give an upwards angle of 3.5 degrees +/- 2 degrees for the upper flat part of the M1 central baffle. The consequences are estimated to be small for general straylight, since it has been verified that

a) no relevant specular rays exist from the sunshade towards the experiments with that new baffle ring
b) the path
sunshade--->scattering on the M1-baffle-ring--->M2--->instruments
is negligible (also with the new tilt).

Several gap closures have been introduced around the (open) cryocover. Thus the so-called ‘inner cavity objects’ (which have been treated in issue 1 as highly emissive objects) now mostly are low emissive objects. Only a small ring around the cryocover has to be treated as highly emitting.

In connection with issue 1 there had been some discussion on the placement of the cryocover relative to the other Herschel components. Status on object positions is

- sun/earth/moon and sunshade at +Z
- cryocover and main mechanics at +Z
- rest of cryocover mechanisms at -Z
- PACS at +Z
- SPIRE at –Z.

The chopping beam motion of the instruments is desired to occur with as much homogeneous background as possible. Therefore the chopping motions are parallel to the X/Y-plane with no appreciable beam motion towards Z. The cryocover position at +Z complies with that intention. The consequence is a possible misbalance of straylight onto PACS and SPIRE from the thermal emitters mentioned.

The surface of the cryocover shall be adequate for establishing a predictable background for the ground tests, i.e. with the closed position of the cryocover. The options and selection of the details of this surface are reported in HP-2-ASED-TN-0076, issue 2. Baseline is now the option with concave mirrors for SPIRE and PACS. The corresponding ASAP commands for these mirrors are applied for all calculations in the present TN.

In order to get the required low temperatures for the instruments during ground testing, the Thermal Shield 2 Aperture was introduced very recently. This additional surface reduces the straylight during ground tests. However, it will add additional straylight for for the orbit case. New calculations with this aperture have been performed only for those straylight paths, where a significant impact onto results was expected.

Three objects are planned to be black due to thermal reasons

- the short cone of the cryocover
- the thermal shield 2 baffle cylinder
- the thermal shield 2 aperture upper side

Partially this choice is disadvantageous for straylight, nevertheless the priority has been given to the thermal reasons. The baffle aperture is a recent addition due to thermal optimization for the ground test case.

The blackening most probably will be an anodizing process, not a sophisticated black color application (as planned for the instruments). Thus, at scientific wavelengths, the anodized surfaces probably will have somewhat lower emissivities than those used for the thermal calculations. Consequently, such calculational differences in the emissivities between thermal and straylight calculations are on purpose.

In summary, the are several gaps

a) between sunshade and the outer rim of mirror M1
b) between M1-Baffle cylinder and M1-Baffle cone
c) between M1-Baffle cone and CVV top plate
d) space on -Z for Cryocover hold down equipment
e) space around open Cryocover
f) between CVV and Thermal Shield 2 Baffle
g) between Thermal Shield 2 Baffle and Instrument Shield
h) between Instrument Shield and Instruments

which are modelled in the ASAP file.

The recent detailed redefinition of gap b) between M1-Baffle cylinder and M1-Baffle cone takes into account that the lower rim of the cylinder is uncertain in X-position within the range of telescope system focus adjustment (other tolerances contribute too). Therefore the gap between cylinder and cone may be as large as 30 mm in the worst case. The straylight and thermal effects of auch a large gap should be avoided, therefore this gap will be closed partly by low emissive material after telescope integration. Only a residual gap will remain open in order to account for vibration and for thermal and pressure movements. This remaining gap will be about 8 mm in orbit at nominal orbit temperatures.

The MLI used for shielding from the radiation of the warm sunshield does not help in the reduction of the apparent emissivity of this gap, because this MLI is located at a larger distance from the M1-baffle.

Due to thermal reasons the space between the CVV and the thermal shield 3 now is closed by the object called crown, a short octogonal object with inner radius somewhat larger than that of the cylinder of thermal shield 2 baffle. The Crown was fully treated for the ground case (RD4), for the orbit case the influence is marginal due to geometry and temperature. Therefore it was sufficient (for the orbit case) to apply an apparent emissivity for the gap with emissivity reduced from 0.9 to 0.5.

4.5 Dimensions used

The most important dimensions as used in the ASAP model are shown in the following table:

Item	Dimensions (mm)
radius of small scattercone	16.5
Z-distance of sunshade	1844 - 12 for MLI = 1832
cylinder baffle radius	250
cylinder baffle height (in X)	adapted to 8 mm gap below
width (in X) of gap between cylinder- and cone baffle	8
cone baffle upper radius	250
cone baffle lower radius	181.6
cone baffle height (in X)	447
width (in X) of gap between CVV and cone baffle	10
CVV height (in X)	21
width (in X) of gap between CVV and thermal shield 2 baffle	14.5
minimum inner radius of CVV	144
inner radius thermal shield 2 baffle	145
height (in X) of thermal shield 2 baffle	118
X-distance of thermal shield 2 aperture from upper edge of thermal shield 2 baffle	30
minimum inner radius of instrument shield baffle cylinder	154
distance between thermal shield 2 baffle lower edge and instrument shield flat	10

The dimensions given are valid for ambient conditions, these dimensions change slightly for the real temperatures (programmed within ASAP)

The large width of the gap between CVV and thermal shield 2 is determined by the situation on ground (vibration clearance under ambient pressure required).

4.6 Emissivities and Temperatures used

a) pessimistic case

The emissivities and temperatures used for the nominal case are listed in table 6.4-1 in connection with the results.

The following remarks are important to note:

Sunshade temperature: The worst case temperatures (EOL, hot case) will be different for the central panel and the side panels. As we did a common raytrace for central panel and side panels in our calculations, we here inserted an average worst case temperature of 204 K (190 +14 uncertainty).
One should emphasize that this is a worst case temperature EOL. Most of the observing time, including hot case BOL will exhibit much lower temperature.

Emissivities of most objects are rough estimates only. They are based on worst case assumptions up to now, not on real measurements.

The emissivity of the gap between sunshade and M1 is an important factor, it was assumed to be 0.9 in issue 2. Therefore the effective emissivity of this gap was calculated in detail in a separate calculation (see chapter 5.3). It turned out to be only about 0.08. In order to account for some uncertainties, this was raised to 0.10.

The evolution of knowledge on the expected telescope emissivity is taken into account insofar as

- the measurements revealed a low emissivity of the telescope mirrors
- consequently the temperature of the telescope mirrors has risen.

Therefore some straylight paths (involving telescope objects) are no longer associated with the 'standard telescope' emissivity and temperature, but with actual ones (in contrast to earlier issues). Some straylight values have changed due to that actualization. However, the reference path (specular reference beam via M1 and M2) is left unchanged in order to facilitate comparison with earlier straylight values (e.g. in issues 1 and 2). Of course, this does not imply that the 'standard telescope' values are the actual ones, the 'standard telescope' is only a fixed reference.

b) optimistic case

The emissivities and temperatures used for the optimistic case are listed in table 6.4-2 in connection with the results.

5 Supplementary Calculations

5.1 Obscuration Calculations

The obscuration effect on throughput for the different versions of the scattercone and the legs is cited from a calculation in RD1:

obscuration ratios	rectangular legs	elliptical legs
small scattercone	7.7%	8.7%
large scattercone	10.3%	11.3%

The obscuration effect on resolution is given in figures 5.1-1 through 5.1-3. The ascending curves represent the encircled energy in percent. The curve for the unobscured pupil (figure 5-1) is given as test for the ASAP routine used for the calculation. The ASAP result is 86% encircled energy at the first dark ring while the theoretical value is 83%. This excess is an artefact of the generation of the figure, i.e. a peculiarity of ASAP. Thus the following figures should be regarded keeping in mind that the values of ASAP are too high by about 3%.

The values for the small and large scattercone are 82% and 78% encircled energy at the first dark ring (figures 5.1-2 and 5.1-3).

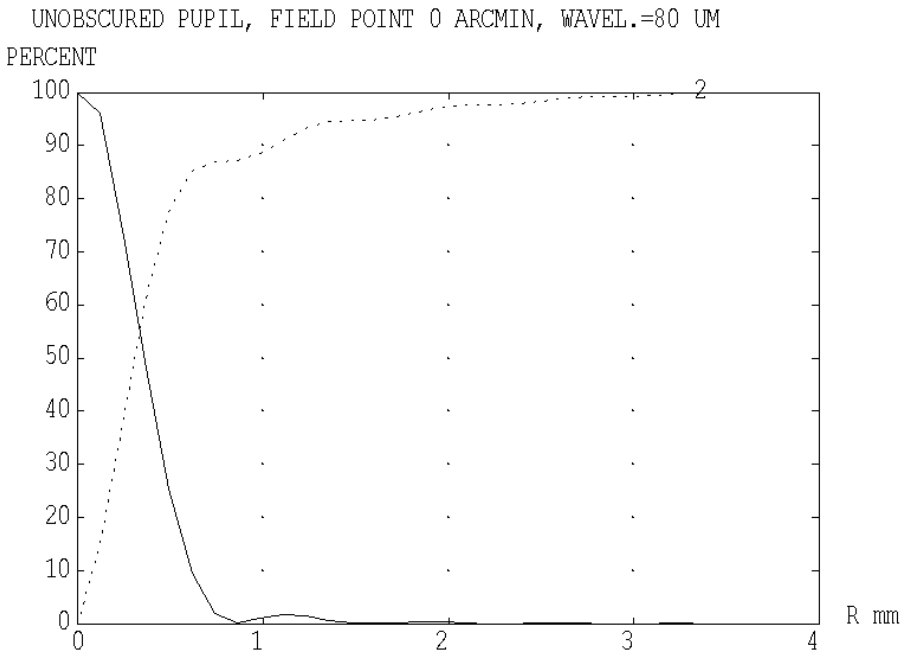

Figure 5.1-1: Radial energy distribution and encircled energy for an unobscured pupil.

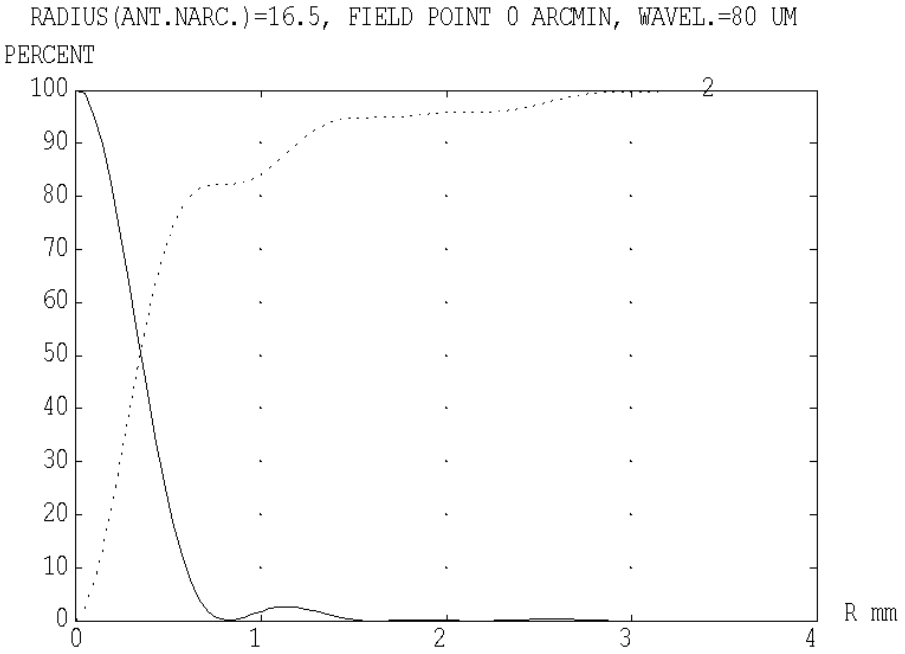

Figure 5.1-2: Radial energy distribution and encircled energy for an obscuration with a scattercone with radius 16.5 mm.

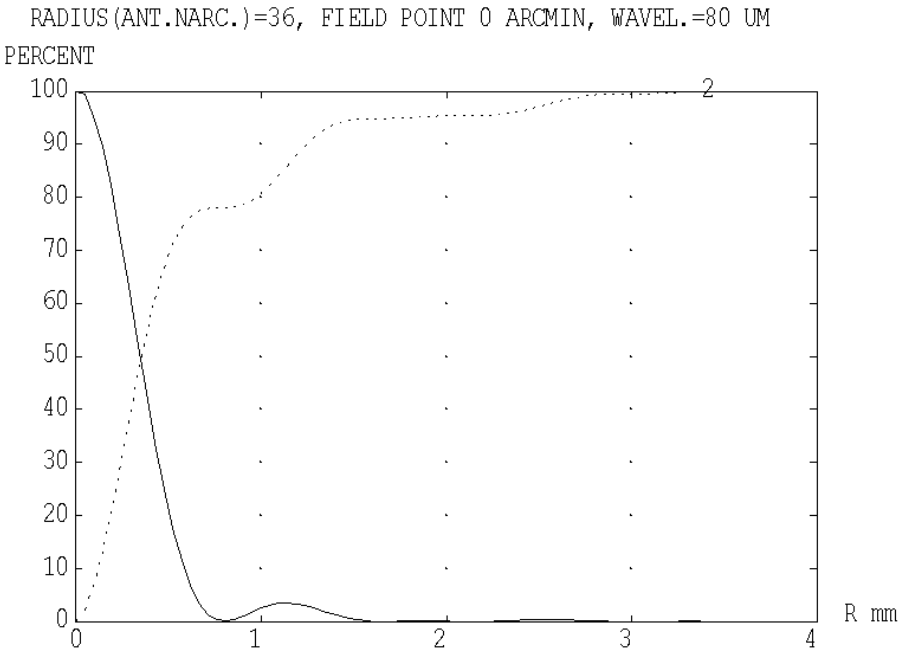

Figure 5.1-3: Radial energy distribution and encircled energy for an obscuration with a scattercone with radius 36 mm.

5.2 Straylight from LOU windows via multiple reflections within the Thermal Shields

Straylight can enter the instruments also from the warm LOU windows, via multiple reflections between the individual thermal shields. One finds:

1) path towards the slit between CVV and Thermal Shield 2 Baffle
2) path towards the slit between Thermal Shield 2 Baffle and Instrument Shield Baffle.
3) path towards the space between Instrument Shield and Instruments itself.

(these paths continue towards the instruments finally).

Path 1) now is supressed by the introduction of the crown between CVV and Thermal Shield 3. The calculations (having been performed earlier) are described in full extent, however only paths 2) and 3) will appear in the summary tables on straylight.

Description of calculations

For reasons of ray statistics, these specific paths were calculated towards the following targets only:

1) gap between CVV and Thermal Shield 2 Baffle (Tube with 14 mm height x 145 mm radius)
2) gap between Thermal Shield 2 Baffle and Instrument Shield Baffle (Ring with outer radius of 154 mm and inner radius of 145 mm)
3) space between Instrument Shield Baffle and Instruments (approximated only by a Tube with about 155 mm height x 154 mm radius)

A separate ASAP model was programmed for this case. The overall view is shown in Figure 5.2-1

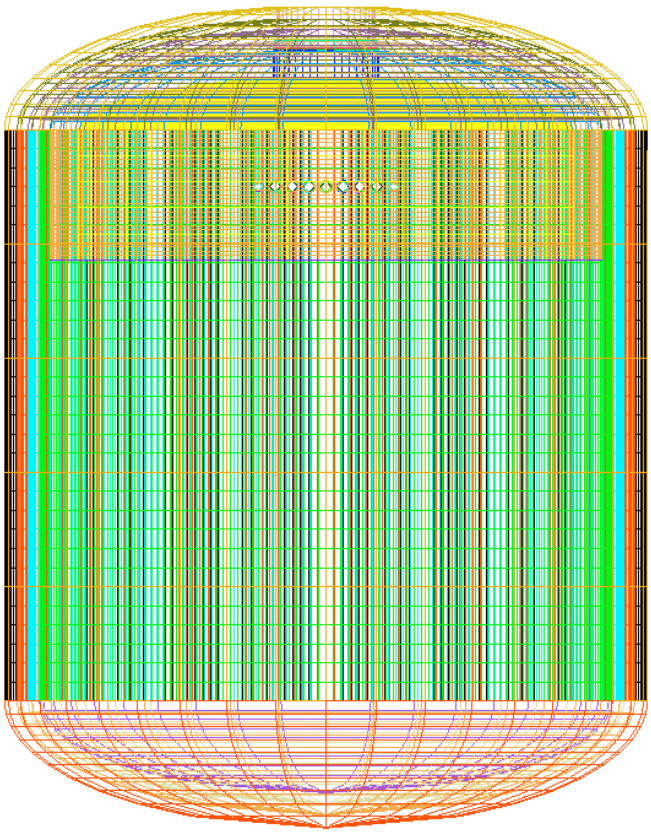

Figure 5.2-1: Overall view of the separate ASAP model.

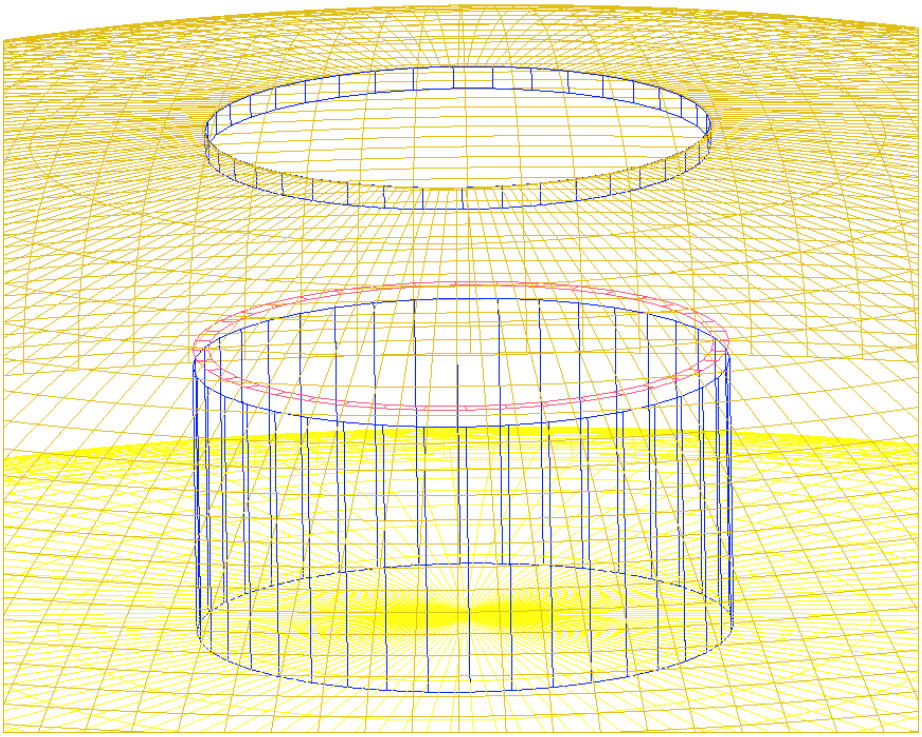

Fig.5.2-2: Detail showing the CVV top sphere, the instruments represented by the lower sphere, and the three target areas in between

The residual calculations from these various gaps towards the instrument detectors are done by the usual raytrace (with the large main ASAP model) by inserting the output from the special raytrace (described here) as a source.

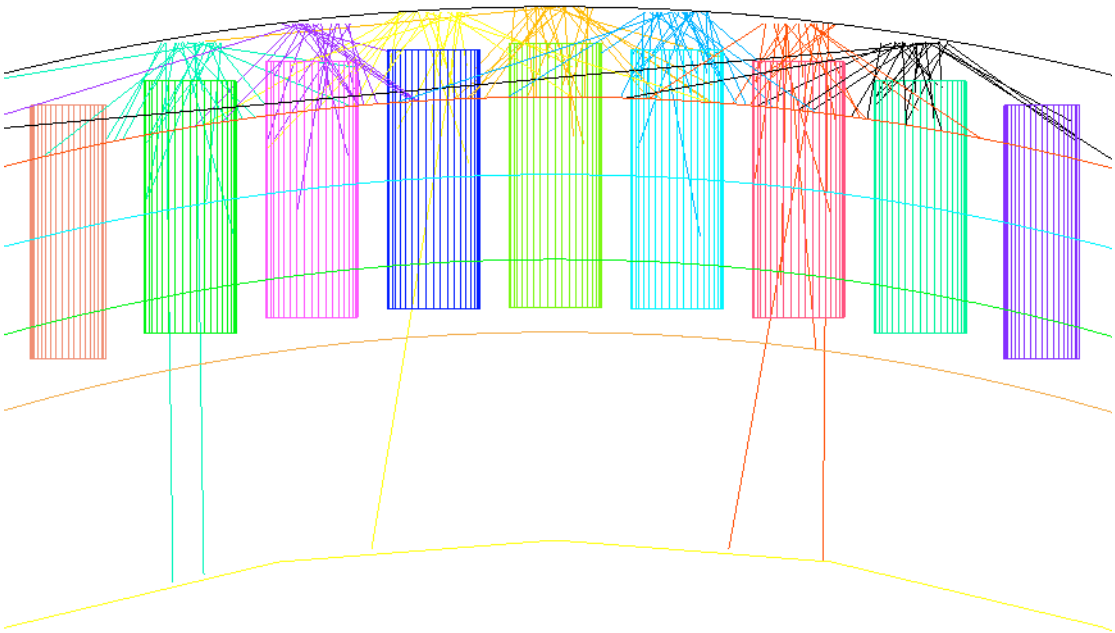

Fig. 5.2-3: Detail showing the location of the sources in relation to CVV and baffle tubes. The different spheres from top to bottom are CVV, Thermal Shields 3, 2, 1, Instrument Shield and Instruments

The rays coming out of the LOU were emitted into the half sphere. Figure 5.2-3 shows the location of the emitting surfaces.

No scattered rays were calculated. However, in order to simulate some minor ray deviations, a roughness random parameter of size 0.02 radian was introduced (for tubes and top spheres only, not for bottom spheres and for LOU baffles), which slightly change the ray direction from pure specular after each reflection on these surfaces. Otherwise every ray will end up on its own path around the system and never can reach a target if it has the wrong initial direction, even if it is reflected 10 000 times. The rationale for this also is that we have MLI on the Thermal Shields which have deviations at least in that order.

Intermediate results

Results have been produced for 2 different cases:

- a worst case calculation with
  - An extreme reflectivity of 0.999 of the CVV, the Thermal Shields and the Instrument Shield.
  - The maximum number of reflections per ray is 10 000.
  - The Instrument reflectivity is 0.95 (non-polished surfaces, with many edges in reality).
  - The reflectivity of the LOU baffle tubes was selected to be 0.8 instead of 0.3 (as for thermal calculations) for the following reasons: The thermal coefficient of ε=0.7 (=reflectivity 0.3) is for shorter wavelengths in the order of 10 microns rather than the wavelengths to be considered here. Usually reflectivity goes up, when the wavelength goes up. Also in reality the reduced reflectivity is for the inner side of the tubes only, whereas in the model there is only one reflectivity for inner and outer side.

- a probable case calculation with
  - A more moderate reflectivity of 0.995 of the CVV, the Thermal Shields and the Instrument Shield.
  - The maximum number of reflections per ray is 2 000.
  - The other parameters (reflectivity of baffle tubes and instruments) are the same as for the worst case calculation.

The 7 holes of the LOU windows (with 34 mm diameter each) have a total area of 6355 mm^2. The ASAP flux emitted from this area into all directions therefore was 6355 (since the standard irradiance of ASAP is 1.0 in our case). It is important to note, that the irradiance at begin into all directions in the normal ASAP calculation with the large main ASAP model (from the targets towards the instruments) is 1.0 too.

The ASAP flux on the targets are

- worst case
  - 383 on target 1 between CVV and Thermal Shield 2 Baffle)
  - 28 on target 2 between Thermal Shield 2 Baffle and Instrument Shield Baffle
  - 271 on target 3 between Instrument Shield Baffle and Instruments

- probable case.
  - 153 on target 1 between CVV and Thermal Shield 2 Baffle
  - 8 on target 2 between Thermal Shield 2 Baffle and Instrument Shield Baffle
  - 243 on target 3 between Instrument Shield Baffle and Instruments

By selecting the worst case, this means that we have to finish the calculation towards the instrument detectors with the temperature of the LOU and the following fluxes from these targets:

- Target 1: flux from 383 mm² area
- Target 2: flux from 28 mm² area
- Target 3: flux from 271 mm² area

The flux from Target 1 now is supressed by the crown. It therefore is not treated further anymore. The intermediate results for the worst case for targets 2 and 3 are treated further in chapter 6.4 (there the final results are listed).

5.3 Calculation of an effective Emissivity for the Gap between Sunshade and M1

In the former issue 2 of this TN, the straylight via the gap between sunshade and M1 was approximated by a worst case assumption. The radiation coming from the S/C structure (part of sunshade below M1 rim, sunshield, CVV outer surfaces etc.) via this gap towards M2 was approximated by the radiation of a black surface (emissivity 0.9) between sunshade and M1, with the maximum temperature of the sunshade. Mainly due to diffraction at the M2 rim, this intense radiation would cause a quite high contribution to the straylight. For this reason, the effective emissivity was analysed with specialised ASAP models.

Model description

a) Extended Model

A separate ASAP file was created, which mainly consists of

- a target in the vicinity of M2
- the sunshade. In this model, it is subdivided into an upper and lower part. The lower part comprises the lower sunshade rim up to the X coordinate of the M1 rim. It emits with a worst case temperature of 204 K. The upper part is not emitting, because only the emission via the gap between sunshade and M1 is calculated here. It only reflects radiation.
- the sunshield. It emits with a worst case temperature of 273 K.
- stiffeners at sunshade and sunshield (1 for sunshade, with the temperature of the sunshade and 2 for sunshield, with the temperature of the sunshield). They emit into both hemispheres.
- the M1 upper and lower surfaces. The lower M1 surface emits with a temperature of 139 K (worst case temperature of the MLI outer facesheet on M1).
- the M1 baffle and CVV cavity. Its outer surfaces emit with a worst case temperature of 127 K.
- The CVV. The upper spherical part of the CVV cavity emits with a worst case temperature of 144 K. The lower spherical part and the cylindrical part of the CVV cavity emit with a worst case temperature of 165 K.
- Radiation shields on + and - Y sides of the CVV cylindrical part. Its surfaces emit with a worst case temperature of 148 K into both hemispheres.
- A radiation shield on -X, -Z side of the CVV. Its upper surface emits with a worst case temperature of 120 K and its lower surface emits with a worst case temperature of 141 K
- The Service Module. It emits into +X half sphere with a worst case temperature of 245 K
- Struts between Sunshade/Sunshield and CVV: The 12 struts are approximated by only 2 struts with 6-fold diameter, in order to represent the correct overall surface size. The temperatures of these struts have been assumed to be 200 K (no information available, because they are not represented in the thermal model).

The selected emissivity for all these surfaces was 0.05. The overall design can be seen in figures 5.3-1 and 5.3-2. As these calculations have been performed already end of 2002, some minor deviations of the configuration ocurred since then. Especially the upper form of the sunshade and the length of the CVV have changed in the meantime. However, the impacts of these changes onto calculation results will be marginal.

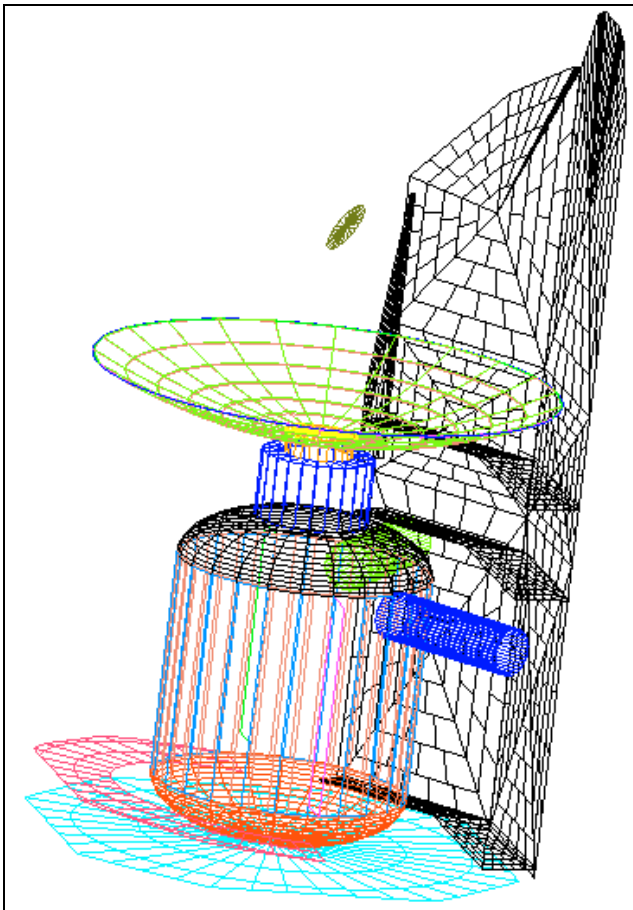

Fig. 5.3-1: Overall view of the Extended Model. For better visibility of some structures, the right part of the sunshade is not shown in the picture.
The small circle above M1 is the target surface for all calculations. This target surface is placed at the location of M2.

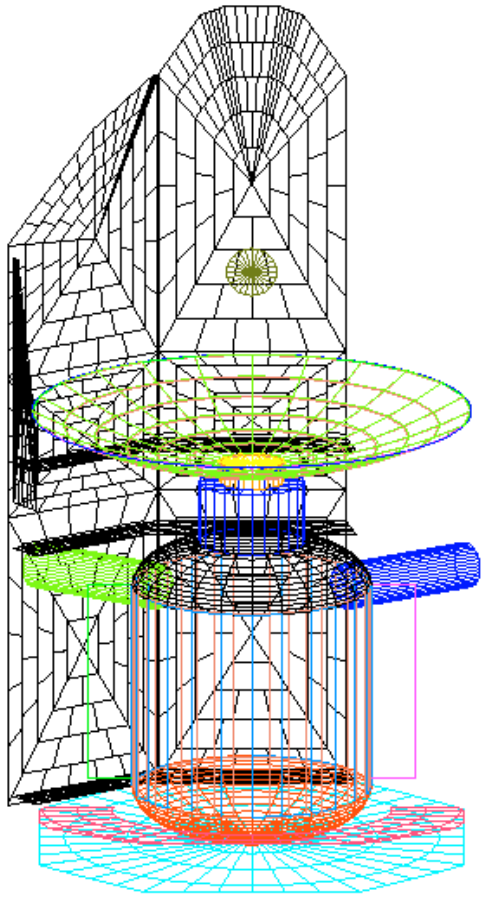

Fig. 5.3-2: Overall view of the Extended Model. For better visibility of some structures, the right part of the sunshade is not shown in the picture.

b) Gap Closure Model.

The Gap Closure Model shall investigate the improvement to be expected from an optional additive mechanical structural element. The intention of this additional surface is to significantly suppress the radiation from the surfaces below.

An additional surface was introduced between the sunshade and M1, 10 mm below the -X edge of the outer M1 rim (see Fig. 5.3-3 through 5.3-5). The Y and Z limits follow the M1 outer rim on -Z side and the sunshade on +Z side. This additional surface also emits into both directions with the worst case temperature of the sunshade of 204 K. The emissivity of this surface also is 0.05.

Fig. 5.3-3: Detailed view of the section between M1 (M1 rim shown on the left side) and sunshade, for the Gap Closure Model. Only the lower part of the central sunshade is shown (vertical line on right side).

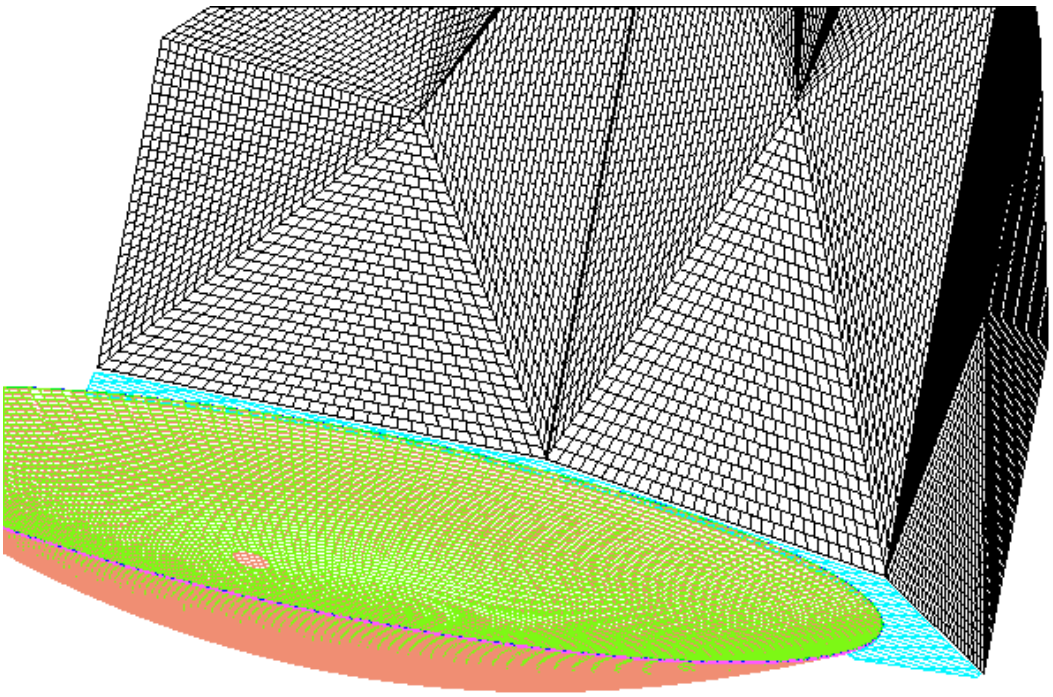

Fig. 5.3-4: Oblique view of the Gap Closure Model. For better visibility, surfaces below the gap and M1 are not shown.

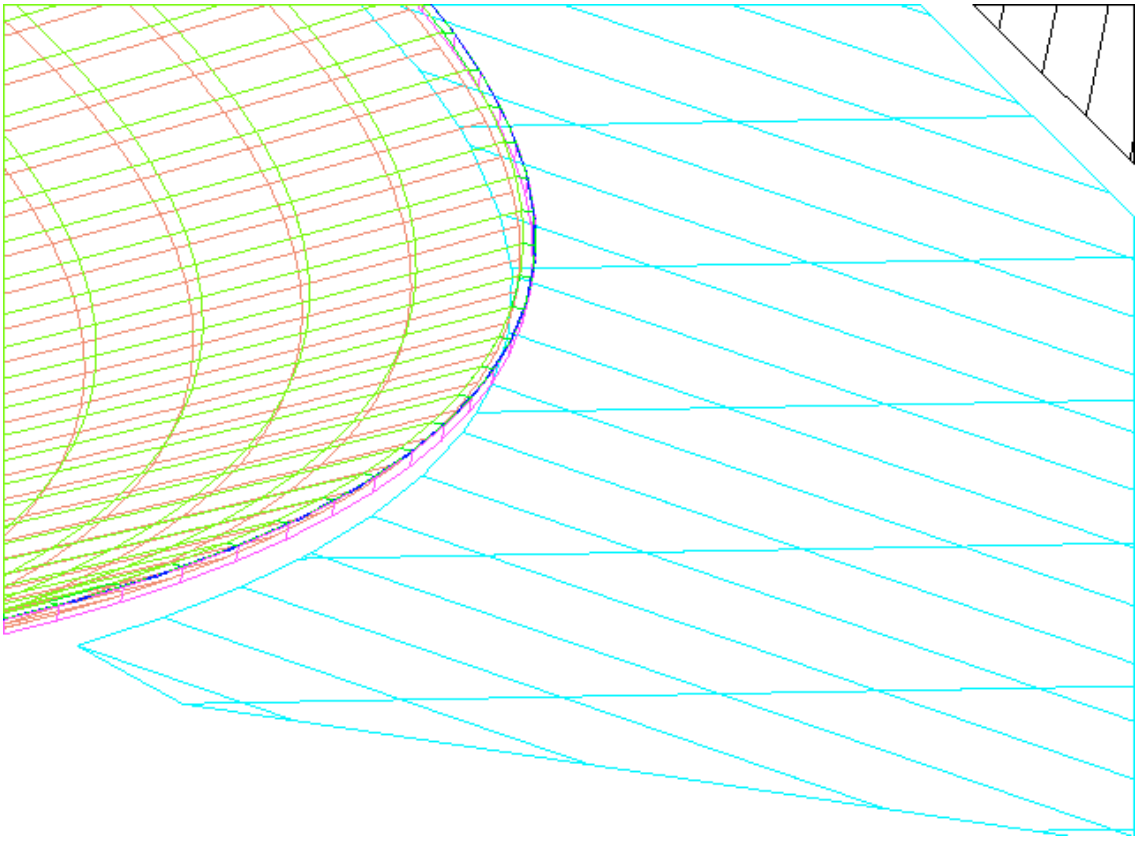

Fig. 5.3-5: Detailed oblique view of the section between M1 (M1 rim shown on the left side) and sunshade, for the Gap Closure Model.

c) Comparative model

The purpose of the Comparative Model is to compare the results gained with the designs of Extended Model and Gap Closure Model with the results gained in the previous standard ASAP calculations for the gap between sunshade and M1.

Fig. 5.3-6: Detailed view of the section between M1 (M1 rim shown on the left side) and sunshade for the Comparative Model with emitting surface between sunshade and M1. Only the lower part of the central sunshade is shown (vertical line on right side).

The Extended Model and the Gap Closure Model contain a target surface at the vicinity of M2 (see e.g. Fig. 5.3-1), since there the additional straylight transport continues (diffraction, scatter). Our Comparative Model also contains this target. In addition it contains the simple apparent surface between M1 rim and Sunshade representing the gap in the normal analyses (chapter 6.4). The Comparative Model uses exactly the same temperature (204 K) and emissivity (0.9) as used in the former issue 2 of this TN. Therefore, by comparing the fluxes at the target surface near M2 of the Extended Model with the Comparative Model we see whether the assumptions on temperature and emissivity for the gap surface between the M1 rim and Sunshade in the usual analyses of chapter 6.4 have to be corrected.

By comparing the Gap Closure Model with the Comparative Model we in fact have a comparison with the Extended Model. So the benefit of the gap closure can be deduced.

Results

Results have been gained for 3 different wavelenghts, 80, 230 and 670 μm.
They are as follows (arbitrary ASAP units):

	80 μm	230 μm	670 μm
Extended Model:	4087	2012	1633
Gap Closure Model	3309	1582	1270
Comparative model:	44342	21106	16919

Table 5.3-1: Radiation on target for different models and different wavelenghts (arbitrary units)

The Comparative Model was with emissivity 0.9 and temperature 204°K. Therefore the corrected emissivities are (if we assume the same temperature of 204°K):

	80 μm	230 μm	670 μm
Extended Model:	0.0830	0.0858	0.0867
Gap Closure Model	0.0672	0.0675	0.0676
Comparative model:	0.9	0.9	0.9

Table 5.3-2: Real emissivities of the gap between sunshade and M1, 204 K assumed.

The results show that the emission from the gap between sunshade and M1 is much lower than assumed in the former issue 2 of this TN. The emissivity for the extended model is in the range of 0.083 - 0.087 instead of 0.9. Due to the simplifications in the model there might be an error in the range of 10 %. **The emissivity of the gap between sunshade and M1 in chapter 6.4 therefore is set to 0.1, at a temperature of 204 K,** because from the values gained it seems not necessary to correct the effective temperature of the gap. The results further show, that there will be no large gain by the introduction of a low emitting foil at Sunshade temperature between Sunshade and M1 (difference between Extended Model results and Gap Closure Model results). The mechanical effort and risk (vibration) are too high for that moderate gain.

6 Thermal emission (Self emission)

6.1 Introduction

For most of the emitting objects, the purely specular paths are the dominant ones. The standard raytrace commands of ASAP have been used for the calculations.

The scattering functions mentioned in the appendix (chapter 11) have been used for those cases where scattering is important (mirrors, filters). The scattering calculations require the definition of a solid angle into which the scattering occurs. For reasons of disk storage and calculational speed, this solid angle is limited as found necessary.

There are no standard ASAP commands available for all cases of diffraction. Therefore the diffraction is calculated separately, see section 6.2. Also the case of thermal emission from the HIFI oscillator window requires some explanation, see section 6.3.

Some remarks follow on wavelength dependence, they start dealing with straylight paths without diffraction.

The requirement on self emission is a number relative to the self emission of the telescope reflectors, therefore the calculations for the different thermal emitters are accompanied by a calculation for the telescope reflectors. The diffuse emitting raygrids within ASAP all have a 'standard' emitting radiance of $1/\pi$ per mm^2 per steradian. The raytrace yields a total flux value for the SPIRE/PACS detectors. The flux onto the detectors from a specific thermal emitter (e.g. the sunshade) is divided by the sum of fluxes onto the detectors calculated for M1 and M2 yielding the desired relative number. Any units (e.g. Watt per µm on the detectors) disappear due to that division. So there is no necessity to deal with units (provided the same 'standard' emitting radiance is used both for the thermal emitter and the telescope mirrors).

If the specific thermal emitter has the same emissivity/temperature as the reflectors, then the relative flux is the final result for that emitter. If not, then the relative flux has to be corrected with two factors:

- Temperature correction factor: thermal emission with the temperature of the emitting object divided by thermal emission of the 'standard telescope' with 70 K. This temperature correction factor depends on the wavelength, two Planck functions are involved (that of the emitting object and that of the 'standard telescope').
- Emissivity correction factor: emissivity of object versus emissivity of the 'standard telescope' with 0.015 for a single mirror. This emissivity correction factor depends on the wavelength (but is treated as such only, if the wavelength dependence is known).

The results are values averaged over the respective detector area. They are valid for the specific wavelength applied when calculating the temperature/emissivity correction factors, i.e. monochromatic. Results are given for two wavelengths per instrument.

No wavelength dependence is furnished by ASAP's raygrids, such items have to be inserted by the user of ASAP (if necessary)

1. either by changing the flux of the diffuse raygrids immediately after creation
2. or by manipulation of the results (in an excel file) after the ASAP raytrace.

The second strategy is chosen almost always because ASAP's raytrace is the time consuming step of the job. If that is done with some appropriate 'standard' values, then a change in boundary conditions (emissivity, temperature) does not require the repetition of the raytrace, only the trivial manipulations of the results (new temperature/emissivity correction factors) in an excel file have to be repeated. This is true for the case of a single thermal emitter in a specific raytrace (single emissivity, single temperature), most calculations have been done with that strategy. Wavelength dependence thus enters when performing the multiplication in the excel file.

However, there are some exceptions in the analysis: if several emitters with different emissivities and temperatures are traced simultaneously, then strategy 1.) is used, the wavelength dependence enters before the raytrace.

The diffuse scattering occurring during some traces could be wavelength dependent; however no wavelength dependence has been entered, since no wavelength dependence has been delivered to us or is known to us (the only exception is scattering by the mirrors of SPIRE, but the corresponding paths have negligible flux). In some cases the reflectivity (=1.0-emissivity) of some walls could be wavelength dependent along zigzag paths towards the detector (i.e. after the emitter). However these paths are not the dominant ones; in such cases the worse case (i.e. the worse wavelength) is entered.

The diffraction calculations described in section 6.2 either use

- ASAP's coherent module, there the wavelength has to be specified before the calculation
- the method of stationary phase, there an input of wavelength is necessary too.

Some informations on the wavelength behaviour are listed below:

a) the diffracted irradiance is known to vary as proportional to wavelength far off the specular beam
b) the irradiance at the centre of the diffraction disc varies as 1/(wavelength)^2 for a point source (also for a line source perpendicular to the line extension)
c) the comparison with the telescope radiation yields an additional wavelength dependence (described above).

For Herschel, the relevant diffraction usually occurs in a situation between a) and b) with an additional influence of c), so a 'theoretical' prediction for a wavelength dependence is hardly possible; only the calculation will show the real dependence.

6.2 Diffraction Calculations

6.2.1 Introduction

Three methods are used for the diffraction calculations

- method of stationary phase
- method with Fresnel-Integrals (after Born & Wolf, only for comparison).
- ASAP's coherent field synthesis

The coincidence of two or three methods gives confidence that the numerous radiometric multiplications with solid angles, areas of emitting/receiving surfaces etc. are correct.

The method of stationary phase is fairly general in application. The results are correct even for large angles of diffraction. Very close (roughly < 1 degree) to the shadow limit the results tend to approach infinity and must be clipped.

The method with Fresnel-Integrals is restricted to simple cases (at least in the example worked out in Born & Wolf), therefore it is used only as a check in order to verify the results of the other two methods.

ASAP's coherent field synthesis may be applied for geometries where a coherent wavefront can be traced across the objects in question without disturbing the following field synthesis of ASAP. The method is less accurate, if large diffraction angles occur.

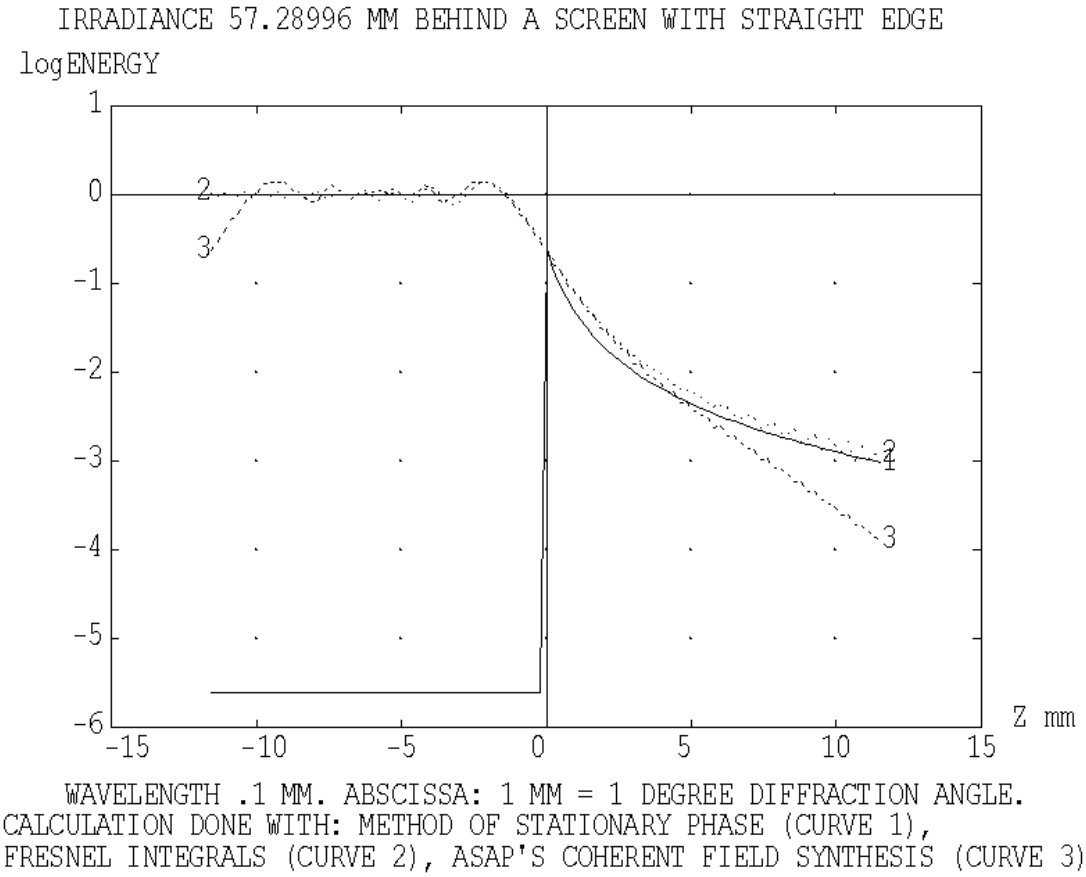

Figure 6.2.1-1: Diffraction behind a straight edge calculated by three methods (wavelength is 0.1 mm).

These properties can be seen in figure 6.2.1-1, i.e. a simple case selected only for the purpose of comparison. The irradiation impinging on a screen with straight edge is a plane wave (i.e. the source is at infinity). The intercepting plane is 57 mm behind the screen. On the left side there is the illuminated half while the shadow is on the right side. Near the shadow limit the linear dimension in mm coincides with degrees of diffraction angle (it is proportional to the tangent of the diffraction angle). The logarithm(10) of the relative irradiance is plotted as obtained with the three methods. The line for the method of stationary phase has not been calculated in the illuminated region (therefore drops to quasi zero).

The cases treated/mentioned in the next chapters are

- diffraction at the rim of apertures in the telescope focal surface
- thermal emission from the gap of the sunshade diffracted into the field of view by the rim of the secondary mirror.

The case with the secondary mirror as diffracting edge is a special case, since this diffracting edge can be seen by the detectors. It is imaged onto the rim of the cold stops / chopper elements probably without any appreciable clipping. Thus a single diffraction at the rim of the secondary is sufficient to redirect radiation onto the detectors. The case with the gap around the cryocover (and other similar cases) is different. At least another scattering/diffracting process is required before the diffracted rays enter the field of view. The reason for that is that all candidates for diffracting edges

- either cannot be seen by the detectors directly
- or are not irradiated by strong sources.

6.2.2 Diffraction at the rim of apertures in the telescope focal surface

The diffraction at the SPIRE opening was treated in issue 2 with a relative comparison with the specular irradiation. In the meantime, a more sophisticated calculational scheme for diffraction at the rim of apertures in the telescope focal surface has been generated for the case of ground testing. This scheme delivers diffracted irradiances on the detectors, thus is considered much superior than the treatment done in the earlier issue 2. Therefore the earlier calculation is abandoned in favour of the new one.

The new calculational scheme is described in detail in HP-2-ASED-TN-0076 issue 2. That TN contains the most stringent circumstances for that case, i.e. radiation from the warm objects around the cryocover during ground testing. No comparable warm objects are present in the orbit situation. Therefore no similar calculation is necessary here for the orbit case.

A supporting short calculation is mentioned here which compares the irradiances onto the SPIRE/PACS input surfaces

1. rays from the warm objects around the cryocover (during ground testing)
2. rays from the sunshade zigzagging down towards the instruments (in orbit).

The latter irradiance is more than a factor of 10 smaller than the first one, also emissivity and temperature of the sunshade are even more favourable than the case 1), the ground test. So the conclusion is correct that diffraction at the rim of apertures in the telescope focal surface is not important in orbit, i.e. less than 1%.

6.2.3 Diffraction at the rim of the secondary mirror with the gap near the sunshade as thermal source

As mentioned already, the diffracting edge of M2 can be seen by the detectors. It is imaged onto the rim of the cold stops / chopper elements probably without any appreciable clipping. Thus a single diffraction at the rim of the secondary is sufficient to redirect radiation onto the detectors. Therefore a calculation of the diffracted radiation impinging on the telescope focal surface is sufficient for a judgement of that straylight case.

ASAP's coherent field synthesis was chosen for that calculation, since it is straightforward to include the two obscuring hexapod legs into the analysis (it would be quite laborious to do the same with the stationary phase method). 29 coherent point sources are placed along the gap, they radiate towards the rim of the secondary mirror. The beams are propagated onto the telescope focal surface. There the coherent field synthesis is done separately for each source. Afterwards the irradiance of each source is added incoherently. Figure 6.2.3-1 gives an impression of the beams used for the calculation. The beams of two sources are clipped partially by two hexapod legs, so a possible diffraction effect by the legs is included. The instrument structure is not included, since the intention is to present a broader distribution of the diffracted radiation on the telescope focal surface in the graphs. The small instrument openings would include only a small fraction of the spatial distribution of the irradiance.

The radiance of the source is set to the same value as usual in our thermal calculations (=1/π 1/(sr*mm^2)), so a comparison with the radiation of the telescope mirrors can be done easily. The usual correction factors for emissivity (=0.10) and temperature (204 K) for the gap near the sunshade are applied. The radiating gap has an area of 8520 cm^2. Compared to issue 2, the new effective emissivity of 0.10 (calculated in chapter 5.3) leads to a substantial reduction in the corresponding straylight value. It no longer represents a strong straylight source.

A normalization of the mirror contribution to 100% is included as usual. Thus the curves presented here are to be interpreted as in the earlier analysis: a value of 1.0 (or 0 in the log(10)-diagrams) corresponds to 1% of the thermal radiation of both telescope mirrors.

The irradiance is plotted across the Y-coordinate in figure 6.2.3-2, across the Z-coordinate in figure 6.2.3-3. The positions of PACS and SPIRE are near Z=+80 and Z=-90 mm. Both diagrams are valid for a wavelength of 0.23 mm, thus touch both wavelength regions of PACS and SPIRE. The corresponding figures 6.2.3-4 and 6.2.3-5 are valid for 0.67 mm wavelength (SPIRE only), see also figures 6.2.3-6 and 6.2.3-7 for 0.08 mm wavelength (PACS only). The positions of the scans are listed in the figure subscripts.

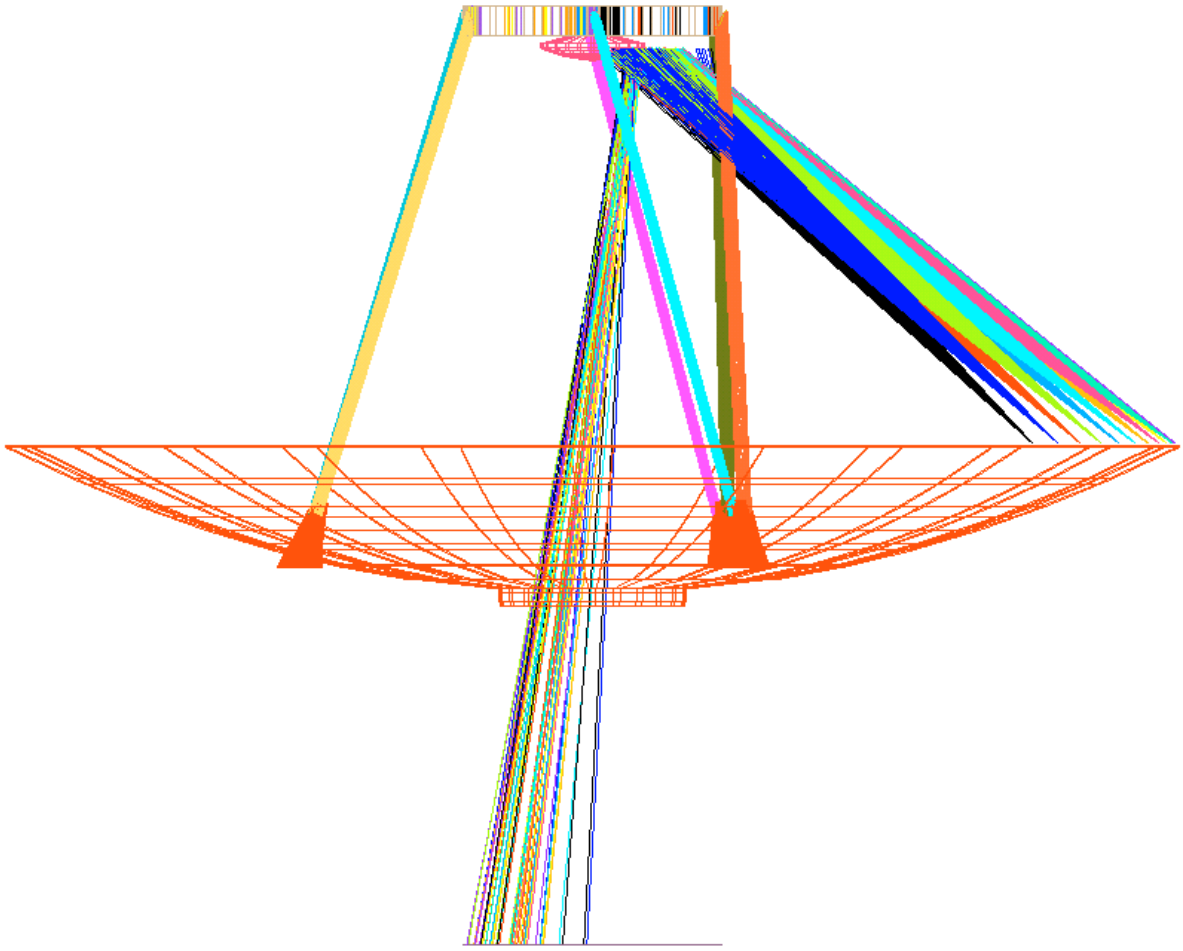

Figure 6.2.3-1: Beams used for the calculation of diffraction at the rim of the secondary mirror. Source is the gap near the sunshade.

The resulting straylight is read from the figures mentioned. For SPIRE, one has to take into account that the rim of the secondary is seen with reduced sensitivity due to the edge taper of 8 dB (or reduction from 100% to 13%) introduced by the horns of SPIRE. The edge taper is not included in the figures which represent the pure diffraction variation. So the numbers for SPIRE (taken from the figures) are reduced by the factor 0.13. The results are

wavelength	0.08 mm (PACS)	0.23 mm (PACS)	0.23 mm (SPIRE)	0.67 mm (SPIRE)
irradiance	0.3%	0.5%	0.4%	1.3%

All the numbers describe a worst case situation for the gap as described in chapter 5.3. This complies with the average temperature of the sunshade set at 204 K, i.e. the thermal hot case.

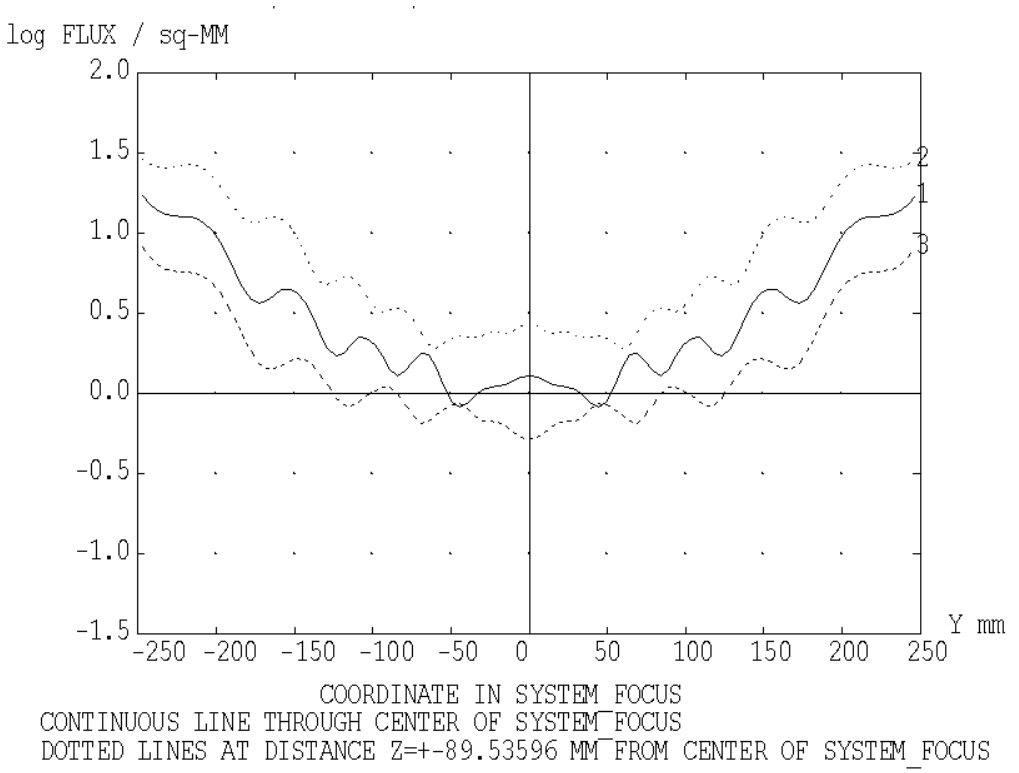

Figure 6.2.3-2: Irradiance on system focal plane with scans across Y-coordinate (wavelength 0.23 mm)

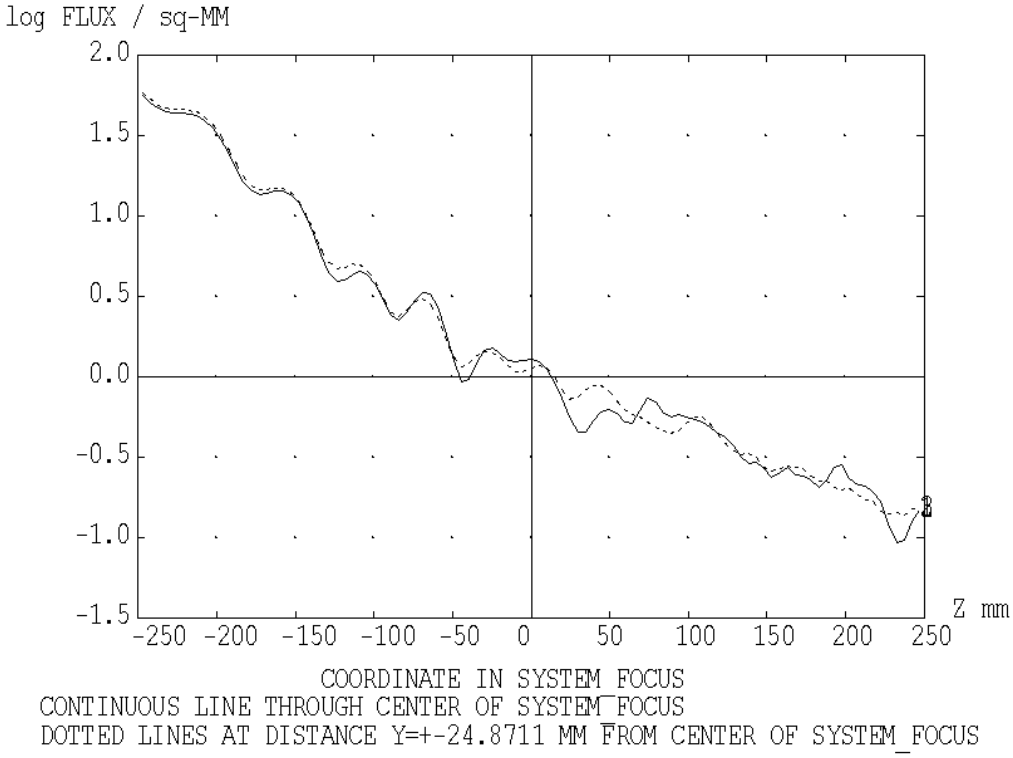

Figure 6.2.3-3: Irradiance on system focal plane with scans across Z-coordinate (wavelength 0.23 mm)

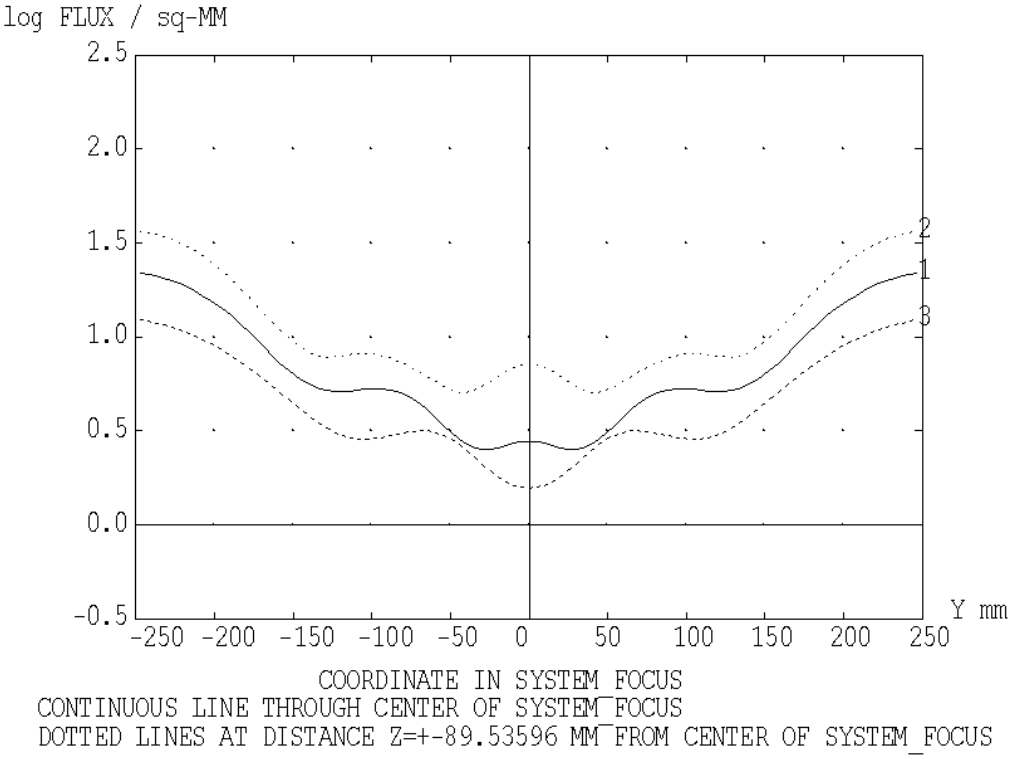

Figure 6.2.3-4: Irradiance on system focal plane with scans across Y-coordinate (wavelength 0.67 mm)

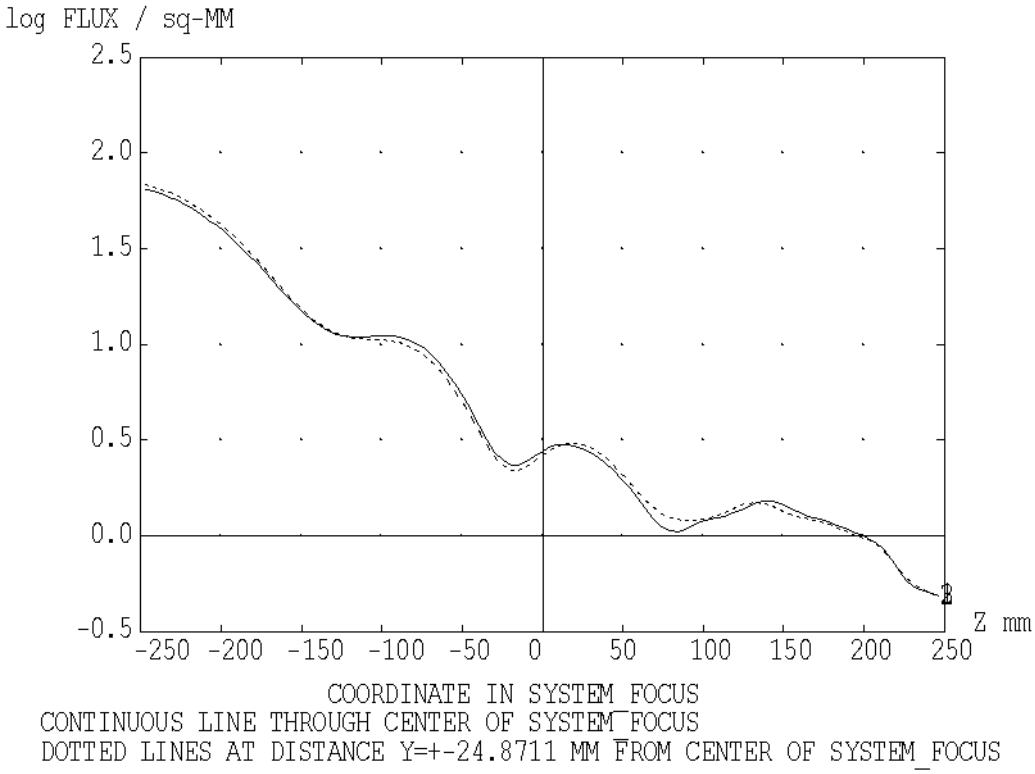

Figure 6.2.3-5: Irradiance on system focal plane with scans across Z-coordinate (wavelength 0.67 mm)

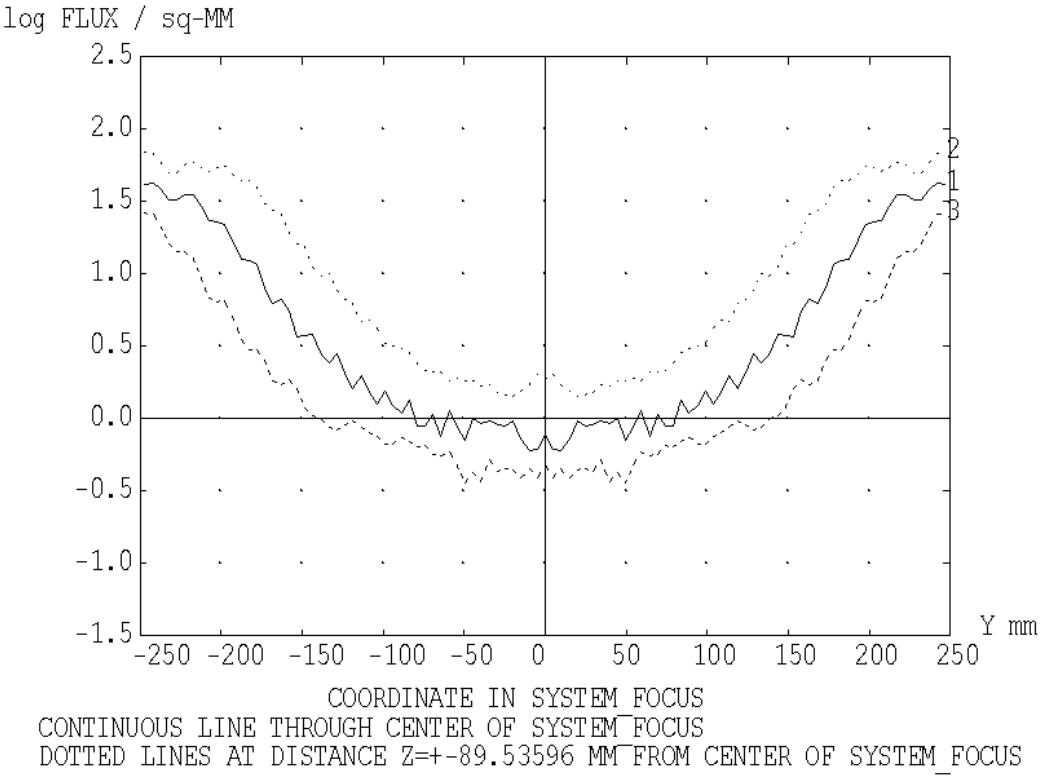

Figure 6.2.3-6: Irradiance on system focal plane with scans across Y-coordinate (wavelength 0.08 mm)

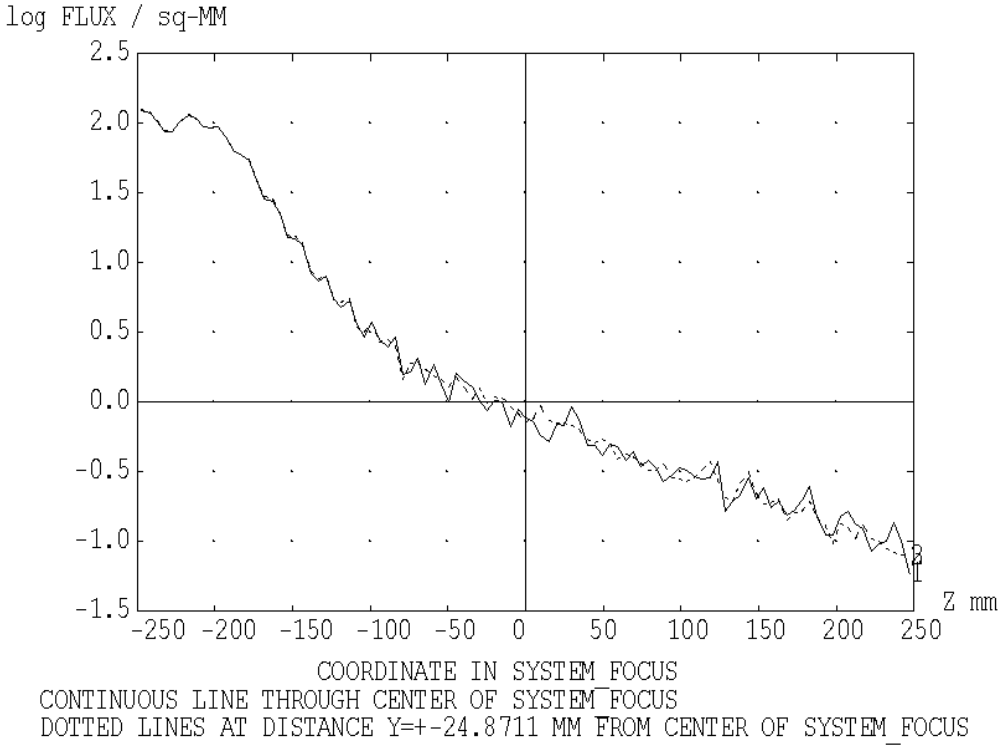

Figure 6.2.3-7: Irradiance on system focal plane with scans across Z-coordinate wavelength 0.08 mm

As mentioned, a complete comparison with the method of stationary phase was not programmed due to the complexity with the hexapod legs and the distribution of sources along the gap. Nevertheless, a partial comparison has been worked out by setting only a single source in the gap at Y=0. For that case (which does not represent the complete radiometric situation) a relative comparison has been programmed with the method of stationary phase. A scan across Z-coordinate at Y=0 in the telescope focal surface is the result shown in figures 6.2.3-8 (wavelength 0.2 mm) and 6.2.3-9 (wavelength 0.67 mm). The method of stationary phase (as applied) does not contain such a refinement in its mathematics that fringes could appear; however, the overall comparison is acceptable. At the shadow limit the curve for the stationary phase tends to infinity, therefore it has been clipped as usual (at the position of the dip which is not real).

The comparison shows that ASAP's coherent field synthesis is acceptable for the case of diffraction at the rim of the secondary of a source nearby the nominal beam. The fringes seen in figures 6.2.3-8 and 6.2.3-9 are less salient in the preceeding figures, since there an incoherent superposition of several coherent sources along the gap has been calculated. The results of the coherent calculation depend somewhat on the input parameters (number of rays etc.). Thus the accuracy of the results certainly has to be considered with caution, we think it is not better than a factor of 3...5. ASAP's coherent field synthesis obviously is approaching its limits for such calculations.

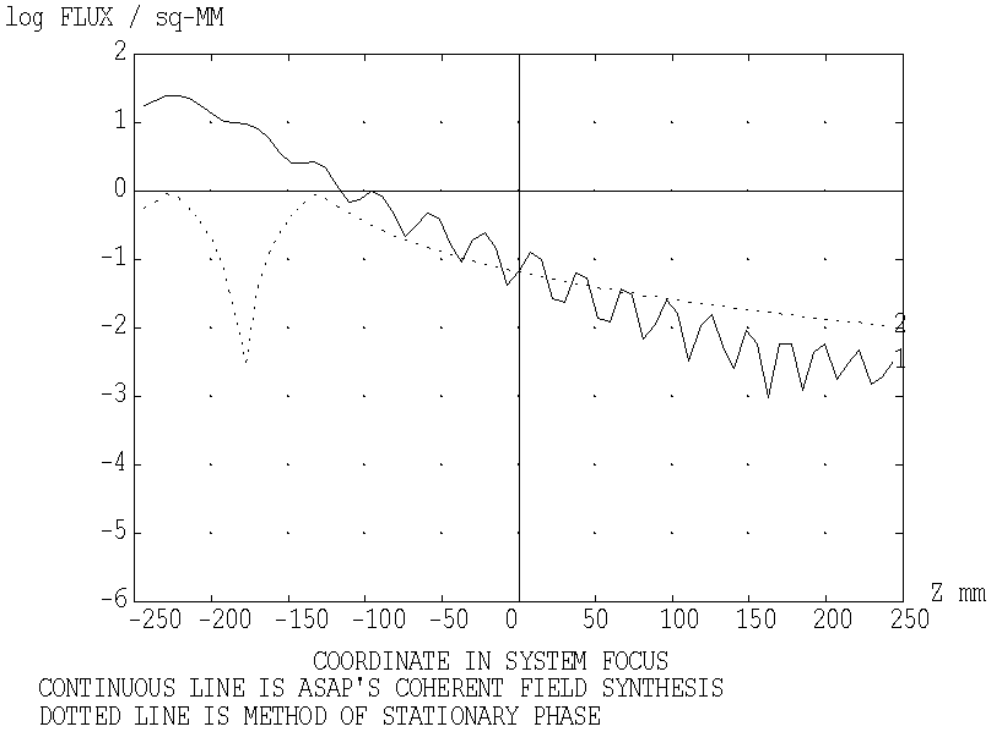

Figure 6.2.3-8: Relative comparison of two methods with a single source in the gap diffracted at the rim of the secondary mirror, wavelength = 0.2 mm

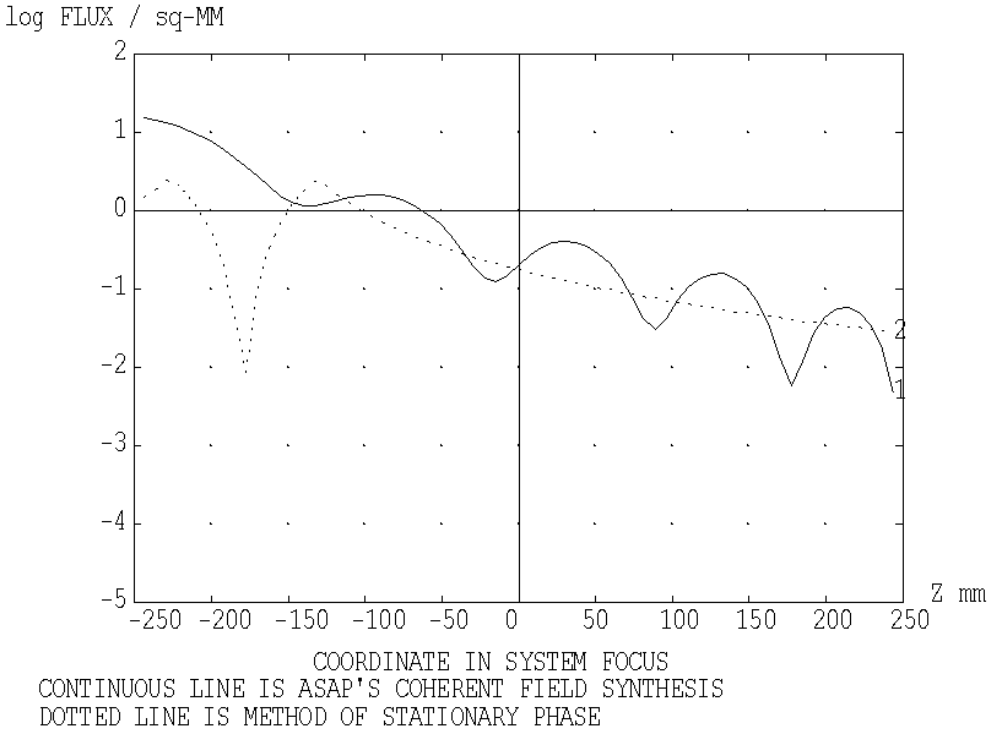

Figure 6.2.3-9: Relative comparison of two methods with a single source in the gap diffracted at the rim of the secondary mirror, wavelength = 0.67 mm

6.3 Thermal Emission from the HIFI Oscillator Window

The windows for feeding the oscillator radiation into the cold instrument region also feed in thermal radiation. This case has been treated in the earlier issues as a worst case calculation. Since then, the temperature of the LOU has decreased slightly. Nevertheless, a repetition of the calculation is not considered necessary due to the application of the 'worst case' philosophy here. So the tables with the results list the recent temperatures, a correction for temperature would change the small numbers by less than 13%.

We assume a black thermal radiation of temperature 150 K there, with no restriction of the solid angle (i.e. hemispherical). The ASAP HIFI model contains mirrors and housing walls. The walls are quoted to have a reflectivity similar to that of mirrors, so we adopt a reflectivity of 0.99. Both the mirrors and the walls transport the thermal radiation towards the internal opening of HIFI, i.e. towards HIFI mirror M3. From there the radiation aims at +X-direction.

A first trial with a lambertian emitter at the oscillator window position with the PACS and SPIRE detectors as receiving surfaces failed. The large number of zigzag reflections within HIFI did not lead to reasonable results. Therefore the whole path was split into several steps

a) transmission of thermal radiation through the HIFI compartments (stepwise)
b) radiation onto PACS and SPIRE (via the M2-assembly) from a fictive thermal emitter at the HIFI opening near M3.

Step b) is described first. The black thermal radiation of temperature 150 K assumed at the oscillator window is placed at the HIFI opening near M3. The resulting radiation (via the M2-assembly) towards PACS and SPIRE clearly represents a worst case. The numbers found are 4.2% (PACS) and 5.3% (SPIRE) (with 100% as contribution of the telescope reflectors). They are not negligible, therefore it is necessary to calculate step a) too.

The transmission of thermal radiation through the HIFI compartments is calculated for

- compartment 1
- compartment 1 plus 2.

the compartment numbering is shown in figure 6.3-1.

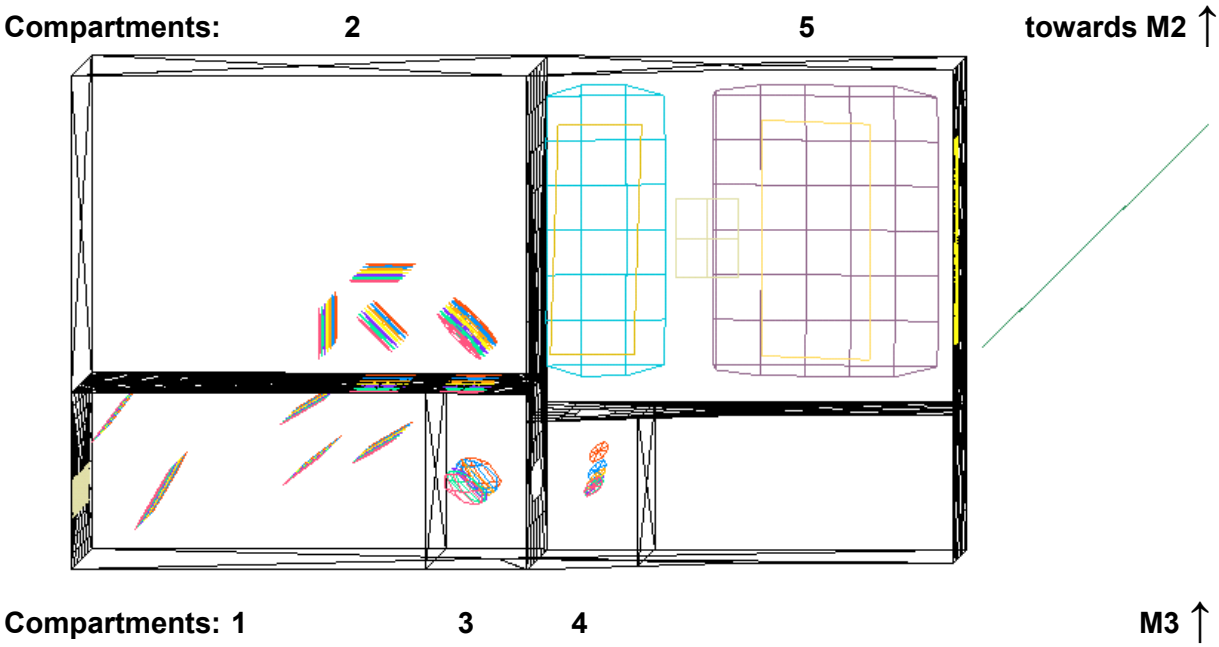

Figure 6.3-1 ASAP-HIFI model with compartment numbering. The numbers increase from the local oscillator windows (lower left side) to the inner opening towards M3 and M2 (telescope secondary mirror).

The transmission calculations start with lambertian sources at the LOU window, the transmission is evaluated as the ratio of the fluxes out/in. The results are

Compartment	Transmission
1	0.3
1+2	0.09

The numbers depend strongly on the wall reflection assumed to be 0.99.

There are 5 compartments; the table above indicates that each compartment yields a transmission with factor 0.3, 5 compartments could give 0.3^5=0.0024. Although only compartments 1 and 2 have been calculated, it is safe to state that the total transmission for all compartments is smaller than 0.01. So the numbers of worst case of step b) now reduces to <0.04% (PACS) and <0.05% (SPIRE). These numbers are small enough for the statement that the thermal radiation from the HIFI oscillator does not play an important role.

6.4 Results

Since the requirement on self emission is a number relative to the self emission of the reflectors, all calculations are done without use of a unit for flux (e.g. Watt). The emitting raygrids within ASAP all have an emitting radiance of $1/\pi$ per mm^2 per steradian. The raytrace yields a total flux value for the SPIRE/PACS detectors. The flux onto the detectors from a specific object (e.g. the sunshade) is divided by the sum of fluxes calculated for M1 and M2.

This relative flux for the specific object has to be corrected with two factors:

- Temperature correction factor: thermal emission with the temperature of the emitting object divided by thermal emission of the 'standard telescope' with 70 K. This temperature correction factor depends on the wavelength.
- Emissivity correction factor: emissivity of object versus emissivity of the 'standard telescope' with 0.015 for a single mirror.

The results are values averaged over the respective detector area.

The contribution of the standard telescope has been set to 100 so:

- the violation of the 10% thermal emission requirement occurs if the numbers exceed 10.

The table 6.4-1 gives an overview on the expected pessimistic situation for the case with the rectangular cross section of the Hexapod legs and the small scattercone, as selected by the scientists. All temperatures comply with recent thermal calculations (mostly 'hot case' plus uncertainty), there are differences to earlier issues, mainly for the telescope.

For most of the emitting objects, the purely specular paths are the dominant ones. However, some paths do not follow this rule, there is a corresponding remark, if necessary. If nothing is indicated, then the values are the sum of 'specular' and 'scattered' (whereby specular dominates).

Table 6.4-1: Self emission onto PACS/SPIRE detectors, pessimistic case.

Emitting object with temperature T and emissivity ε	T [K]	ε	PACS 80 µm	PACS 230 µm	SPIRE 230 µm	SPIRE 670 µm
Sunshade (scattering on M1+M2 + spec.)	204	0.05	2.329	1.099	0.614	0.493
Gap Sunshade-M1 (scattering on M2)	204	0.10	1.000	0.472	0.092	0.074
Gap Sunshade-M1 (diffraction at M2-rim)	204	0.10	0.300	0.500	0.400	1.300
Hexapod	90	0.02	5.885	4.477	5.721	5.298
M1+M2 (without reference path)	90	0.005	1.557	1.185	0.898	0.832
Scattercone	90	0.005	0.388	0.295	0.000	0.000
M1-Baffle flat	90	0.05	2.161	1.644	1.423	1.318
M1-Baffle cone / cylinder	79	0.05	4.032	3.496	0.537	0.516
Gap betw. M1-Baffle cone and cylinder	79	0.90	1.172	1.016	0.237	0.228
Cryocover mirrors + plate	73	0.02	0.251	0.238	0.010	0.009
Reflecting objects near Cryocover	73	0.05	0.492	0.467	0.086	0.085
Cryocover black rim	73	0.80	1.621	1.539	0.236	0.233
Black gaps around Cryocover / M1-Baffle	73	0.80	3.306	3.138	0.378	0.373
CVV plate top	73	0.05	1.147	1.089	0.074	0.073
Gap betw. CVV / Thermal Shield 2 Baffle	73	0.50	0.213	0.202	0.064	0.063
Thermal Shield 2 Baffle (only specular)	47	0.80	0.631	1.220	0.634	0.757
Thermal Shield 2 Baffle (only scattering within instrument)	47	0.80	0.286	0.553	1.170	1.399
Thermal Shield 2 Aperture (upper side)	47	0.80	1.613	3.118	0.529	0.633
Thermal Shield 2 Aperture (lower side)	47	0.05	0.069	0.134	0.120	0.144
Instrument Shield Baffle	16	0.05	0.000	0.007	0.001	0.003
Gap below Instrument Shield Baffle	16	0.90	0.002	0.373	0.018	0.077
LOU via HiFi	140	0.90	<0.040	<0.040	<0.050	<0.050
LOU via gaps (below Instrument Shield Baffle etc.)	140	0.90	0.110	0.061	0.003	0.002
Holes in OB for cooling straps (with view onto Thermal Shield 1 by reflection)	36	0.90	0.029	0.110	0.005	0.008
sum			**28.6**	**26.5**	**13.3**	**14.0**

Data for PACS and SPIRE are in % with 100% = telescope irradiation
('standard telescope' with 70 K, total ε=0.03)

There are some positions in the tables which cause significant differences compared to issue 2.

Telescope

The BSDF for the telescope mirrors has changed significantly. The same BSDF also was used for other parts outside the CVV and therefore exposed to ambient/contamination conditions.

The contributions from the hexapod structure and the side paths via M1/M2 are different from those in issue 2, there the values from RD1 have been cited. For the present issue, those straylight contributions are based on new calculations in order to allow for

- the geometry changes of the hexapod (inclinations of the lower barrel surfaces)
- SPIRE and PACS are represented with their actual location near the telescope system focus
- SPIRE is represented with the edge taper (apodization) of the detector horns and the central blockage of its pupil.

The contributions involving the emission from M1 and M2 via side paths in table 6.4-1 are influenced by the details mentioned above. For SPIRE the central pupil blockage is important eliminating the contribution of the scattercone.

The emission from the hexapod for SPIRE is larger than for PACS in table 6.4-1. This is due to the fact that the emission from M1+M2 (on the reference path, used for normalization) is influenced by the SPIRE edge taper while only a marginal influence exists for the emission from the hexapod (inner part of the pupil, not the very centre).

Comparison SPIRE-PACS

Some differences between SPIRE and PACS are due to their different location in the focal region of the telescope. But more important is the fact that the ASAP model of SPIRE has a central blockage of the pupil. Whether this blockage in reality will be as good as in the ASAP model, depends on problems of misalignment etc. Thus the values for SPIRE in some cases could come closer to those of PACS in case of misalignment. Nevertheless, some differences will always be present due to the apodization across the pupil realized by SPIRE.

The different locations of the first filter element in SPIRE/PACS also contributes to differences in straylight, e.g. from the thermal shield 2 baffle.

Marginal paths

Many paths found are 'marginal' paths, they involve small solid angles within the path, i.e. a small angular redirection of the rays is sufficient for a blockage of that path. An example is shown in figure 6.4-1 dealing with the mentioned beam limitation on the pupil, i.e. M2. It is clear that the values for the marginal paths have to be considered with caution, since usually only few rays find their way to the detectors due to the small solid angles. Some of these paths are marginal only in terms of solid angle, but not in terms of flux.

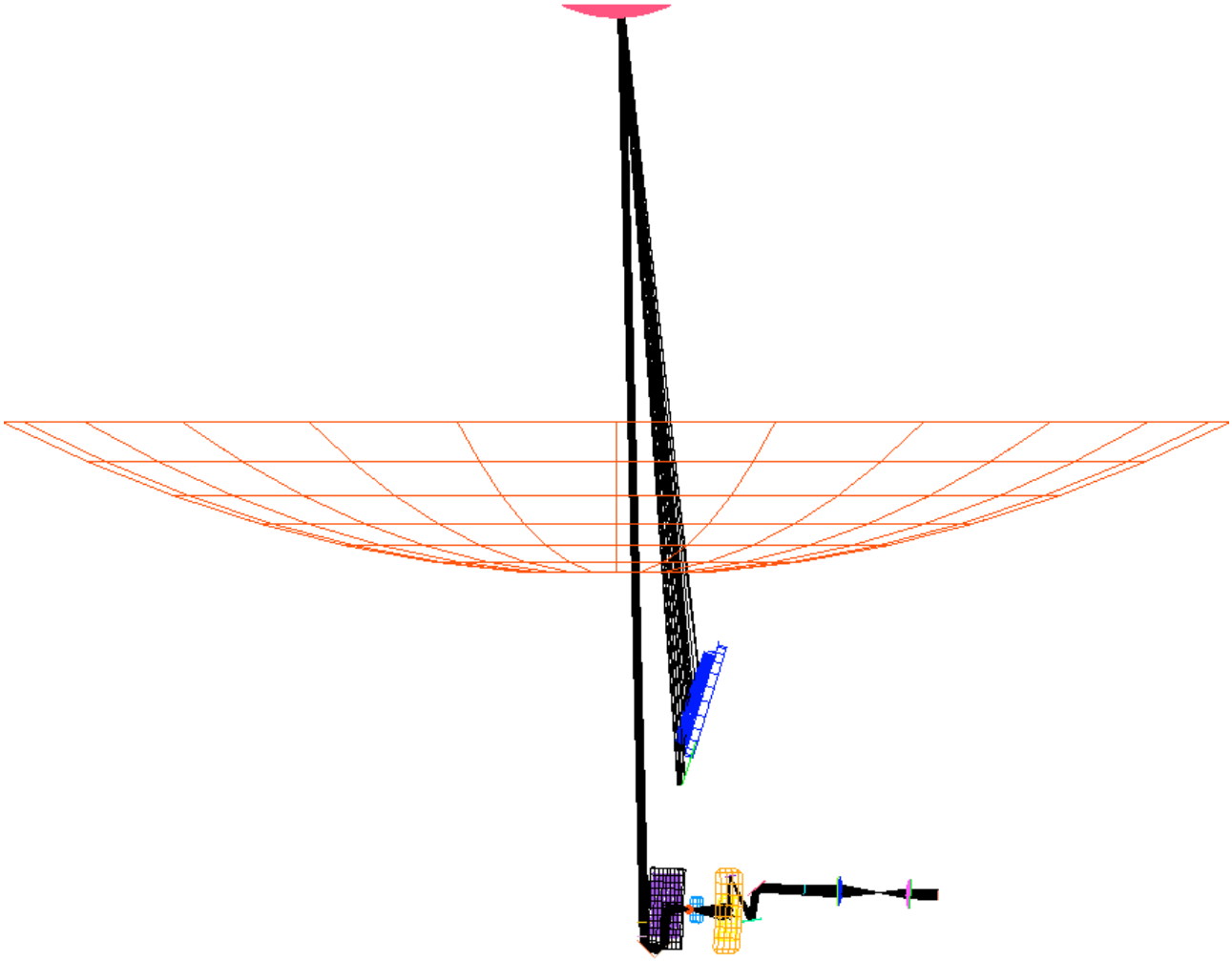

Figure 6.4-1: Marginal path involving the small solid angle of visibility of the M2 surface to the PACS detector.

Sunshade

The contributions from the sunshade have a specular path via the chamfer on the outer rim of M2. If this chamfer is not as regular as it is simulated in the present ASAP model, then this path is reduced to some extent. Presently this path contributes 50% of the value for PACS for the line 'sunshade' (less for SPIRE). Another specular path contributing another 20% for both PACS and SPIRE is

sunshade ---> M1 ---> hexapod base in M1 ---> M2 ---> PACS/SPIRE

The haxapod base object is named M1.FITT_COVER1 in the ASAP file received from ASTRIUM France.

Gaps

The emissivity of the gap between sunshade and the outer rim of mirror M1 has been calculated to be only 0.1 (see chapter 5.3) instead of 0.9 as assumed in issue 2. This eliminates the necessity to cover this gap with a low emitting foil.

In summary, the are several gaps

a) between sunshade and the outer rim of mirror M1
b) between M1-Baffle cylinder and M1-Baffle cone
c) between M1-Baffle cone and CVV top plate
d) space on -Z for Cryocover hold down equipment
e) space around open Cryocover
f) between CVV and Thermal Shield 2 Baffle
g) between Thermal Shield 2 Baffle and Instrument Shield
h) between Instrument Shield and Instruments

which are modelled in the ASAP file

The recent changes with respect to gaps b) and f) have been described in chapter 4.4; gap f) will be partly closed by the object called 'Crown'. The Crown was fully treated for the ground case (RD4), for the orbit case the influence is marginal due to geometry and temperature. Therefore it was sufficient (for the orbit case) to apply an apparent emissivity for the gap with emissivity reduced from 0.9 to 0.5.

M1-baffle Cylinder/Cone

The cylindrical and the conical part of the baffle above the CVV have been traced in a single run. Therefore a medium temperature was inserted in table 6.4-1.

Cryocover
For thermal reasons, the outer rim of the cryocover now is black, in order to avoid the transfer of warm radiation from the gap between CVV and thermal shield 2 baffle onto the instruments during ground test as much as possible.

For sake of completeness, we list the contribution of the deleted version of the earlier black cryocover (i.e. black across the whole surface), i.e. 10% to be added for PACS, 0.4% for SPIRE.

Thermal Shield 2 Aperture
In order to get the required low temperatures for the instruments during ground testing, the Thermal Shield 2 Aperture was introduced very recently. This additional surface reduces the straylight during ground tests. However, it will add about 3% additional straylight for PACS and about 1% for SPIRE in orbit. New calculations with this aperture have been performed only for those straylight paths, where a significant impact onto results was expected. These are the paths originating from Thermal Shield 2 Aperture itself, the Thermal Shield 2 Baffle, and the gaps below the Instrument Shield.

Scattering within instruments
For most cases scattering within the instruments is negligible. The exceptions from that rule are the black thermal shield 2 baffle irradiating SPIRE.

Holes in the Optical Bench for harness routing and for cold fingers.
In the optical bench (OB) there are 4 large holes for harness routing (formerly in the +/- Y sides of the instrument shield) and 6 holes of different size for cold fingers.
The holes for harness routing will be closed by

- Aluminium plates, covering most of the hole, up to the OB harness brackets.
- the harness bundles itself will go through the OB harness brackets and sealed there with stycast.
- residual slits between the individual harness brackets will be taped with Al-tape.

Therefore it is expected that the total surface of the holes for harness routing remaining open is negligible.

Two large holes for the cold fingers will be closed neatly by MLI. The 4 smaller ones will have light tight devices, however, which cannot eliminate straylight completely. These light tight devices are neglected completely in our consideration, and therefore our worst case assumption is that 52 cm² in total remain open. In a further worst case assumption these 52 cm² have been located directly at the gap between instrument shield baffle and Instruments, such that further straylight propagation towards the Instruments can be calculated the same way as the contribution from the LOU windows via the side paths between the individual thermal shields. The effective temperature of the radiation going through these holes is set to the temperature of thermal shield 1, because the holes in this thermal shield, which would allow the penetration of higher temperature radiation, are closed by MLI.

Summary for thermal self emission, pessimistic case
The requirement of 10% is violated. The results are 29% for PACS and 14% for SPIRE.

Thermal self emission, optimistic case

Because the requirement is violated for the pessimistic case, results are given for an optimistic case too. In this optimistic case, the emissivities of reflecting surfaces have been reduced to favourable values. Also the various temperatures of the various objects have been changed to optimistic values (mostly the thermal cold case minus uncertainty). The results are given in Table 6.4-2.

For the contribution from the sunshade gap, a reduced emissivity of 0.08 was inserted (temperature and emissivity actually are a selection representing the synthetic case described in chapter 5.3).

For reasons of comparison, one has to leave the contributions from M1 plus M2 on the reference path constant, when comparing the pessimistic and the optimistic case. A reduced emissivity for M1 plus M2 would apparently ‘increase’ the straylight for the ‘optimistic’ case, since the large contribution from M1 plus M2 on the reference path is in the denominator of the relative fluxes presented in the tables.

As can be seen, the straylight values for PACS and SPIRE go down to 12 % and 8 % respectively. For PACS the requirement still is violated.

Table 6.4-2: Self emission onto PACS/SPIRE detectors, optimistic case

Emitting object with temperature T and emissivity ε	T [K]	ε	PACS 80 µm	PACS 230 µm	SPIRE 230 µm	SPIRE 670 µm
Sunshade (scattering on M1+M2 + spec.)	131	0.02	0.335	0.193	0.108	0.092
Gap Sunshade-M1 (scattering on M2)	204	0.08	0.800	0.378	0.074	0.059
Gap Sunshade-M1 (diffraction at M2-rim)	204	0.08	0.240	0.400	0.320	1.040
Hexapod	74	0.02	2.715	2.536	3.241	3.180
M1+M2 (without reference path)	74	0.005	0.958	0.895	0.679	0.666
Scattercone	74	0.005	0.239	0.223	0.000	0.000
M1-Baffle flat	74	0.02	0.399	0.373	0.323	0.317
M1-Baffle cone / cylinder	69	0.02	0.842	0.858	0.132	0.133
Gap betw. M1-Baffle cone and cylinder	69	0.90	0.816	0.831	0.194	0.195
Cryocover mirrors + plate	63	0.01	0.082	0.095	0.004	0.004
Reflecting objects near Cryocover	63	0.02	0.097	0.112	0.021	0.022
Cryocover black rim	63	0.50	0.665	0.768	0.118	0.123
Black gaps around Cryocover / M1-Baffle	63	0.50	1.356	1.565	0.189	0.196
CVV plate top	63	0.02	0.226	0.261	0.018	0.018
Gap betw. CVV / Thermal Shield 2 Baffle	63	0.30	0.084	0.097	0.030	0.032
Thermal Shield 2 Baffle (only specular)	41	0.50	0.223	0.590	0.306	0.398
Thermal Shield 2 Baffle (only scattering within instrument)	41	0.50	0.101	0.268	0.566	0.735
Thermal Shield 2 Aperture (upper side)	41	0.50	0.570	1.508	0.256	0.333
Thermal Shield 2 Aperture (lower side)	41	0.02	0.012	0.031	0.028	0.036
Instrument Shield Baffle	11	0.05	0.000	0.001	0.000	0.001
Gap below Instrument Shield Baffle	11	0.90	0.000	0.062	0.003	0.036
LOU via HiFi	136	0.90	<0.040	<0.040	<0.050	<0.050
LOU via gaps (below Instrument Shield Baffle etc.)	136	0.90	0.104	0.059	0.003	0.002
Holes in OB for cooling straps (with view on Thermal Shield 1 by reflection)	34	0.90	0.022	0.097	0.005	0.007
sum			**10.9**	**12.2**	**6.7**	**7.7**

Data for PACS and SPIRE are in % with 100% = telescope irradiation
('standard telescope' with 70 K, total ε=0.03)

7 Sources outside the FOV (Sun, Earth, Moon)

7.1 Specular paths from Moon and Earth

There are some specific directions from which the Moon or the Earth can be reflected specularly via various hexapod structures into the instrument detectors. The earliest basis (=design) for the calculations were hexapod legs with rectangular cross sections and hexapod bars nominally parallel to the Y/Z-plane.

The specular paths from moon/earth found during the calculations for issue 1 led to the recommendation of rounding the legs of the hexapod assembly. In the next step, the elliptical legs of the telescope are approximated with a polygonal cross section with 24 sides. Therefore slim plane surfaces exist in the model whereas the reality will be a curved surface. The polygonal modelling has the advantage to highlight paths which might be overlooked with curved surfaces (due to insufficient ray statistics), thus is very helpful. However these paths could be overestimated.

The specular paths found for the elliptical version are more spreaded over the sky, however they represent less sensitive paths. A comment from the scientists (e-mail from SPIRE dated 31.01.03) states that the minor degree of spreading is favoured (i.e. the rectangular legs are favoured), so the calculations of the earlier issue 1 (performed with the version with rectangular legs) are reported here again.

The changes mentioned in chapter 4.3 (new inclination of the hexapod bar introduced before year 2004, new center ring of the M1-baffle) will alter the directions found for the specular paths from moon and earth (also for those in RD1). They do not change the overall picture and the order of magnitude of the resulting straylight fluxes. However the specular paths exist for somewhat different directions, these differences in direction may influence mission planning.

Most of the specular directions are close to the limit for the possible moon directions, at around 20 degrees from the X-axis; therefore they are affected by the Moon (and bright stars) only and not by the Earth.

Figure 7.1-1 shows these directions for the case of the SPIRE detector, figure 7.1-2 displays the case of the PACS detector. Both are gained by a backward trace.

Two of the most important paths for SPIRE are shown in figure 7.1-3 and figure 7.1-4

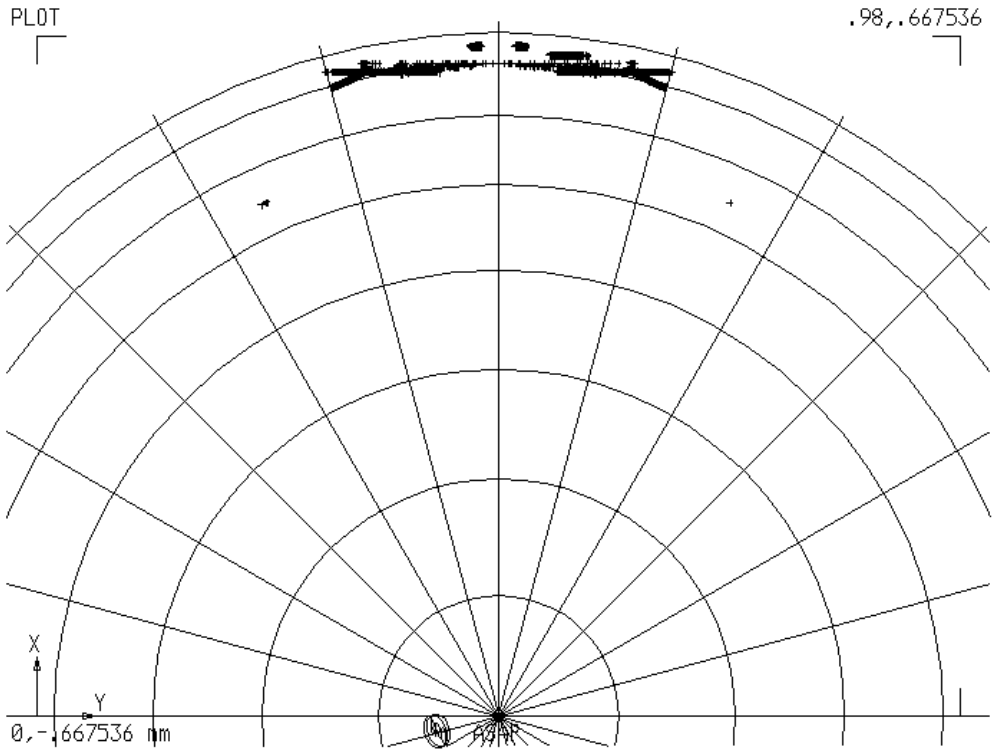

Figure 7.1-1: Directions from which specularily reflected rays can hit the SPIRE detector.

Plot of directions towards the sky. The center of this polar diagram is the +Z axis. The circles around the +Z axis have distances of 10 degrees. The outermost line roughly represents the limiting direction for the moon. The limit for the earth is between the 2nd and the 3rd circle from outside. Each + sign represents a direction with specular paths towards the SPIRE detector

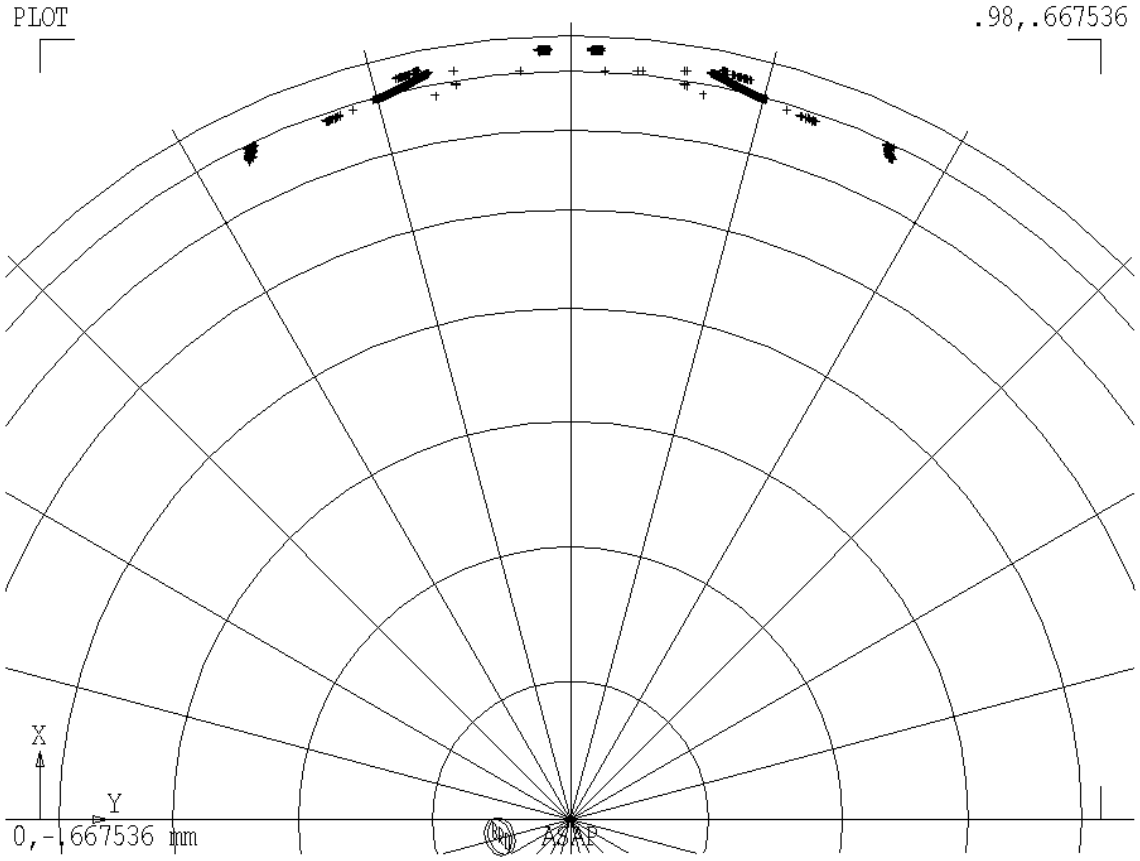

Figure 7.1-2: Directions from which specularily reflected rays can hit the PACS detector.

Plot of directions towards the sky. The center of this polar diagram is the +Z axis. The circles around the +Z axis have distances of 10 degrees.

The outermost line roughly represents the limiting direction for the moon.

The limit for the earth is between the 2nd and the 3rd circle from outside.

Each + sign represents a direction with specular paths towards the PACS detector

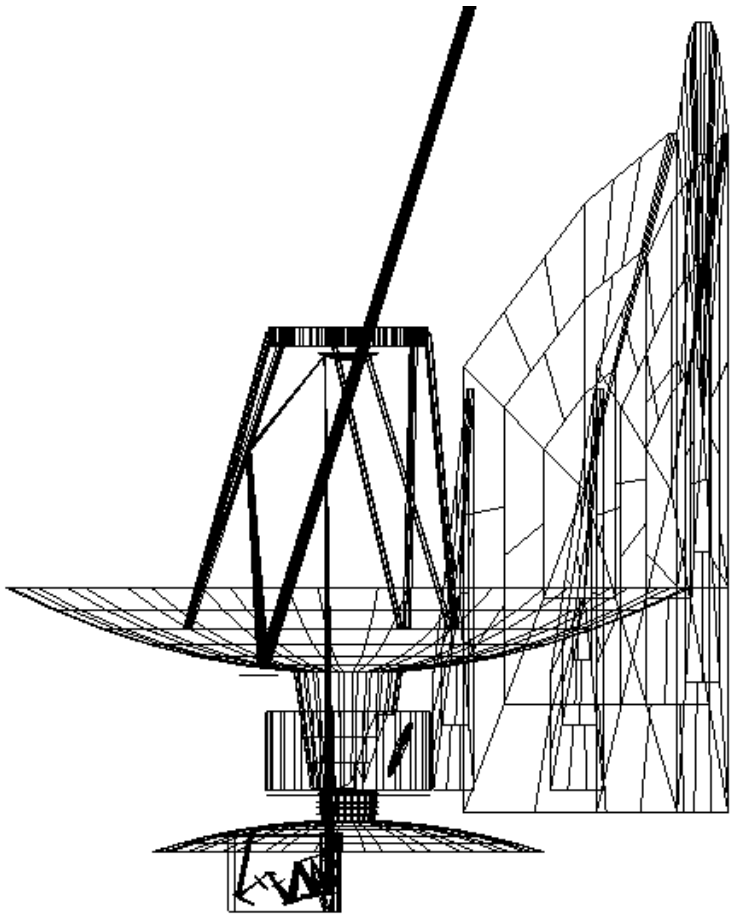

Figure 7.1-3: Specular Straylight path no. 1 for the moon

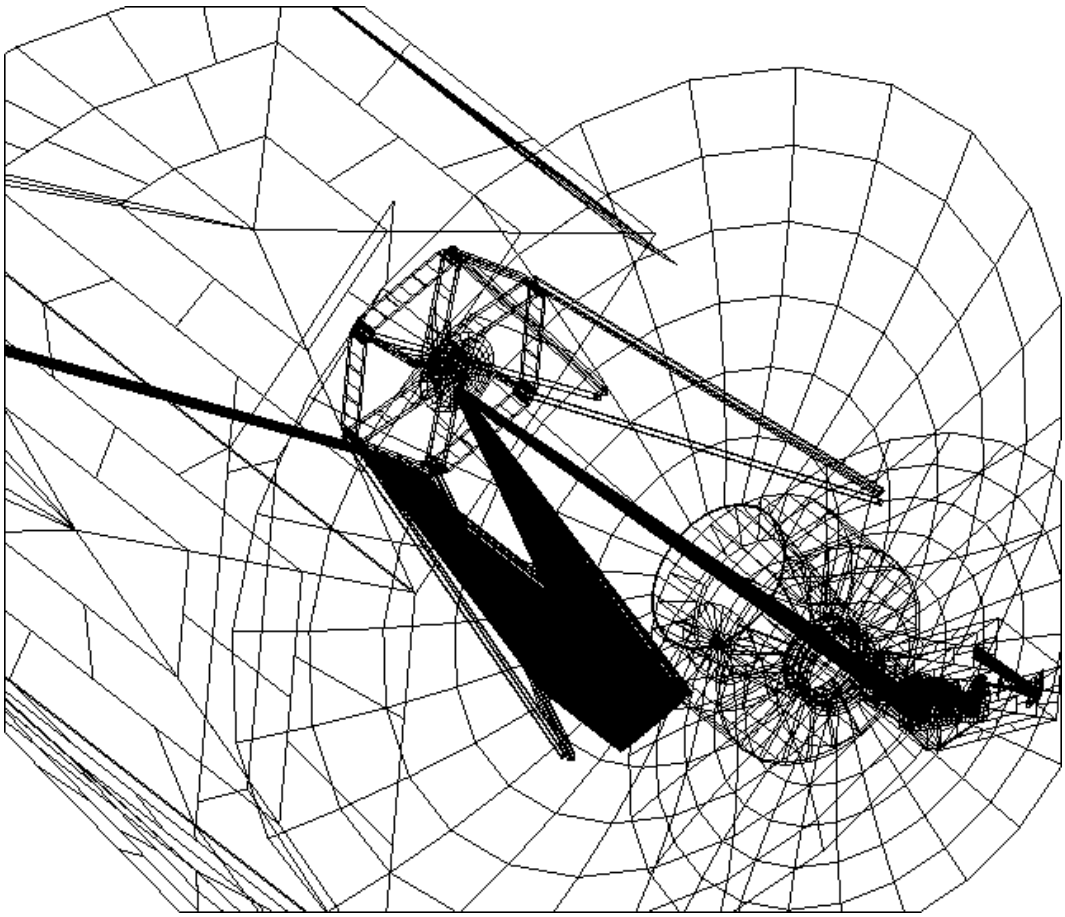

Figure 7.1-4: Specular straylight path no. 3 for the moon

Table 7.1-1 shows averaged coordinates and directions of some of the detected direct paths for the SPIRE detector. The directions are those plotted in figure 7.1-1. The coordinates are the averaged positions on Herschel, where rays on the specific path hit the first Herschel object (e.g. a hexapod strut, mirror M1, etc.).

path		coordinates of grid.			directions of source		
		X	Y	Z	A	B	C
1	**M1-Z**	**1297.47**	**284.46**	**-429.13**	**-.9189013081**	**-.2136134569**	**-.3310044862**
2	M1-Z	1297.53	-285.06	-427.56	-.9189812584	.21347118273	-.3308537199
3	**HEX-Y**	**2928.56**	**-301.65**	**237.96**	**-.9406922184**	**.13956008227**	**-.3089975805**
4	HEX+Y	2928.08	302.04	237.28	-.9406708956	-.1409893138	-.308641475

Table 7.1-1: Average coordinates and directions for the most important direct paths onto SPIRE detector

The radiation onto the SPIRE detector was calculated for paths no. 1, 2 and 3. Path 4 is symmetric to path 3, and therefore is expected to give similar results. All other paths show less radiation in the backward trace, and therefore are expected to give lower results.

Moon and Earth are treated as extended sources with angular radii of 0.002 and 0.005 rad, they are placed in a distance of 1,000,000 mm from the telescope, which is sufficient for the ASAP calculations. They are lambertian sources with emissivity 1, scattering towards the telescope targets. The Moon has such an angular extension that it covers most of the pixels of PACS and SPIRE detectors. Therefore the relative comparison to the telescope radiation is done by comparing radiances of moon and telescope and by division of the ASAP fluxes onto the detectors as in the case of self emission.

Results:
The paths result in real images on the detector. Paths 1 and 2 are somewhat diffuse, path 3 represents a sharp picture. All paths shown in the following table are potential paths for the Moon.

relative flux on SPIRE detector	path 1 and 2	1.5E-3 each
relative flux on SPIRE detector	path 3	1.9E-3.
contribution from M1 + M2 onto SPIRE detector	reference path	16.4

The contributions from these paths have to be corrected for temperature and for emissivity in order to do a correct comparison with the telescope. The assumed emissivity and temperature of the standard telescope mirrors is 0.03 and 70 K. The assumed emissivities and temperatures of the moon are 1 (black body), 100 K for the dark region, 400 K for the illuminated region (consistent with RD 2).

The contributions for all moon paths therefore have to be corrected by the following factors:

	Moon bright zone (400 K)		**Moon dark zone (100 K)**	
	80 µ	670 µ	80 µ	670 µ
temperature factor (=1 for 70 K)	21.25	6.55	2.39	1.50
emissivity factor	66.67	66.67	66.67	66.67
Total multiplication factor	**1417**	**437**	**159**	**100**

Table 7.1-2: Correction factors for ASAP results concerning the Moon.

The comparison to the telescope background therefore gives (in % of M1 + M2 straylight):

	Moon bright zone (400 K)		**Moon dark zone (100 K)**	
	80 µ	670 µ	80 µ	670 µ
Path 1	13.0%	4.0%	1.45%	0.92%
Path 2	13.0%	4.0%	1.45%	0.92%
Path 3	16.4%	5.1%	1.84%	1.16%

Table 7.1-3: Contributions from Moon on SPIRE detector for paths 1 - 3

Thus the specification of 1% is violated. The situation for PACS is similar as verified independently by ALCATEL (RD3).

The possible means for an improvement of the situation have not been introduced, see explanation given above.

Remark: The specular paths probably exist also towards other directions onto the sky due to the symmetry of the hexapod structure. There moon and earth will never appear, nevertheless planets and bright stars may reach these patches of the sky. Beam chopping and nodding will be affected. The rounding of the hexapod structures (mentioned above for the case of the moon patches) will also improve the situation for chopping and nodding. Maps displaying these directions can be found in RD 1. Please remind, that finally the rectangular legs were favoured by the scientists.

7.2 Scatter Paths from Moon and Earth

All results are presented as relative numbers w.r.t. the thermal radiation of the telescope mirrors M1 and M2.

Their contribution has been set to 100 so the violation of the requirement of 1% for moon/earth occurs if the numbers exceed 1.

The table shows that the scatter paths (scatter at primary and secondary mirror) are negligible. Thus only the patches mentioned in section 7.1 violate the specification.

Table 7.2-1: Scatter paths from moon/earth onto PACS and SPIRE detector

emitting object	PACS DETECTOR	area= 1320 mm^2	SPIRE DETECTOR	area= 902 mm^2
	flux	irradiance	flux	irradiance
moon at 13 degrees, cone baffle	8.69E-04	8.69E-04	5.00E-04	5.00E-04
moon at 13 degrees, cylinder baffle	8.09E-04	8.09E-04	4.37E-04	4.37E-04
earth at 23 degrees, cone baffle	4.09E-03	4.09E-03	1.81E-03	1.81E-03
earth at 23 degrees, cylinder baffle	4.22E-03	4.22E-03	1.72E-03	1.72E-03

The results reported here are those of issue 1, they have not been recalculated for the changes introduced since then:

- combined cylinder/cone baffle
- new mirror scattering function
- SPIRE apodization.

Since the numbers are so low, there is no danger for approaching the specified value of 1%, if a recalculation is done.

7.3 Solar irradiation

The diffraction of the solar radiation at the sunshade yields irradiances small compared to the specification as elaborated in RD1.

8 Sources inside the FOV

No calculations were made by ASED. The subject has been already treated by ASEF in RD1. The results from ASEF show compliance with the specification with good margin.

The question of cross-talk between SPIRE and PACS has been treated in RD3. For an assumed residual reflection of 10% on the SPIRE detector the in-field requirement is still met with margin.

9 Summary of Changes not fully reflected by present Calculations

The flat ring above the cylindrical part of the M1-baffle is part of most calculations in this issue 3. A recent change is the wish of HIFI for a conical shape of the innermost flat part of the M1-baffle. Meanwhile the flat shape has been abandoned and it was decided to realize an upwards angle of 3.5 degrees +/- 2 degrees for the upper flat part of the M1 central baffle. The consequences are estimated to be small for general straylight, since it has been verified that

a) no relevant specular rays exist from the sunshade towards the experiments with that new baffle ring

b) the path

sunshade--->scattering on the M1-baffle-ring--->M2--->instruments

is negligible (also with the new tilt).

The new inclinations of the hexapod bar introduced before year 2004 (and the change mentioned above) will alter the directions found for the specular paths from moon and earth (also for those in RD1). They do not change the overall picture and the order of magnitude of the resulting straylight fluxes. However the specular paths exist for somewhat different directions, these differences in direction may influence mission planning.

Thermal constraints influencing the ground test have led to the recent introduction of the Thermal Shield 2 Aperture and also the Crown between CVV and Thermal Shield 3. The paths of the Thermal Shield 2 Aperture have been recalculated insofar, as they were considered to have a potential impact (there was a slight straylight increase). The Crown was treated in full detail for the ground case (RD4), for the orbit case the influence is marginal due to geometry and temperature. Therefore the calculation with an apparent emissivity reduced from 0.9 to 0.5 was suffcient.

10 Summary on Straylight

Summary for thermal self emission:

The requirement of 10% is violated. The actual values are 29% for PACS and 14% for SPIRE. Possible improvements (large scattercone) have not been introduced because of disadvantageous obscuration.

Summary for out-of-field sources (Sun, Earth, and Moon):

This radiation is within specification, except for small locations on the sky, where radiation reflected at rectangular hexapod structures can enter the instruments directly. These small locations exist mainly for the Moon. Only two minor paths were found which could be applicable also for the Earth. For the worst case locations of the Moon the specification is exceeded by about a factor of up to 17.

Note: Because these straylight paths partially lead to sharp ghost images on the detector, even bright stars/planets on these locations could influence chopping and nodding. There are much more dangerous locations for bright stars than for moon and earth.

Summary for in-field Sources:

The requirement is met with good margin.

11 Appendix: Scattering Models used for the Calculations

The following pictures show the scattering models used for the calculations.

Models for Telescope and Cryostat parts (Figures 11.1-1 through 11.1-3)
PACS scatter model (Figure11.2-1)
SPIRE scatter models (Figures 11.3-1 through 11.3-5)

In addition, a Lambertian model (BSDF=0.1/π per sr) was used for

- the filter in the PACS pupil (in transmission)
- PACS mechanics around the PACS opening.

(model not shown as picture).

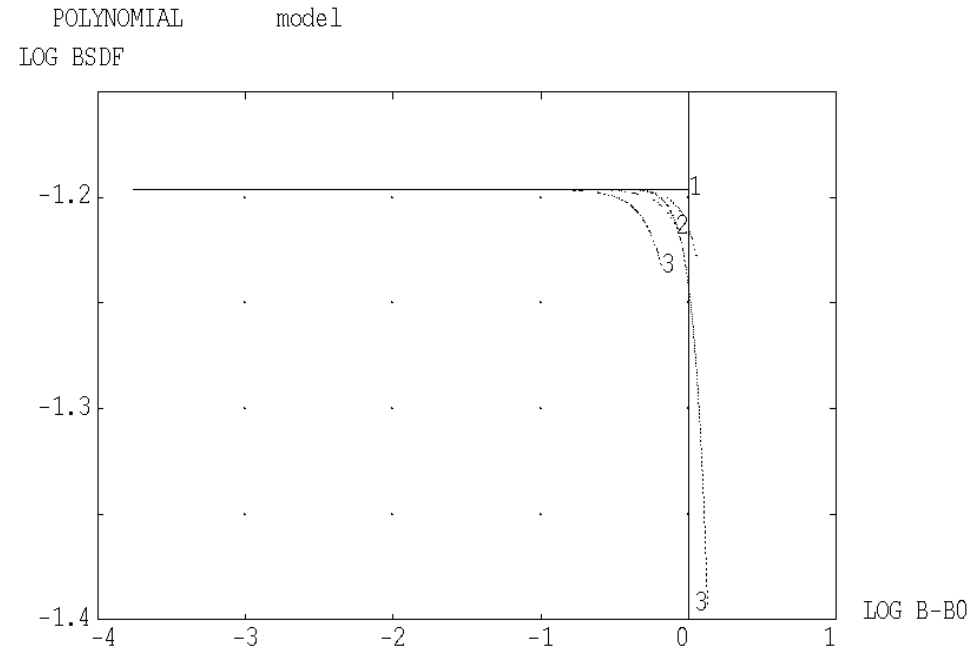

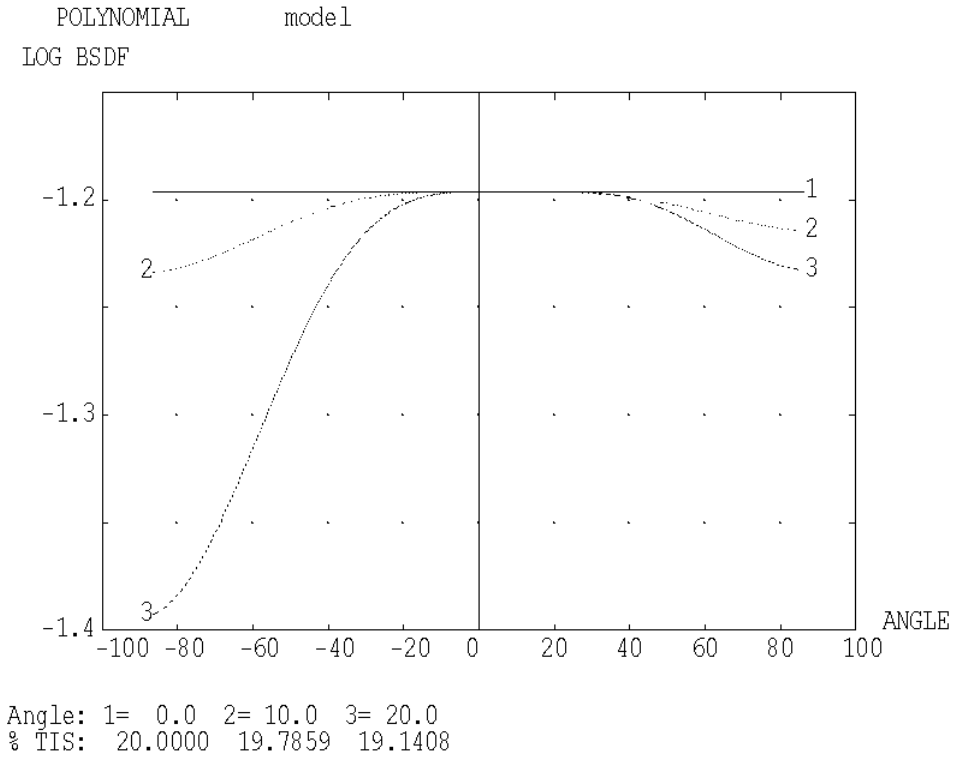

Fig. 11.1-1: Model for thermal shield 2 baffle and instrument shield baffle tube
(also for deleted black flat cryocover variant)
(POLYNOMIAL 2 2 LOG[.2/3.1416] 5@0, 0 0 1.8 0 0 1.8, 0 -1.8)
The upper plot mainly shows the values for small scattering angles
The lower plot mainly shows the values for large scattering angles

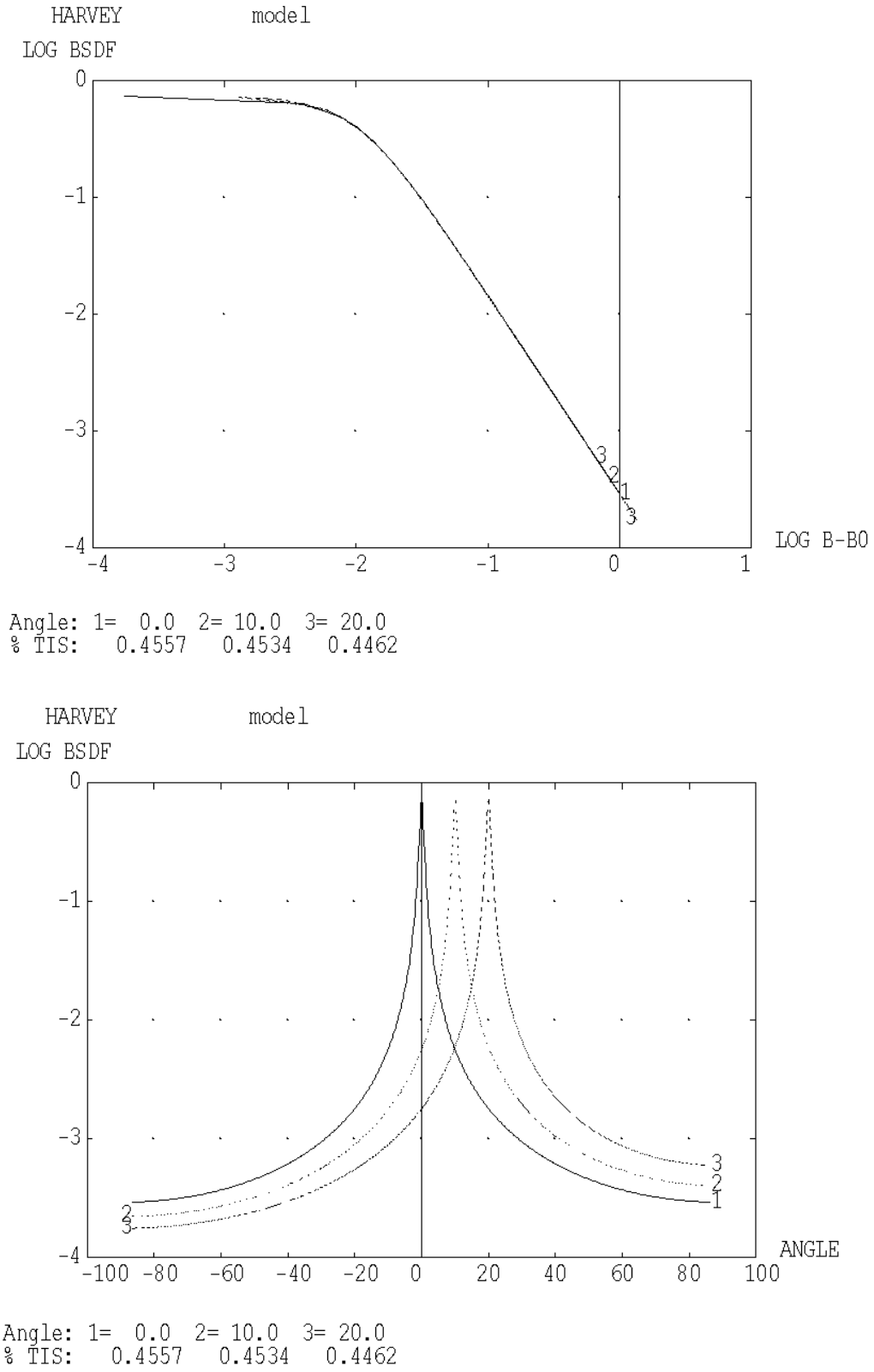

Fig. 11.1-2: Model for telescope mirrors, Harvey 0.73 -1.7 0.01
The upper plot mainly shows the values for small scattering angles
The lower plot mainly shows the values for large scattering angles

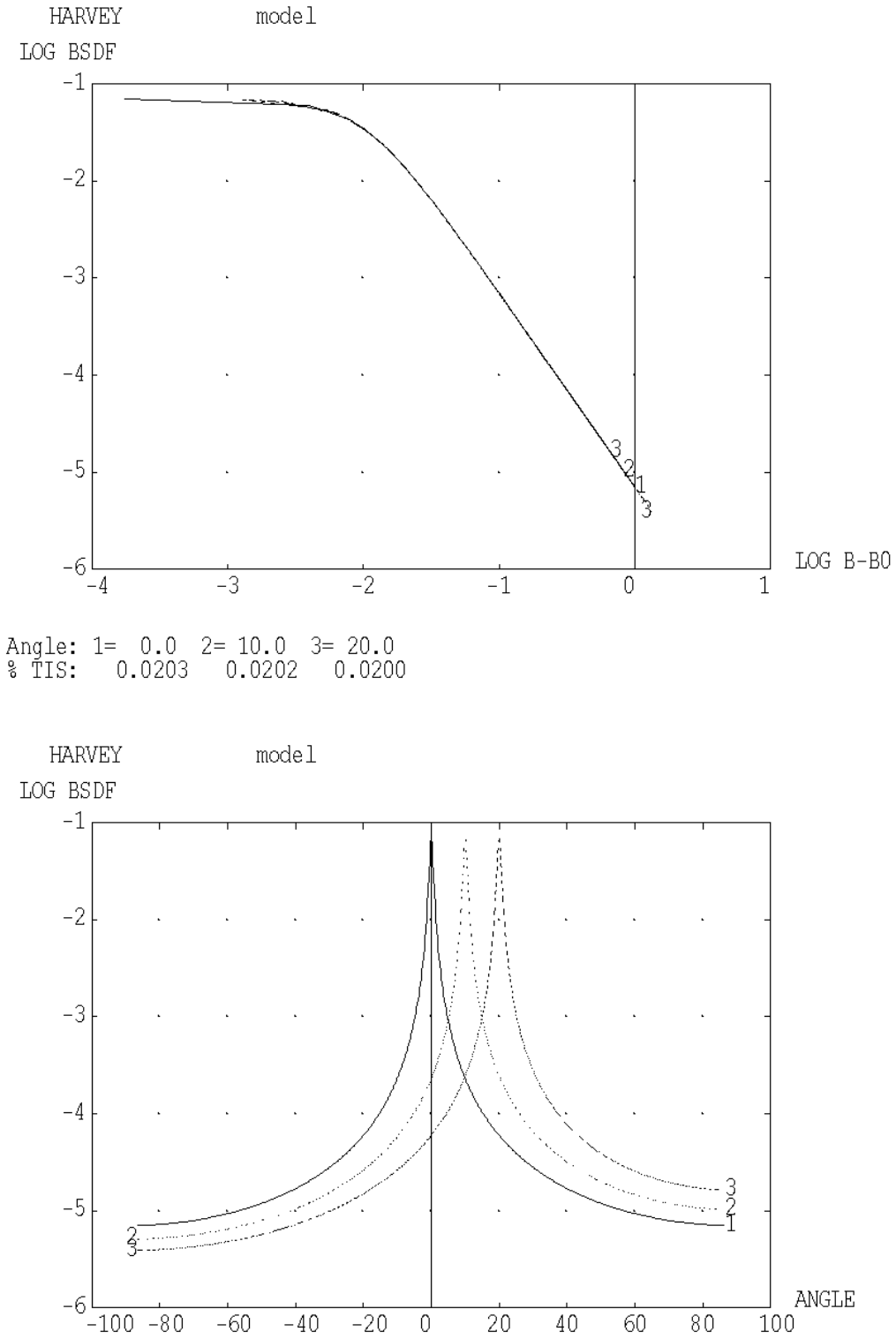

Fig. 11.1-3: Model for instrument shield flat and flat cryocover parts, Harvey 0.07 -2 0.01
The upper plot mainly shows the values for small scattering angles
The lower plot mainly shows the values for large scattering angles

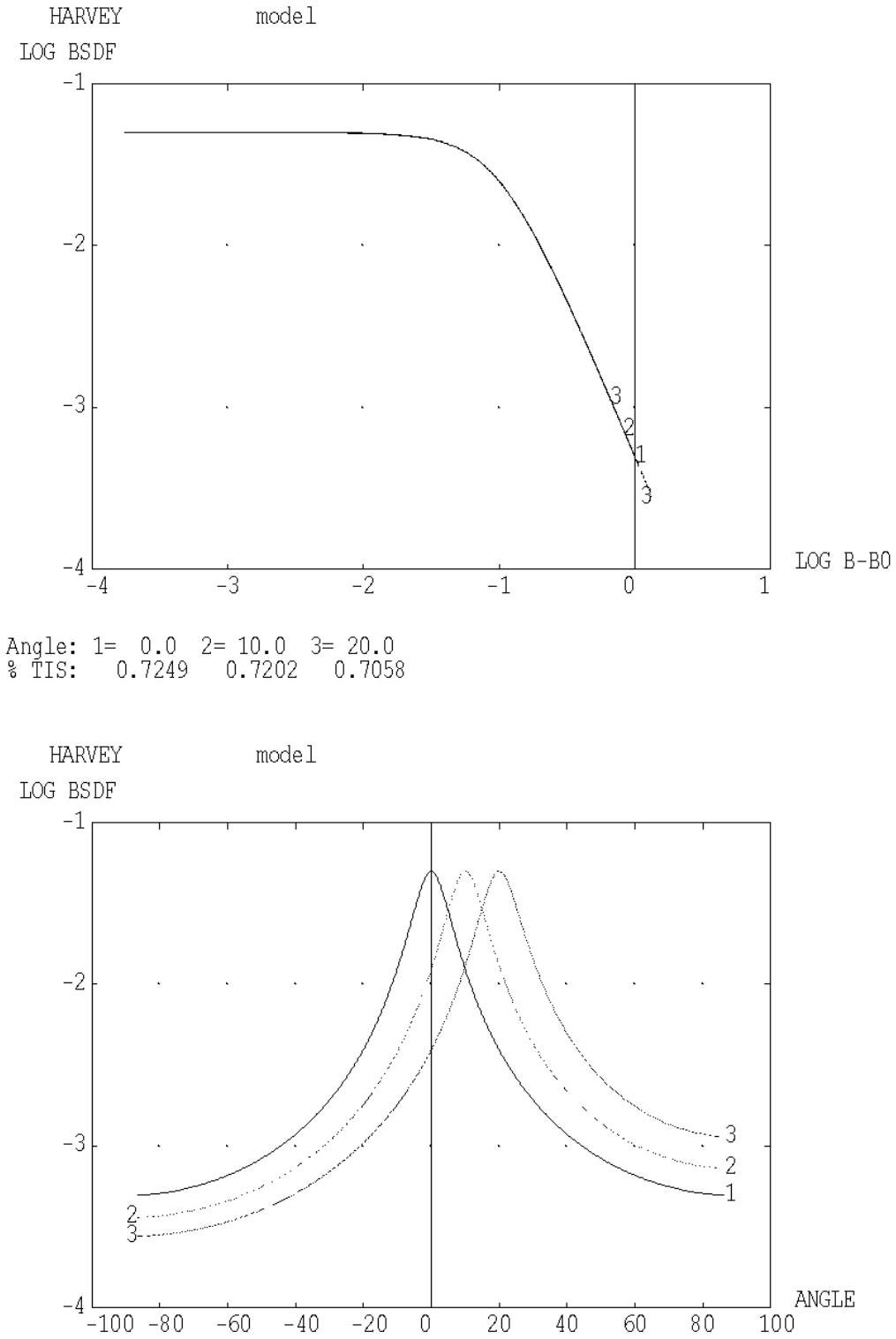

Fig. 11.2-1: Model for PACS Trog1, Trog2, Trog3, Fold1, Harvey 0.05 -2 0.1
The upper plot mainly shows the values for small scattering angles
The lower plot mainly shows the values for large scattering angles

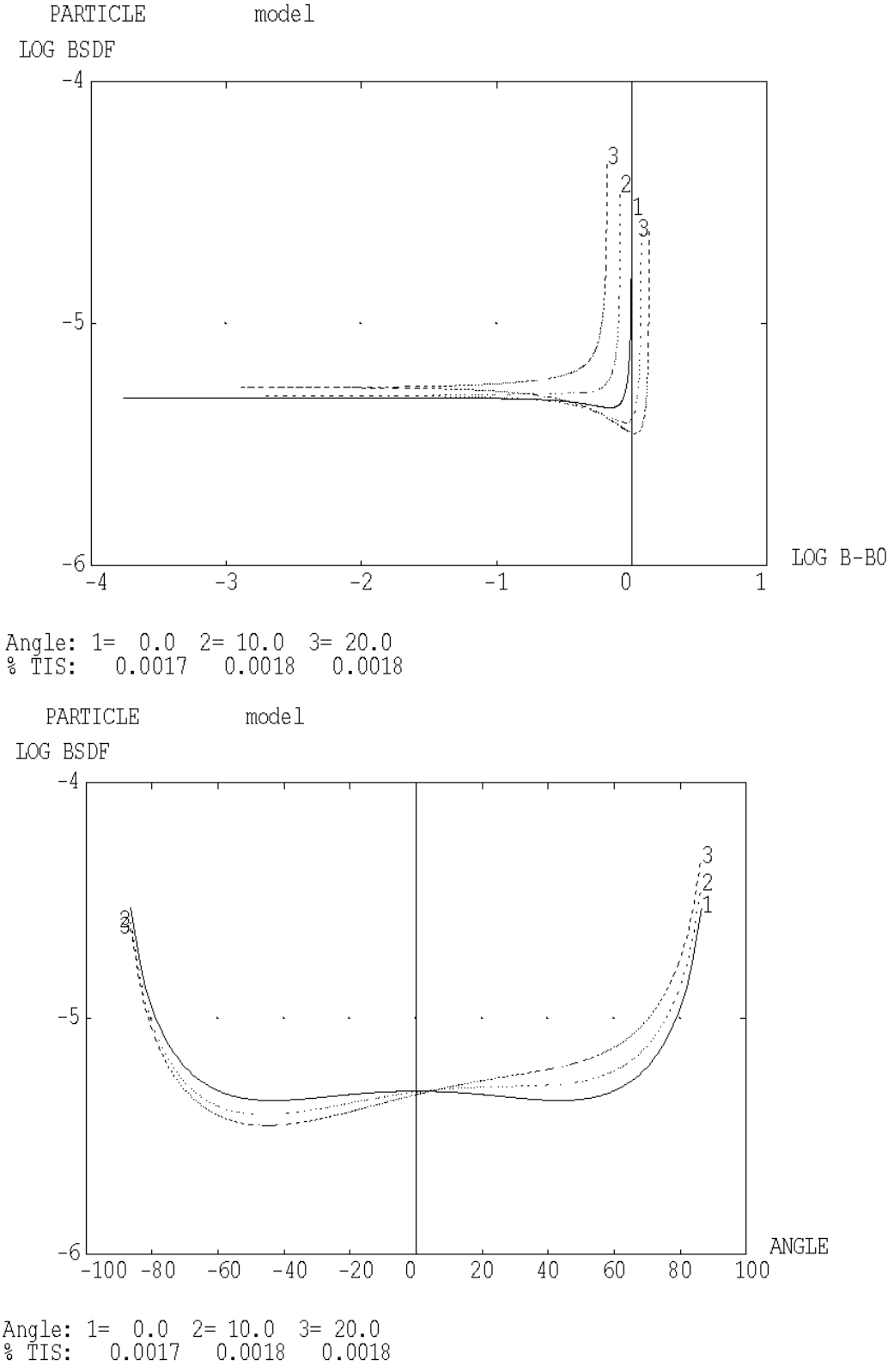

Fig. 11.3-1: Model for SPIRE mirrors, especially M3 (particle model),
The upper plot mainly shows the values for small scattering angles
The lower plot mainly shows the values for large scattering angles

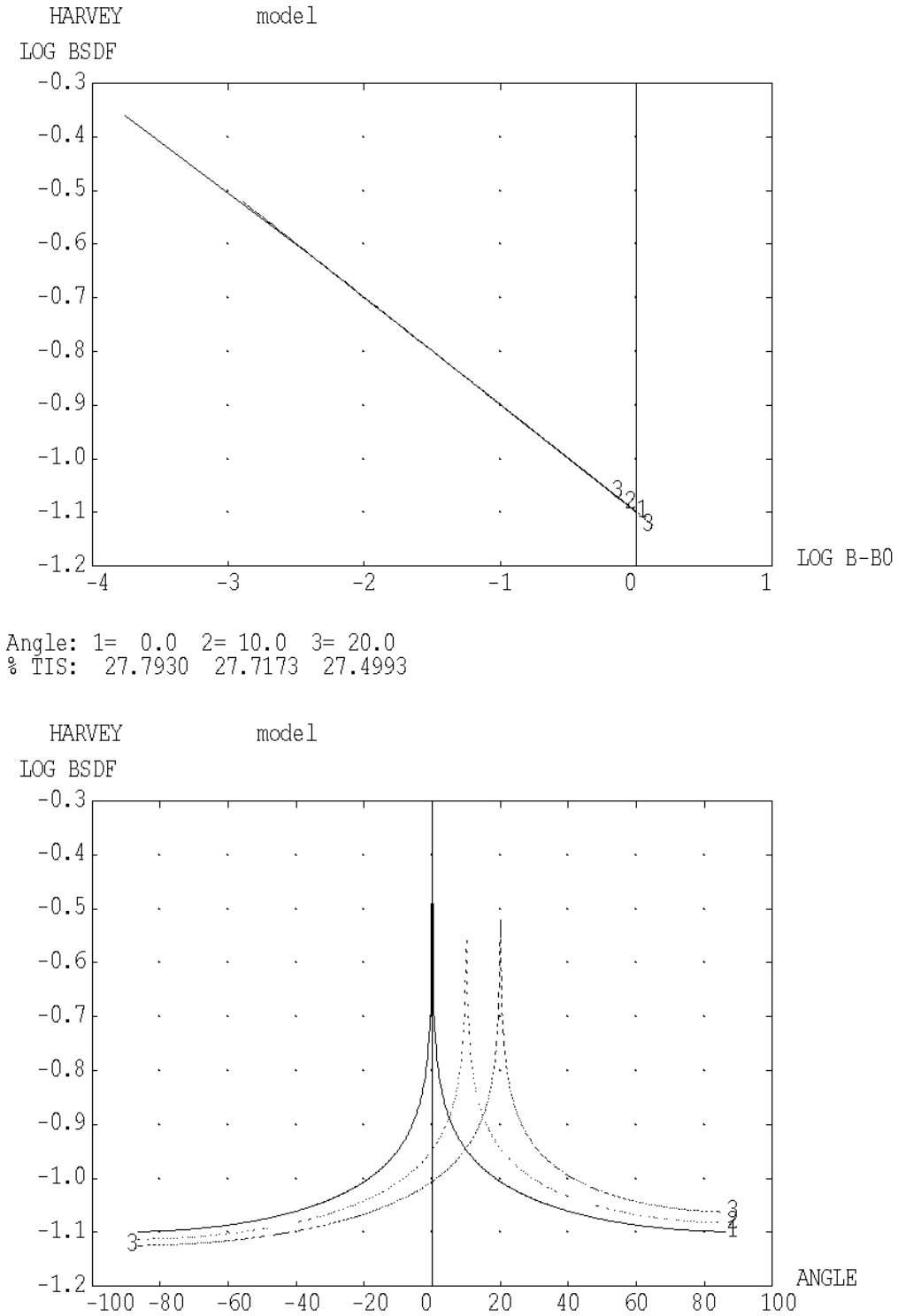

Fig. 11.3-2: Model for SPIRE M4 aperture (i.e. mechanics around M4), Harvey 0.2 -0.2
The upper plot mainly shows the values for small scattering angles
The lower plot mainly shows the values for large scattering angles

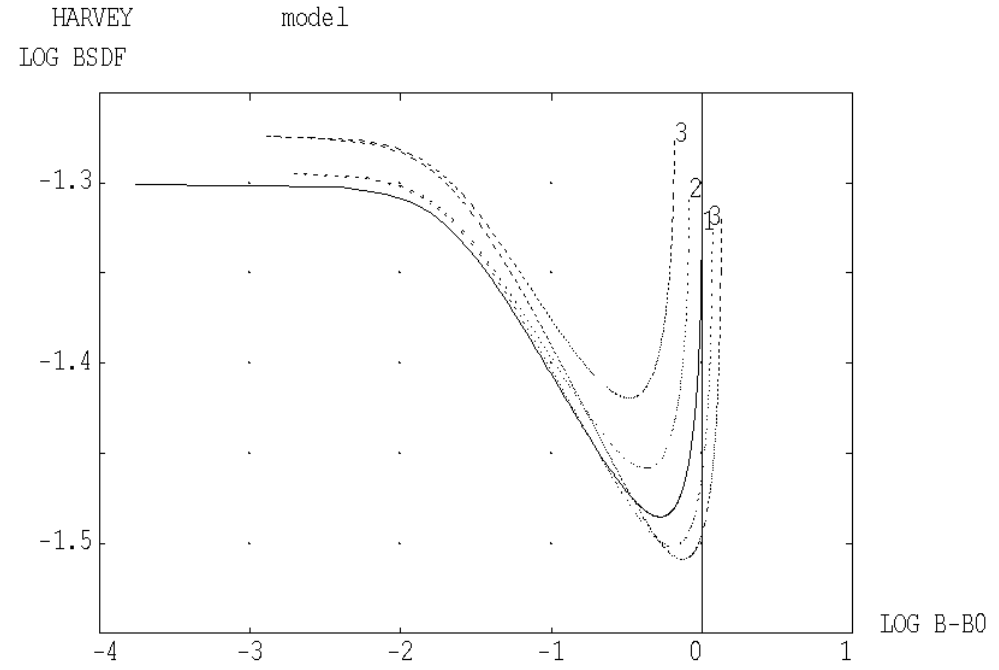

Angle: 1= 0.0 2= 10.0 3= 20.0
% TIS: 11.1359 11.2068 11.4268

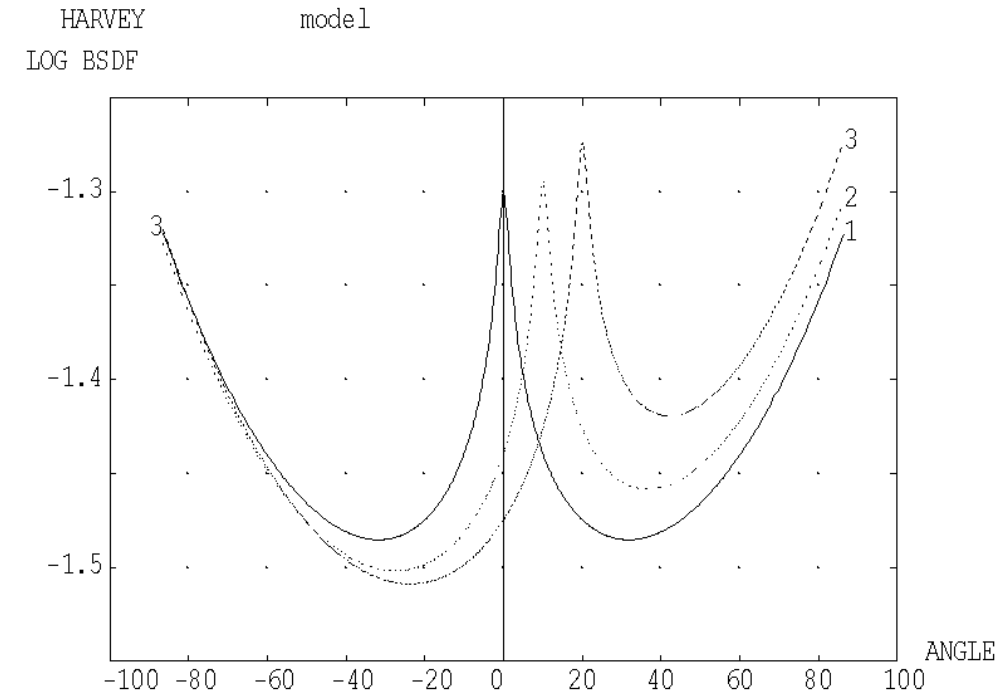

Angle: 1= 0.0 2= 10.0 3= 20.0
% TIS: 11.1359 11.2068 11.4268

Fig. 11.3-3: Model for SPIRE FP_UNIT, upper part, HARVEY 0.05 -0.15 0.02 1 1
The upper plot mainly shows the values for small scattering angles
The lower plot mainly shows the values for large scattering angles

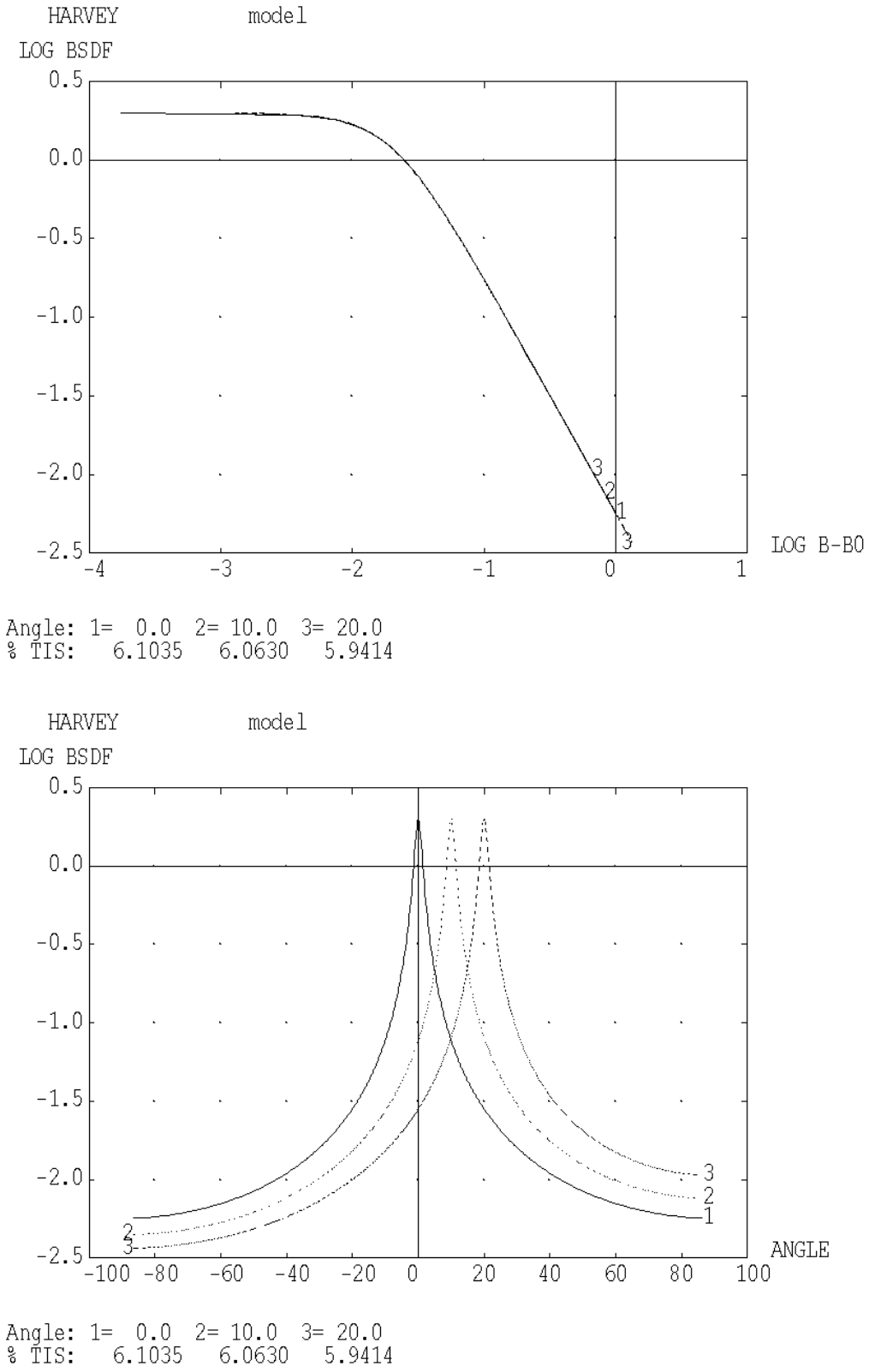

Fig. 11.3-4: Model for SPIRE FP_UNIT, lower part, HARVEY 2 -1.5 0.02
The upper plot mainly shows the values for small scattering angles
The lower plot mainly shows the values for large scattering angles

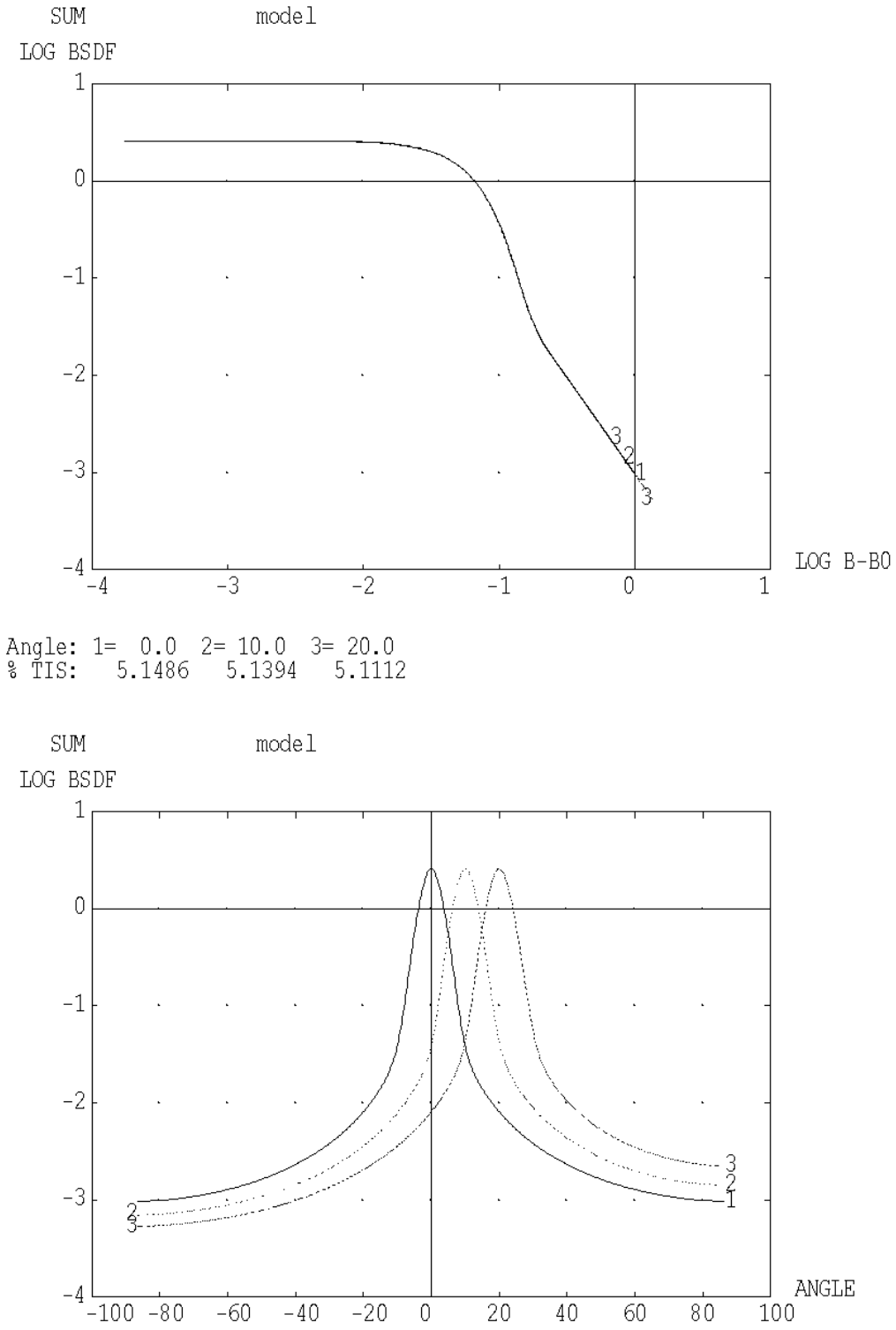

Fig. 11.3-5: Model for SPIRE filter 1, sum of Harvey 2.0 -50 0.35 and Harvey 0.60 -2.0 0.04
The upper plot mainly shows the values for small scattering angles
The lower plot mainly shows the values for large scattering angles

E N D O F D O C U M E N T

	Name	Dep./Comp.		Name	Dep./Comp.
	Alberti von Mathias Dr.	AOE22		Stritter Rene	AED11
	Alo Hakan	OTN/TP 45		Tenhaeff Dieter	AOE22
	Barlage Bernhard	AED11		Thörmer Klaus-Horst Dr.	OTN/AED65
	Bayer Thomas	AET52		Wagner Klaus	AOE23
	Faas Horst	AEA65		Wietbrock, Walter	AET12
	Fehringer Alexander	AOE13		Wöhler Hans	AOE22
	Frey Albrecht	AED422			
	Gerner Willi	AED11			
	Grasl Andreas	OTN/AET52			
	Grasshoff Brigitte	AET12			
	Hauser Armin	AOE23			
	Hinger Jürgen	AOE23			
	Hohn Rüdiger	AET52		Alcatel	ASP
	Huber Johann	AOA4		ESA/ESTEC	ESA
	Hund Walter	ASE4A			
	Idler Siegmund	AED432		**Instruments:**	
	Ivády von András	FAE22		MPE (PACS)	MPE
	Jahn Gerd Dr.	AOE23		RAL (SPIRE)	RAL
	Kalde Clemens	APE3		SRON (HIFI)	SRON
	Kameter Rudolf	OTN/AET52			
	Kettner Bernhard	AOE22		**Subcontractors:**	
	Knoblauch August	AET32		Air Liquide, Space Department	AIR
	Koelle Markus	AET22		Air Liquide, Space Department	AIRS
	Kroeker Jürgen	AED65		Air Liquide, Orbital System	AIRT
	Kunz Oliver Dr.	AOE23		Alcatel Bell Space	ABSP
	Lamprecht Ernst	OTN/ASI21		Astrium Sub-Subsyst. & Equipment	ASSE
	Lang Jürgen	ASE4A		Austrian Aerospace	AAE
	Langfermann Michael	AET52		Austrian Aerospace	AAEM
	Mack Paul	OTN/AET52		APCO Technologies S. A.	APCO
	Muhl Eckhard	OTN/AET52		Bieri Engineering B. V.	BIER
	Pastorino Michel	ASPI Resid.		BOC Edwards	BOCE
	Peitzker Helmut	AED65		Dutch Space Solar Arrays	DSSA
	Peltz Heinz-Willi	AET42		EADS CASA Espacio	CASA
	Pietroboni Karin	AED65		EADS CASA Espacio	ECAS
	Platzer Wilhelm	AED22		EADS Space Transportation	ASIP
	Puttlitz Joachim	OTN/AET52		Eurocopter	ECD
	Rebholz Reinhold	AET52		HTS AG Zürich	HTSZ
	Reuß Friedhelm	AED62		Linde	LIND
	Rühe Wolfgang	AED65		Patria New Technologies Oy	PANT
	Runge Axel	OTN/AET52		Phoenix, Volkmarsen	PHOE
	Sachsse Bernt	AED21		Prototech AS	PROT
	Schink Dietmar	AED422		QMC Instruments Ltd.	QMC
	Schlosser Christian	OTN/AET52		Rembe, Brilon	REMB
	Schmidt Rudolf	FAE22		SENER Ingenieria SA	SEN
	Schweickert Gunn	AOE22		Stöhr, Königsbrunn	STOE
	Stauss Oliver	AOE13		Rosemount Aerospace GmbH	ROSE
	Steininger Eric	AED422		RYMSA, Radiación y Microondas S.A.	RYM